Universität Potsdam

Influence of the Pore Structure and Chemical Properties of All-Carbon Composites on their Electrochemical Properties in Lithium-Ion Capacitors

Dissertation

zur Erlangung des akademischen Grades

Doktor der Naturwissenschaften (Dr. rer. nat.)

In der Wissenschaftsdisziplin „Anorganische Chemie"

eingereicht an der

Mathematisch-Naturwissenschaftlichen Fakultät

der Universität Potsdam

von

Jinyeon Hwang

Geboren am 12.02.1990 in Seoul, Repulik Korea (Südkorea)

Potsdam-Golm, im Januar 2023

Acknowledgment

Like river Havel's leisurely flow in front of my house in Potsdam, nearly four years have flown by since 2018 when I first set foot in Germany. The proposition "Nature knows the answer" is a basic value in conducting my research both then and now, and has inspired me a lot. Among my first seminar slides presented in the Max Planck Institute, I remember the grass of Babelsberg Park in the introduction. I still strongly believe that many solutions for future generations can also be found inside ordinary trees, insects, and even food around us. Nature knows eco-friendly, sustainable energy sources, and mechanism behind them to achieve efficient system. The past research experiences in Germany with great research seniors and wonderful colleagues were enough to cultivate the ability to do such research.

I would like to express my gratitude to many of the people who help me make this research possible. First of all, I would like to express my gratitude to Prof. Dr. Martin Oschatz with unlimited glory. Of course, because he gave me the opportunity to conduct my doctoral work at Max Planck Institute of Colloids and Interfaces (MPIKG) and the University of Potsdam (UP), I always thank him a lot but there was more behind this. I think he will be an unforgettable role model for me. He has consistently shown in action over the past few years what are a good researcher and a good leader. There were many twists and turns in conducting the research, however, he gave lots of meaningful and effective advice for academic fields as well as my private fields. He was more than a group leader for me, and it would have been really hard to be continuously motivated without his involvement and encouragement. Taking this opportunity, I would like to express my gratitude once again.

I also give huge thankfulness to Prof. Dr. Markus Antonietti. The professor's passion for continuous research and beautiful ideas has enabled new directions to approach research topics,

especially effective comments during the seminar. But most of all, I will never forget the generosity and second opportunity you gave me. Many things have happened so far, but I will try my best to become a better and more conscientious researcher based on lessons from the past.

I would like to offer my thanks to Prof. Dr. Andreas Taubert of UP for reviewing my thesis and providing me the opportunity to achieve successful Ph. D. degree in the university. In addition to Prof. Dr. Taubert, I would like to thank Prof. Dr. Helmut Schlaad who gave me a wonderful lecture and inspiration on various organic materials.

Without the help of the following collaborators, it would not be possible to reach the goal line. I would like to thank Dr. Tobias Heil, Heike Runge, and Bolortuya Badamdorj for their discussion and an enormous help to collect the best quality of SEM/EDX data and special techniques to do so. Ines Below-Lutz offered me lots of support not only on research (synthesis of HAT) but also on research-related fundamental works. Administrative tasks and ordering chemicals were sometimes hassled, but she helped me a lot. Without the passionate participation of other technicians in MPIKG, the work could not be successfully preceded: Antje Völkel for elemental analyses, Ursula Lubahn for TGA, Daniel Werner for powder XRD and SAXS, Dr. Clemens Schmitt for Raman, and Jessica Brandt for general help since 2018.

My time at MPIKG and UP has brightened thanks to my wonderful colleagues in the same 'carbon group'. I never forget Dr. Jonas Pampel's limitless support and cheering when I was in huge struggles. Besides Jonas, it was my great pleasure to work with a magnificent research team: my office-mate Ipek, my Potsdam/Korean neighbor Sol, a wonderful splendid couple Ralf and Milena, the electrochemistry mates (Konstantin, Amrita, Ivan), and big Chinese friends (Runyu, Qing, Wuyong, Ming) who are the influencers giving me what the passion on the research is.

MPIKG friends (Korean gangsters with Hyun-Il, Geonho, Soeun, Unforgettable holiday trip to Leipzig with Majd, Crazy Chez Briel moments with Baris, Dainel, Alessandro, Paolo, Francesco,

Grill-boat trip with Qian and Jianrui) and UP colleagues (Susanne, Karis, Holger, Tobias, and wonderful friends Anna, Cevin, Boris) gave me encouragement, suggestions, and support. They also provided me what German life is, which was meaningful in large part for relaxing the tension, re-thinking the value of research, and the way of enjoying life. It was all the precious time together.

Lastly, I want to express profound appreciation to my supporters in my home country, Korea. My previous advisor in SNU (Prof. Dr. Ki Tae Nam) and senior researchers/colleagues in KIST have supported me a lot. Thanks to my beloved family, I got a lot of encouragement even though they are apart from more than 8000 km. There would be no word in the world to express the whole love I have felt for my stay in Germany.


Thank you all

Table of contents

1. Introduction

1.1 Motivation

Climate change has recently become such a serious issue that it affects not only our personal lives but also government policies. The catastrophes in 2021 such as the heavy rainfall in western Germany (which killed 243 people and caused more than 10 billion euros of property damage), and the disastrous large-scale forest fires in both Europe and America are related to this climate change.[1,2] This is not just a problem of the economy, industry, and agriculture for human beings alone, but it is even a matter of "survival" for other living beings as well. For example, polar bears are dying of melting icebergs in the Arctic Sea, and coral reefs in the ocean are dying from overwhelming temperature increments as shown in **Figure 1**. According to the IPCC (Intergovernmental Panel on Climate Change) report, 24% of living creatures on Earth will be endangered if the global temperature rises by 2.2°C and 35% if it rises by 2.9°C.[3] If people in modern society do not give up the inertia to the existing life patterns accumulated since the industrial revolution, the possibility to halt this deadly temperature increase (nearly 2 degrees of global average temperature increase compared to pre-industrial times) occurring under the current conditions seems highly unlikely.[4,5] For this reason, various civic movements mostly led by environmental activists such as Greta Thunberg (2019 Nobel Peace Prize nominee) and various international treaties among countries (e.g. Kyoto protocol in 1997, Paris agreement in December, 2015) have recently been globally initiated.[6,7] However, there is skepticism regarding the effect of these efforts. The anxiety that there is not much time

left to cope with the current climate change is spreading beyond the industry to the research community.
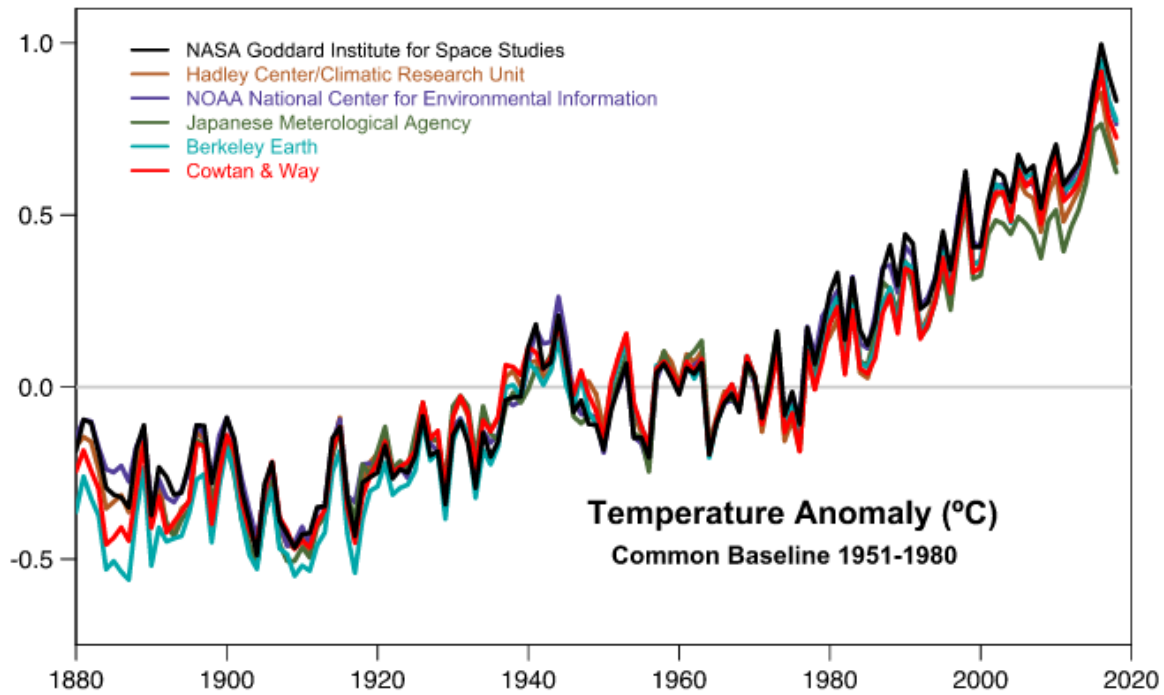
Figure 1. Increase of annual global surface temperature calculated by six different analyses through 2018. NASA stands for National Aeronautics and Space Administration, and NOAA stands for National Oceanic and Atmospheric Administration. Copyright 2019, John Wiley and Sons.[8]

It is generally accepted that the main reason for climate change and the rising global temperature is the constantly increasing emission of greenhouse gases (e.g. CO_2, CH_4, NO_2).[9–12] Greenhouse gases trap the reflected solar radiation energy from the Earth's surface and prevent it from escaping out of Earth again. This excess heat captured by the atmosphere generates an additional greenhouse effect despite the moderate albedo value (30.6%) of the Earth (albedo is a meteorological term to express the reflectivity of solar energy; 0% when not reflected at all, 100%

when fully reflected).[13] In particular, the concentration of CO_2 in modern times (419.1 ppm in 2021) has significantly increased as compared to the concentration before the industrial revolution (~270 ppm, **Figure 2(a)**).[10,14,15] Although the impact of some other greenhouse gases (i.e. CH_4) is greater than that of carbon dioxide, CO_2 emissions are both directly and indirectly correlated to the rapid development in transportation or manufacturing as a consequence of the increased human activities.[12,16,17] Annually, CO_2 is generated about 40 billion tons. When taking a look at Germany as an example, with 770 million tons per year the country emits the largest amount of CO_2 in the European Union and it ranks sixth (2.2%) among all countries in the world emission.[18,19] However, the energy-related CO_2 emission "per capita" is 9.71 tons per year as shown in **Figure 2(b)**, which is nearly more than double the global average of 4.38 tons or that of China (4.57 tons per capita).[19–21] As a result, it needs cooperative global efforts at the same time because reducing CO_2 emission is not the problem of one certain country or community alone.
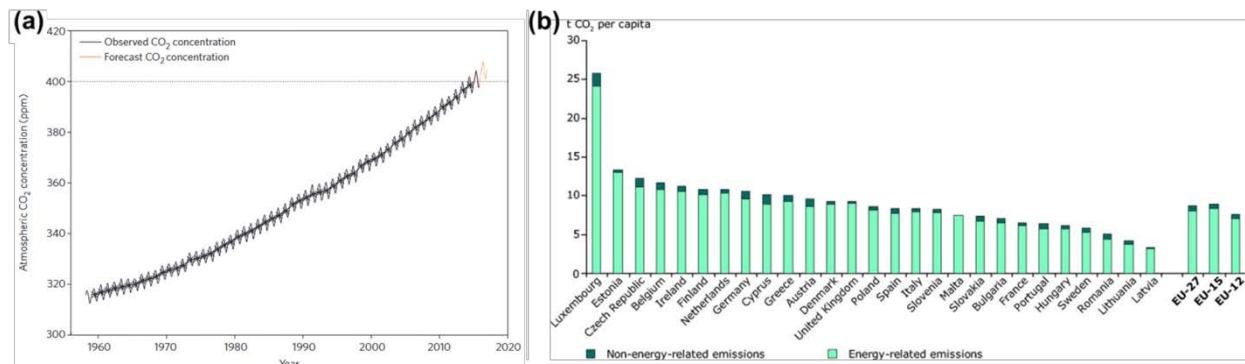

Figure 2. (a) CO_2 concentration measured at Manua Loa Observatory in United States. Copyright 2016, Springer Nature.[15] (b) CO_2 emission per capita of European countries classified by energy-related and non-energy-related emission. Copyright 2009, European Environment Agency.[21]

As of 2021, 355 million tonnes of CO_2 was emitted in Germany, which is 11% larger amount than that of 2020. More than 66% (235 million tonnes) of this emission is originated from the power stations to generate electricity.[19] The reason why an enormous amount of CO_2 is generated from the power plants is that most of the current electricity production is based on the combustion of fossil fuels. In terms of CO_2 generation, these combustion-based power plants operating mainly by brown or black coal emit much as for instance compared to nuclear power plants or regenerative energy systems.[22,23] Particularly, Germany is one of the major countries for both brown coal production and consumption (168.2 million tons, or 17% of the world's brown coal consumption), and generates 14% of the total gross electricity by coal combustion in 2017.[24,25] As a consequence, it still produces nearly 40% of national electricity with emission-intensive fossil fuels as shown in **Figure 3**, even though Germany tries to raise the renewable power sources as a leading country in EU. In addition to greenhouse gas emissions, there are many different reasons to reduce the use of fossil fuels. As can be seen from the massive power outrage in China following the cutting of coal imports from Australia in 2021, and the energy crisis in Europe caused by the reduced supply of natural gas from Russia due to the Ukraine war in 2022, the concentrated reserves of fossil fuels in certain regions could destabilize the energy security of importing countries and the price of the energy source. For example, Germany imports 61% of coal, 97% of oil, and 83% of natural gas to obtain energy.[26–28] Furthermore, during the mining process of fossil fuels, additional problems such as air pollution caused by dust generation, exposure of heavy metals, groundwater pollution, depletion, and labor exploitation cannot be overlooked. For this reason, the paradigm shift to eco-friendly energy generation emerges already as a huge inevitable trend worldwide. For instance, German

Chancellor Olaf Scholtz announced that the "complete ending plan" of brown coal-based power generation is set as a goal until 2038.[24,29] Energy plays a vital role for modern human society to thrive and the related energy demand thus gradually increases with the growth of the global population, which is expected to rise to 9.8 billion by 2050.[30] Consequently, sustainable end energy generation with less contamination must be achieved for the future of mankind and the Earth, until the possible development of new zero-emission technology such as nuclear fusion plants.
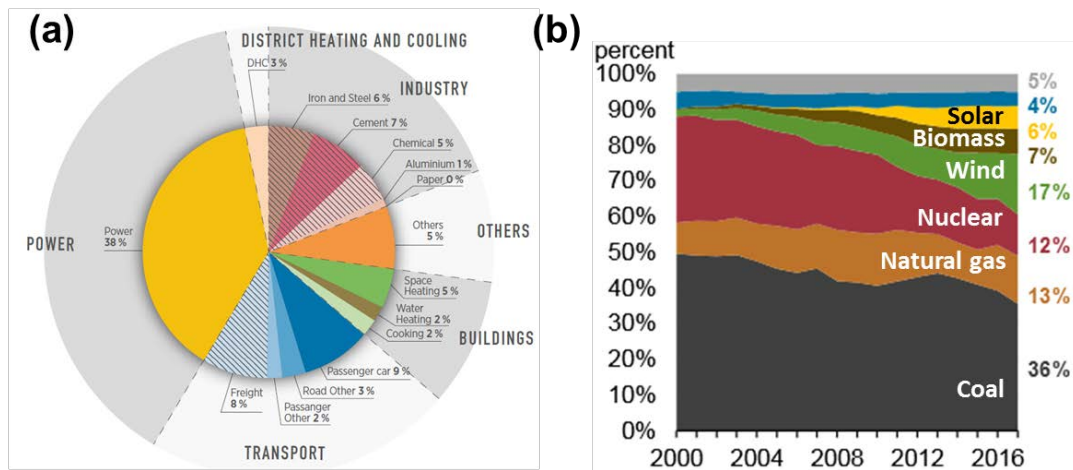
Figure 3. (a) Global CO_2 emission classified by the energy-related sector in 2015. Most of the CO_2 is generated by power plants.[31] (b) Energy sources for the electricity generation of Germany from 2000 to 2016 announced by German Association of Energy and Water Industries.[32]

The innumerable attention to the renewable energy market is recently skyrocketing globally, and the renewable energy sources are expected to be about 40% of the total power generation in 2050 as displayed in **Figure 4**.[33,34] China and India endow a lot to make solar photovoltaics the largest domestic energy source, and the European Union put their effort to transform 80% of new

energy capacities into renewable energies by 2030.[35] However, there are still many hurdles to adopting sustainable energy sources (power generation by solar, wind, tidal, or geothermal power) on a nationwide scale. Typically, the non-uniform distribution of these sustainable energy sources is pointed out as a key limitation such as sunlight availability for the photovoltaic system as described in **Figure 5(a)**.[36–38] In addition, because the power generation using solar or wind power decreases on cloudy days without wind, its availability is significantly influenced by the weather conditions that change from time to time. As described in **Figure 5(b)**, such unstable fluctuation and time discrepancy of renewable energy production and thus need restrict the practical application as an energy supply source on both a city and country-wide scale, which in addition continuously requires a certain supply of energy.[39,40] For example, the peak energy supply is usually reached at the midday of summer, but the peak energy demand reaches in the evening during the winter, respectively). To solve this problem, an auxiliary energy storage system (EES) capable of saving or using excess power generated from renewable energy sources is essential to accomplish a flexible, reliable, and less carbon-emissive power system.[39,41,42] In other words, the development of efficient EESs is a cornerstone that can accelerate the introduction of zero-emission energy generation. The development of EESs is also beneficial for people dependent on the use of fossil fuels. In the case of electric vehicles, which are currently seen as the future solution for individual transportation, CO_2 emission during operation can be drastically reduced compared to conventional combustion engine automobiles. Due to governmental policies and market needs, global carmakers are currently investing into the electric vehicle market to respond to the demand against global climate change. For example, Volkswagen Group plans to invest 15 billion euros over five years by 2024, while BMW Group

plans to invest 30 billion euros in research and development (R&D) by 2025.[43] In addition, the price of electricity produced by renewable energy sources is currently already below the price for electricity from fossil fuel resources.
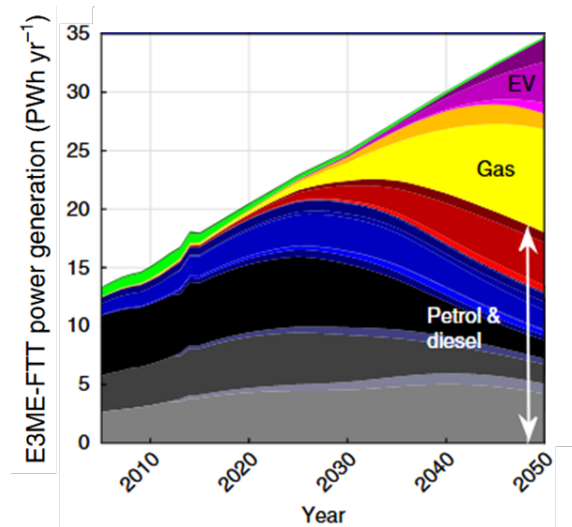
Figure 4. Simulation-based energy-economy-carbon-cycle-climate model (E3ME-FTT) projection for world electricity generation (in PWh yr^{-1} units) until 2050 classified by power generation type. Images are redrawn from reference. Copyright 2018, Springer Nature.[33]

Rechargeable batteries are a key component for the application as mentioned above. Currently, lithium-ion batteries (LIBs) and supercapacitors are utilized for most electrochemical energy storage applications due to their high current efficiency and comparably low cost per stored energy.[44] Nevertheless, there are challenges to adopting one system alone for all given applications. For example, new concepts for alternative energy storage devices should be developed instead of LIBs which have insufficient power density and suffer from limited long-term stability. Supercapacitors, in turn, do not provide sufficient energy density for most applications. An adequate combination of different electrochemical energy storage devices can

be a promising strategy. One such example is lithium-ion capacitors in which a battery-type electrode and a supercapacitor-type electrode are combined within one and the same device. Within this thesis, materials chemistry is used for the further development of one of the new alternative systems and to understand how optimized performance can be achieved by advanced electrode materials, namely all-carbon hybrid composites with porous lithiophilic sites. Through this, it will become possible to take one step closer to store and supply energy from renewable sources and by that reducing greenhouse gas emission.
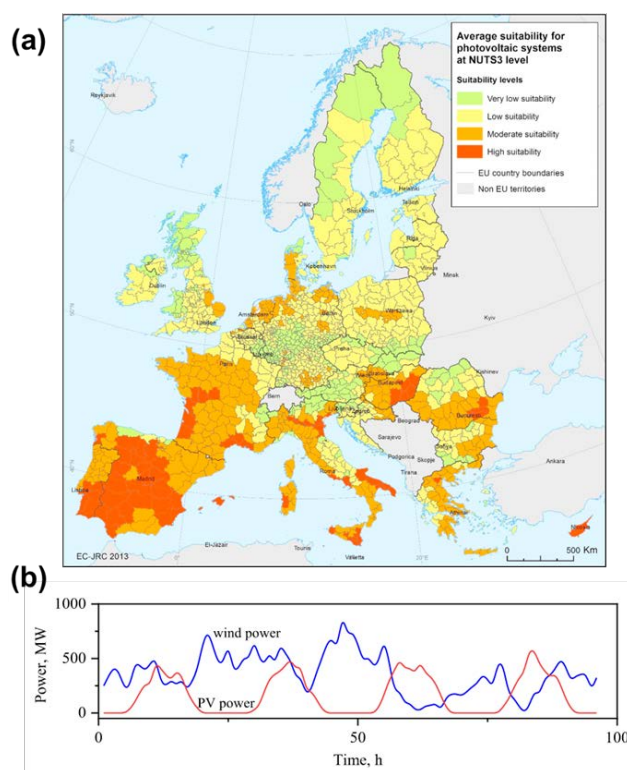
Figure 5. (a) Regional distribution of suitability levels for the installation of large-sized photovoltaic cells in Europe. From green to red, solar energy sufficiency is increased. Copyright 2016, Elsevier.[38] (b) Renewable energy generated by wind (blue) and solar (red) power at Jarud Banner point (43°50'-45°50'N, 119°14'-125°57'E) during 4 days with sunny weather. Copyright 2020, American Chemical Society.[40]

1.2 State-of-the-art

1.2.1 Porous carbon materials

The chemical element carbon is one of the most remarkable ones in the periodic table because it can exist in various forms with significantly different chemical bonding motives, physicochemical properties, and structures as summarized in **Figure 6**. There is a long history behind this element. Carbon was firstly synthesized in the universe by a nuclear fusion between ^{3}He/^{4}He atoms during the 'Big-Bang' or the formation of a star. Especially near the end of the life of a star, a depletion of hydrogen as a main fuel for the nuclear fusion leads to the accumulation of ^{3}He and ^{4}He, triggering the formation of ^{12}C along with other elements including beryllium, oxygen, and iron (the most stable nuclei).[45,46] The word 'carbon' is named after the Latin word meaning 'coal', and it always existed along with the history of the human beings as a form of food, clothes, and tools. The diversity of carbon compounds originates from the moderate electronegativity (~2.5) and the four valence electrons of carbon atoms. For instance, tetravalent valence electrons enable carbon to exist stably at different oxidation states from -4 (e.g. CH_4) to +4 (e.g. CO_2). As there is a tendency for the formation of covalent bonds to elements with a similar size and electronegativity and the possibility of sp, sp^2, and sp^3-hybridization of carbon atoms,, the carbon atom can covalently connect to an enormous diversity of atoms including H, Li, N, O, and Cl. This broad chemical functionality leads to a vast diversity in terms of structures that carbon atoms can form.[47,48] Consequently, carbon-backboned compounds can be found especially in organic molecules and macromolecules such as natural and artificial polymers with various lengths and configurations. Carbon-based inorganic materials also play a crucial role due to their often high abundancy, high

chemical/thermal stability, good electrical conductivity, and tunable structure and morphology which makes them attractive for versatile applications.[49,50]
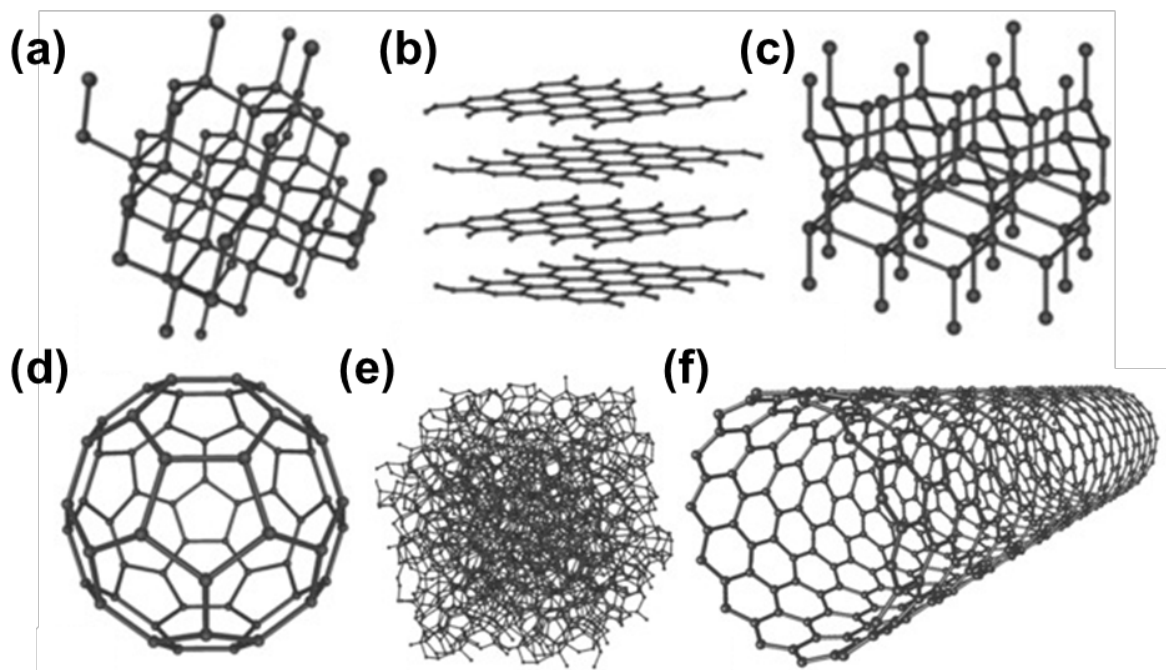
Figure 6. Different carbon allotropes: (a) diamond, (b) graphite, (c) londsdaleite, (d) fullerene, (e) amorphous carbon, and (f) carbon nanotube (CNT). Images are redrawn from reference. Copyright 2021, Elsevier.[51]

Interestingly, carbon exists in various forms of allotropes based on the fundamental sp^2-hybridized graphite (layered hexagonal structure) and sp^3-hybridized diamond (tetragonal cubic structure).[52,53] These allotropes consist of carbon entirely, but have different chemical bonding structures resulting in differentiated physical and chemical properties. For example, diamond is a transparent insulator (i.e. it has a wide bandgap energy) with outstanding hardness, while graphite is a dark-colored soft electric conductor due to the presence of delocalized electrons in the π-resonance system.[52] Even recently, different types of carbon allotropes with a nanometer-

sized structure such as nano-diamond, fullerene, carbon nanotube (CNT), and graphene are being discovered, synthesized, and investigated. Due to their outstanding and unique properties, carbon nanomaterials attract considerable attention not only from the academic field but also from industry. For example, fullerene (C_{60}) is a 0-dimensional "all-carbon soccer ball" with the combined structure of pentagons and hexagons composed of 60 carbon atoms.[54,55] Fullerenes and their derivatives (e.g. C_{70} or chemically functionalized fullerenes) can cage a guest metal or molecules (e.g. water, lanthanum, or other fullerenes) into their internal hollow void. In photovoltaics, fullerene-containing polymers are widely used because fullerenes effectively capture excited electrons generated by solar radiation.[56,57] 1-dimensional CNT and 2-dimensional graphene also show extraordinary properties. Both consist of sp^2-hybridized carbon, so they have outstanding anisotropic electric conductivity because of delocalized electrons in π-orbitals.[58,59] Especially, graphene which is a single layer of graphite has ultra-high mechanical strength, high transparency (2.3% of light absorbance per one layer), and magnificently large specific surface area (~2630 m^2 g^{-1}) at the same time.[60–62] Dedicated to the fundamental understanding of new findings from physical/chemical phenomena based in these carbon allotropes, Nobel prizes in chemistry (1996, Fullerene) and physics (2010, Graphene) have been awarded.

Based on the different long-range ordering, carbon materials also can be divided into crystalline and amorphous carbon.[63] Crystalline sp^2-carbon generally shows improved electrical conductivity and physical properties than amorphous ones. Carbon materials with crystalline structure thus have been utilized as catalysts and electrodes since the 1960s. However, amorphous carbon is also essential thanks to the low synthetic cost, high potential of structural

tuning, and various possibilities for chemical functionalization at defective microstructures.[64–66] Especially, as amorphous carbon can be prepared with high porosity and surface area, it has been extensively adjusted in versatile fields such as gas adsorption, water purification, catalyst supports, and electrochemical devices.[50,67–78]

When the carbon materials possess porosity in the structure, they are named porous carbon materials. From a structural point of view, a pore can be defined as a cavity with a depth that is larger than its width. Due to the large surface area and the enormous possibility of tuning the pore architecture or chemical functionality, porous carbons attract a lot of attention over a wide range of applications. As all other porous materials, carbons are also generally classified based on technical report of IUPAC (International Union of Pure and Applied Chemistry) as three different sorts depending on the pore size: macroporous (pores larger than 50 nm), mesoporous (pores between 2 and 50 nm), and microporous (pores less than 2 nm).[79] In case of micropores, they can be further classified as super microporous (pores between 0.7 and 2 nm) and ultramicroporous (pores less than 0.7 nm).

Nanostructured porous carbon exhibits unique properties which are not observed for the non-porous counterparts. This is mainly resulting from the different local bindings originating from the pore structure change and the interfacial properties.[78] If these pores are even hierarchical (i.e. a combination of pores of two or more different size regimes), the specific surface area of carbon materials and the mass transport properties of carbons can be strengthened at the same time.[80] Small pores in carbon materials in the size range of the molecules or ions to be adsorbed do generally enhance the adsorption enthalpy of the guest species and in some cases also the adsorption capacity.[81–85] In conclusion, various approaches such as activation and templating

have been developed and optimized for the synthesis of nanostructured carbon materials with defined pore architectures.[86–88] The pore formation by carbon activation is one of the well-established techniques and makes use of physical (e.g. CO_2, air, and steam at elevated temperature) or chemical agents (zinc chloride, phosphoric acid, potassium hydroxide).[81,89–91] Due to the low processing cost, it is beneficial to adopt in an industry-scale synthesis. However, the limitations of physical activation (large energy consumption and low yield) and chemical activation (excessive formation of functional groups and additional reaction steps) limit industrial application to low-price applications.[81,92,93] In addition, the pore shape of activated carbon is a major drawback because the materials generally have a relatively broad pore size distribution often with a worm-like bottleneck morphology (i.e. they consist of poorly connected pore systems), resulting in low mass transportation rate and unselective adsorption. The latter is a particular disadvantage for size-exclusive filtration of specific target molecules.[94–96]

As an alternative approach, templating strategies are widely applied for the synthesis of designer carbon materials in recent years as they can overcome some of the limits observed in the activation method. In particular, the templating method allows precise pore size control with high uniformity and facile manipulation of the desired pore shape.[94,97] The whole process generally follows three sequences similar to the bulk casting as shown in **Figure 7**.[50,98] Firstly, the carbon precursor and templates, which are "structure-directing" casting materials (such as zeolites, mesoporous silica, silica nanoparticles, and anodized alumina membranes), are mixed together to form a nanoscale composite material. This is followed by carbonization.[99] Finally, the template materials are removed chemically and a well-defined pore size distribution is achieved. When the template is removed after the carbonization, the formerly occupied volume

turns into pores in the structure. In this regard, the final pore architecture including the pore size and pore volume is heavily dependent on and can be dictated by the structure and type of templates. Among other methods for pore generation, the templating strategy provides highly connected pore networks and the possibility to further functionalize the final carbon product for various applications.[75,100–104] In other words, the design of specific pore systems and parameters for carbon materials is easily tunable by templating for a targeted use.[105] Because each application requires different porosity architectures (total pore volume, specific surface area, and pore size distribution), it is important to find particular conditions and a balance among them. For instance, the total pore volume (V_{Total}) often influences the loading capacity of porous carbon as a conductive host for catalysts or within electrodes.[94] Meanwhile, the high specific surface area (SSA) is beneficial to surface-dependent applications such as supercapacitors,[94,106] and the pore size distribution affects adsorption selectivity and mass transportation rate which is for instance crucial to achieving improved rate capability for electrochemical energy storage applications.[107] In conclusion, the manipulation of pore parameters as well as the understanding of "performance-structure relationships" is significantly vital to figure out what the optimized pore design is and to determine which pore generating strategies are most suitable for specific applications.

The templating syntheses can be classified into three different main categories: soft-templating, hard-templating, and salt-templating.[108] The soft-templating method utilizes soft template materials like polymers, whereas hard-templating method generally adopts inorganic materials as templates. The carbon precursors are then embedded in the soft-/hard-/salt-templates and transformed into porous carbon after the sequential carbonization and removal of templates.
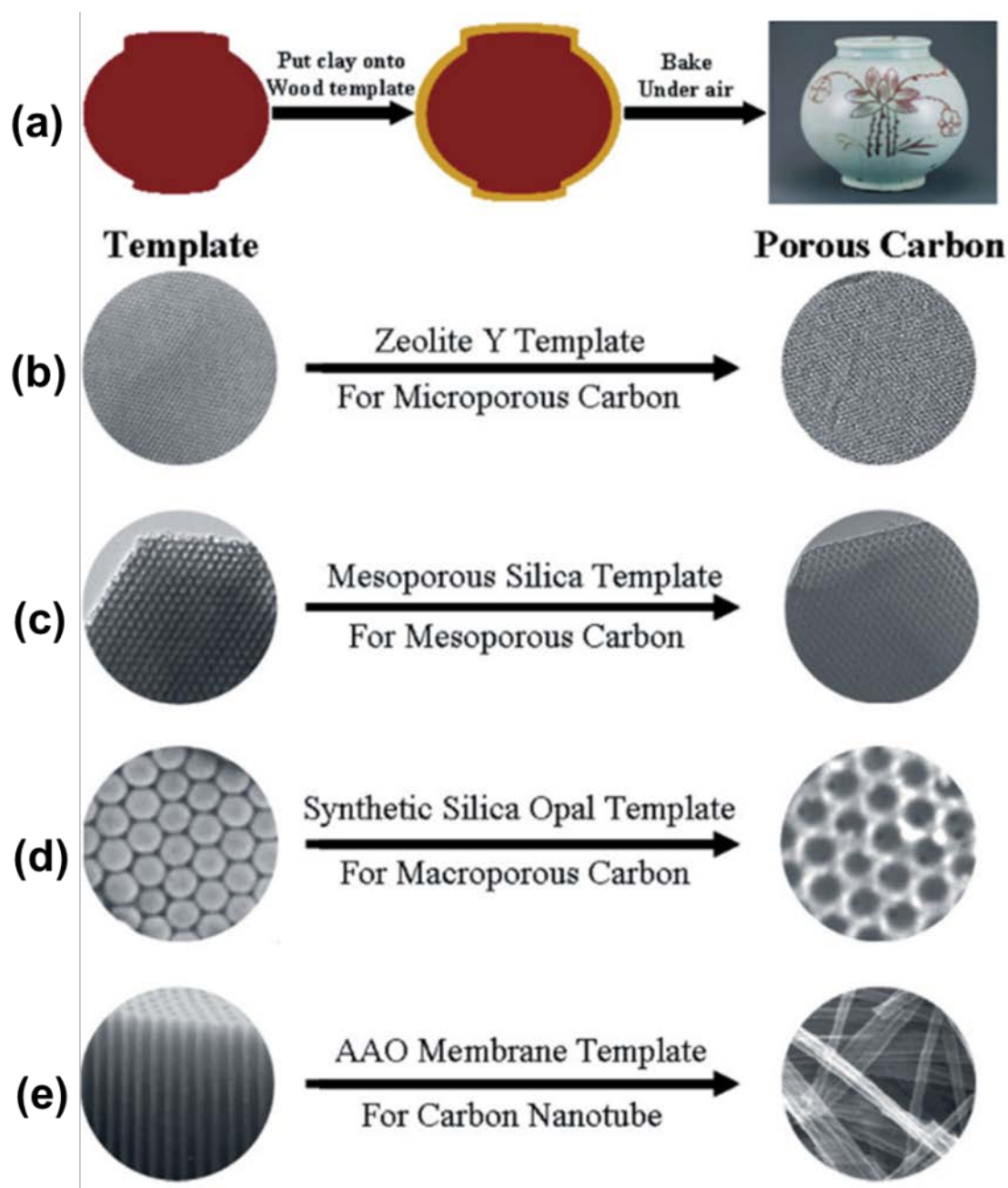
Figure 7. (a) Principle of the synthesis for porous carbon materials using templating methods. Porous carbon materials from the suitable templates containing (b) micropores, (c) mesopores, (d) macropores and (e) fibrous structures, respectively. Image is redrawn from reference. Copyright 2006, John Wiley and Sons.[50]

Soft templating method adopt the self-assembly of amphiphilic molecules/polymers in solution as depicted in **Figure 8**. During the self-assembly, the combination of comparably weak intermolecular forces (e.g. dipole-dipole interaction, hydrogen bonding, dispersion force, and electrostatic interaction between charged functional groups) are the major driving forces for the process.[109] After the formation of a non-rigid self-assembled structure, added carbon precursors (e.g. sucrose) deposit onto the surface of the template and then undergo condensation or crosslinking. The final carbonization leads to porous carbon materials after the removal of the template by heat-treatment or dissolution. Consequently, the pore system and the pore geometry of the produced carbon are easily tunable by changing the template structure or the ratio of the template to the carbon precursor.[110] Well-known starting materials for soft templating that can undergo the self-assembly in solution are surfactants like cetyltrimethylammonium bromide, or block copolymers consisting of hydrophilic and hydrophobic blocks at the same time (e.g. the block copolymer called P123).[111] These molecules form ordered and thermodynamically stable structures (e.g. micelles or lamellar structures) depending on concentration and temperature conditions.[112,113] The most notable material fabricated by this method is ordered mesoporous MCM-41 (Mobil Composition of Matter) silica with hexagonally ordered pore structure.[114] Even though the soft-templating strategy enables high reproducibility and precise control of pore architecture with a relatively simple template removing process, the various applications of resulting porous materials are limited due to the low specific surface area of usually less than 1000 m^2 g^{-1}.[99]
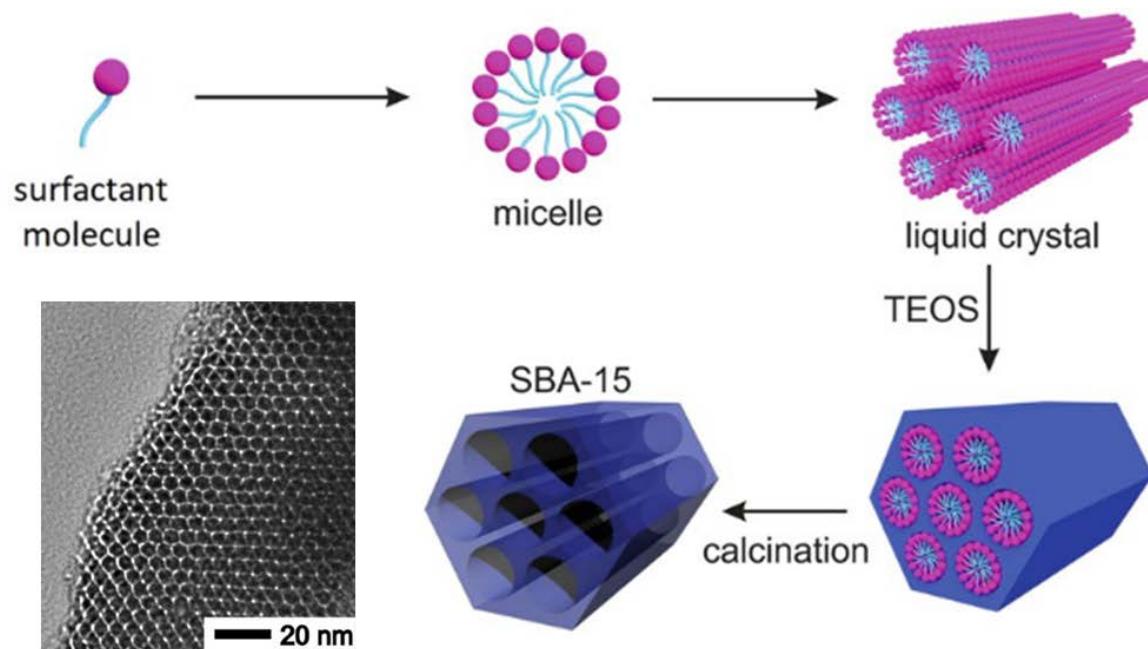
Figure 8. Schematic illustration of a soft-templating synthesis and transmission electron microscopy image of fabricated SBA-15. Image is redrawn from reference. Copyright 2019, Springer Nature.[115]

Hard templating utilizes an existing pore structure of rigid templates which function as a mold in "nanocasting".[98] The nanoscale porosity of the hard-template is used as space to immobilize the carbon precursor material. Firstly, the pore network of the template is filled with carbon precursor (infiltration). This is subsequently followed by carbonization and template removal steps.[116,117] That is, void cavities of the template infiltrated with precursors are transformed into carbon. As a result, the pore morphology, pore connectivity, and pore size are directly determined by the template because the final carbon product represents the inverse replica of the cast.[118] The most prominent ordered mesoporous carbon materials are prepared by silica-based hard-templating methods: the 2-dimensional hexagonal ordered mesoporous carbons (CMK-3,

the inverse copy of ordered mesoporous SBA-15 silica, **Figure 9(a)**),[119–121] and 3-dimensional cubic ordered mesoporous carbons (CMK-8, the inverse copy of ordered mesoporous KIT-6 silica, **Figure 9(b)**).[118,122] .SBA, KIT, and CMK stand for Santa Barbara Amorphous, Korea Advanced Institute of Science and Technology (KAIST), and Carbon Mesostructured by KAIST, respectively. Even though the pore design of these silica-templated mesoporous carbons is easily adjustable, the insufficient infiltration to complicating nanopores and the harsh removing process of silica (e.g. washing with hot concentrated NaOH aqueous solution, or with hydrofluoric acid which is highly toxic) are pointed out as major drawbacks. In this sense, hard templates from metal oxides such as zinc oxide (ZnO, which can be easily removed by acidic solution or heating at high temperature) are suitable alternatives to silica-based templates. In detail, taking ZnO-templated carbon as an example, ZnO undergoes a carbothermal reduction reaction with carbon during the carbonization step. (**Eq. 1**)[108,123]

$$ZnO_{(s)} \; + \; C_{(s)} \; \rightarrow \; Zn_{(g)} \; + \; CO_{(g)} \quad (\textbf{Eq. 1})$$
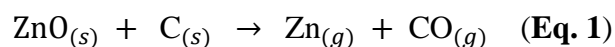
As the carbon pyrolysis temperature is higher than the boiling point of zinc, Zn is removed through evaporation to the gas phase. Interestingly, released CO gas during the carbothermal reaction also generates additional pores that are then interconnected with existing mesopores produced by the ZnO template.[123] However, it is intricate to be applied in mass production due to the costly and time-consuming procedures, even though hard-templating allows precise control over the pore structure of carbon products.
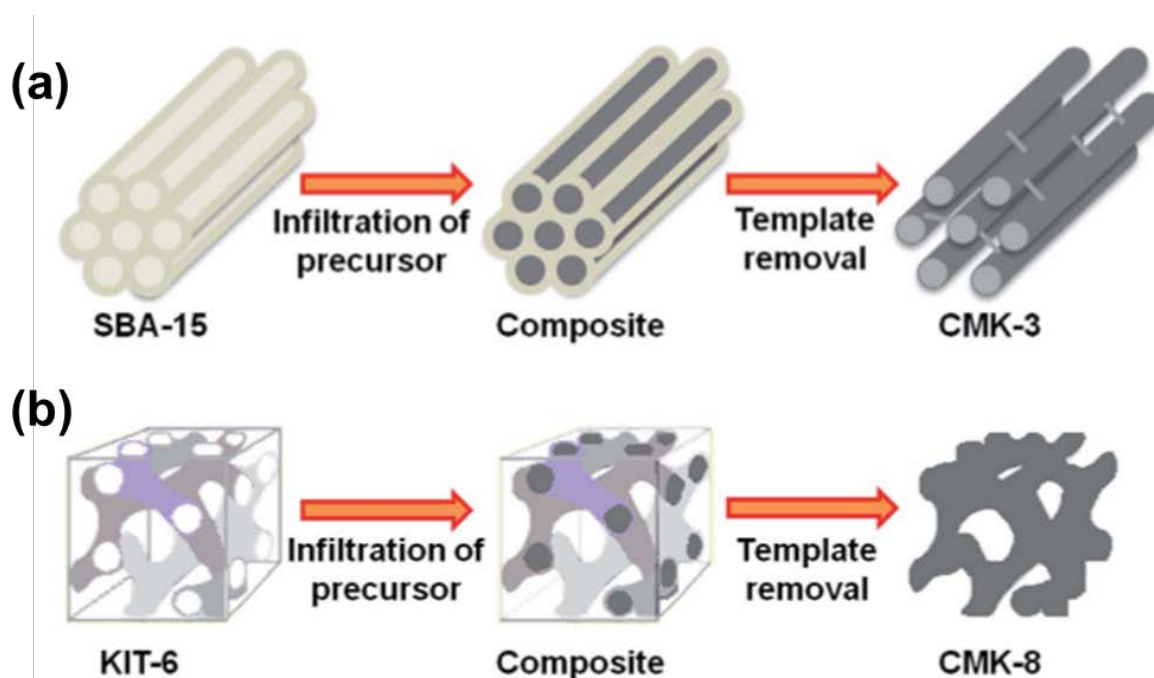
Figure 9. Schematic illustration of the hard-templating method for the synthesis of (a) CMK-3 fabricated from hexagonal SBA-15, and (b) CMK-8 fabricated from cubic KIT-6. Image is redrawn from reference. Copyright 2011, Royal Society of Chemistry Publishing.[121]

Salt templating adopts a medium of salts (e.g. molten salt, eutectic mixture, ionic liquid) as a cast. Dissolved carbon precursors then accumulate around the salt to create highly porous carbon materials after the poly-condensation and carbonization at elevated temperatures as depicted in **Figure 10**.[124] For example, the combination of metal halides (such as LiCl/ZnCl$_2$) with various carbon precursors is widely used due to the high stability, melting point, recyclability, and water solubility of these templates.[125] Similarly, pyrolysis of glucose also can be carried out in an eutectic LiCl/KCl mixture under inert atmosphere. Unlike soft- or hard-templating, the ions of the salt template can be easily removed washing with a proper solvent. The synthesized porous carbon materials remain after washing, and they usually have well-defined porosity with high

surface area and chemical/structural functionality.[93,126] This is beneficial especially for inducing ultramicro-/micropores without harsh washing conditions of difficult template synthesis. As the amount of templating agent (i.e. the ratio of salt vs. carbon precursors) and their chemical nature distinctly alter the resulting carbon morphology and porosity, they can be adjusted easily to achieve a specific pore architecture.[127–129] Additionally, the hierarchical pore structure can be prepared from the salt-templating technique by hybridizing with other soft-/hard-templates or activation processes.[130,131]
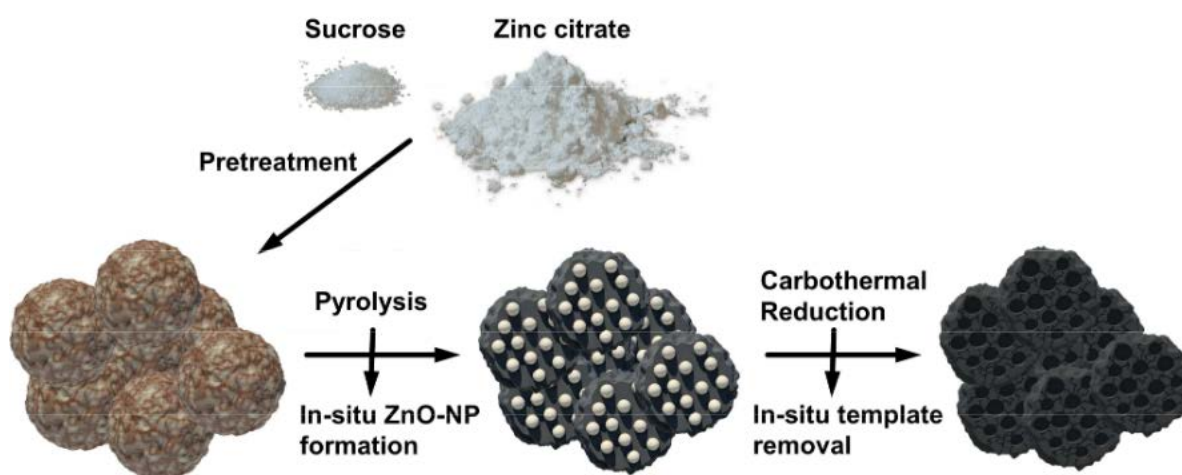
Figure 10. Schematic illustration of the salt-templating method using sucrose, zinc citrate, and ZnO nanoparticles. Copyright 2016, Elsevier.[124]

## 1.2.2 Lithiophilic nitrogen-containing porous carbon materials

One of the unique characteristics of carbon-based materials is that their chemical and surface properties can span over a wide range depending on the nature of chemical bonds and functional groups.[132–135] As a carbon atom has medium electronegativity and four valance electrons, it can

form covalent chemical bonds with a large range of different atoms. Doping of heteroatoms such as B, N, O, F, S, and P is therefore on straightforward option for the further functionalization of porous carbon materials.[136,137] Among these various atoms, doping by nitrogen (N-doping) often results in a remarkable change in performance compared to non-doped pristine carbon in various applications including supercapacitor electrodes, supporting materials for catalysts, and metal-free catalysts.[138–140] This is because the electronic structure and the distribution of electron density are influenced a lot after the insertion of nitrogen into the carbon matrix. As a result, various techniques have been reported to introduce nitrogen-containing functional groups for the fabrication of N-doped porous carbon. Examples of well-known methods include (1) the post-treatment (mostly heat-treatment) of a mixture containing the as-synthesized porous carbon and nitrogen-rich precursors (e.g. urea, melamine, nitric acid, methyl cyanide),[141,142] (2) gas-phase deposition by using reactive nitrogen-providing species (e.g. NH_3 or cyanamide),[143] and (3) condensation or pyrolysis of nitrogen-containing sources to form the porous carbon framework within a direct synthesis (e.g. various molecular precursors to C_2N-carbon or simply glucosamine to porous N-doped carbon).[142,144–146]

However, the facile implementation of a well-defined pore structure and homogeneous distribution and chemical binding motives of nitrogen species on the nanoscale is still pointed out as a complicated task for the synthesis of advanced N-doped porous carbon. For example, NH_3 deposition in method (2) may decrease the pore volume and surface area at the same time caused by ammoxidation.[147] It triggers non-homogeneous nitrogen distribution, leading to unstable doping and a wide variety of different properties within the N-doped carbons. On the other hand, the combination of the synthesis of N-doped carbons with templating approaches

consumes lots of time and needs many steps to achieve well-ordered N-rich porous carbon with even pore size.[148] Taking these challenges into consideration, the use of simple heat-treatment (1) with adjustable nitrogen-containing precursors can serve as a rather reliable and reproducible preparation method for N-doped porous carbon materials.
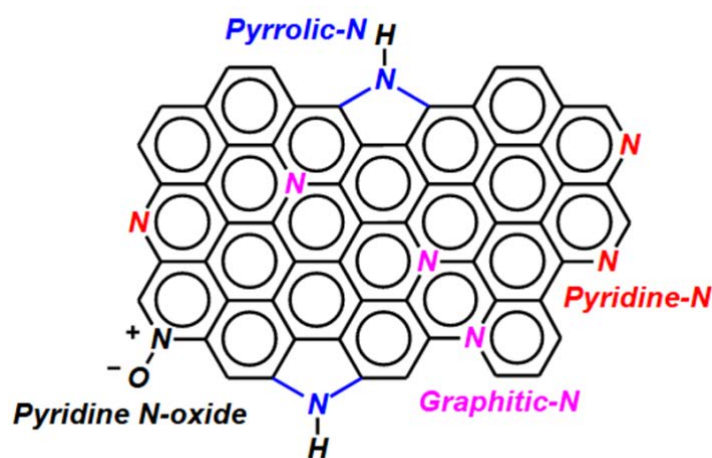
Figure 11. Possible binding sites for nitrogen heteroatoms on a graphitic carbon lattice: pyridinic (red), pyrrolic (blue), graphitic (pink), and pyridinic N-oxide (black) sites. Copyright 2019, John Wiley and Sons.[149]

From an atomic binding point of view at the molecular level, carbon atoms are substituted or nitrogen atoms are inserted into the carbon framework, resulting in pyridinic, pyrrolic, and graphitic nitrogen sites after the doping as depicted in **Figure 11**.[149] The specific structure of the nitrogen doping sites formed during the synthesis is largely dependent on the type of nitrogen precursor and the nitrogen content. As the inherited properties of carbon (such as surface polarity, wettability, electrical conductivity, acidity/basicity, chemical stability, and electrochemical activity) are affected by the doping sites and degree of doping due to the change of chemical/electronic structure, nitrogen-rich carbons are highly tunable and their properties can be

varied corresponding to the doping method.[139,142] For instance, higher stability against the oxidation reaction is reported for N-doped carbon materials compared to that of the pristine carbon in many studies.[133]

Heteroatom doping also influences the interaction between the carbon and any guest species to be adsorbed on its surface. Such strengthened binding based on nitrogen can be adopted for electrochemical applications.[150–153] Considering lithium (Li) ions, the reversible charge transfer of Li-ions on N-rich porous carbon can lead to improved dispersion and stabilization because especially electron donating nitrogen sites play the role of "lithiophilic" anchoring points with increased binding enthalpy between Li-ions and the surface of the carbon-based material.[135,136,154,155] Generating a high density of N-rich "lithiophilic" sites by chemical functionalization is thus a powerful strategy to optimize the adsorption capacity towards lithium atoms. However, there seems also an optimized density ("trade-off") for the formation of lithiophilic sites. It is a critical consideration that too high nitrogen contents (i.e. too high doping ratio) can result in reduced structural stability of carbon matrix and severe changes in electron density with notable influence on electronic conductivity and its Fermi level.[156,157] In addition, the particular nitrogen sites (pyridinic, pyrrolic, graphitic) in the carbon lattice also determines the activity of N-rich carbon materials.

1.2.3 Lithium-ion batteries (LIBs)

Since the pioneering research on LIBs during the 1970s and their commercialization in the 1990s, LIBs have dominated the rechargeable secondary battery market over any other energy storage

devices. This reality was started from the prototype development in 1985, and related commercialization was largely initiated and attempted by R&D projects from global companies in the 1990s.[158] Even though few commercial products were successful at that time, they triggered the development of further advanced energy storage devices based on a variety of electrochemically active compounds including Li-sulfur,[159] Li-air,[160] and Na-ion batteries.[161] Nowadays, LIBs are found not only in small portable devices but also in larger objects driven by electric energy such as electric vehicles. The breakthrough has been achieved when the unstable Li metal-based electrode ($E^o(Li/Li^+)$ = -3.04 V vs. standard hydrogen reference electrode) has been replaced to safer Li-intercalating carbon anodes with a prolonged lifespan, and the transition metal oxides or sulfides have been utilized as cathode with high reversibility during the continuous charge-discharge cycles.[162–164] The most common electrode materials now for commercial LIBs are lithiated graphite as anode, and carbon/$LiCoO_2$ composite as cathode, respectively.[165,166] Recently, based on this huge leap in the energy storage field, the contribution to the development of LIBs was recognized in Nobel Prize in Chemistry to John B. Goodenough, M. Stanley Whittingham, and Akira Yoshino in 2019.
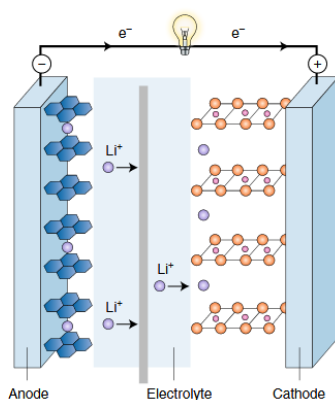
Figure 12. The cell structure of LIB during discharging. Copyright 2018, Springer Nature.[167]

The basic cell structure of LIBs consists of the cathode and anode materials, an electrolyte and a separator between the electrodes as described in **Figure 12**. The fundamental reaction that occurs in the cell is the reversible intercalation/deintercalation of Li-ions in the layered structures of the electrode materials. For instance, the reversible intercalation between $LiCoO_2/Li_{0.5}CoO_2$ occurs at the potential of 4.2 V vs. Li/Li^+.[168] Especially for graphite, this process provides prolonged cycle life and improved safety compared to Li metal electrodes. On the other hand, the intercalation of Li-ion in the carbon materials or graphite (theoretical capacity = 372 mAh g^{-1} at around 0.1-0.2 V vs. Li/Li^+) proceeds in various steps for the complex formation of different intermediates such as LiC_6, LiC_{12}, LiC_{24}, and LiC_{27}.[169] During the intercalation processes, a passivating layer called SEI (Solid-Electrolyte Interphase, as described in **Figure 13**) is formed on the electrode surface which limits reversible charging-discharging especially in the first lithiation and de- lithiation cycles in the typically applied aprotic polar electrolyte containing Li salt.[170,171] Once formed, the SEI layer increases the apparent stability of the electrolyte as well as the electrode by a passivating effect. Some portion of charge and energy are thus consumed due to the SEI layer formation at the electrode-electrolyte interface.[172] The energy that needs to be irreversibly invested for the formation of the SEI layer increases with the total interface area. As a result, an excessive amount of Li-ions is needed for the stable operation of LIBs, and materials engineering is crucial to reduce the irreversible charge consumption for SEI layer. In addition, a selection of the most suitable electrolyte (e.g. carbonate-based or ether-based electrolyte) and salt (e.g. $LiPF_6$) is also the key to improving the reversibility.[173,174]

enlargement of SEI source
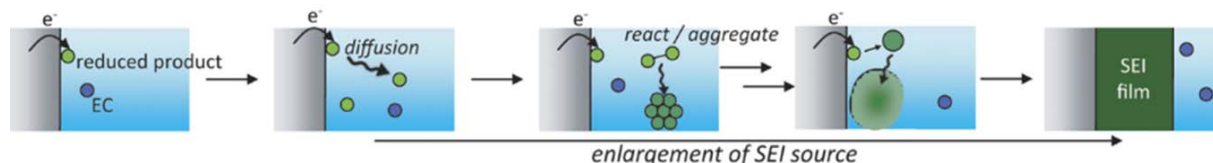
Figure 13. Proposed process of SEI layer formation, indicating the layer follows the near-shore aggregation mechanism. The reduced electrolyte molecules can accumulate and aggregate near the interface. This formed deposit on the electrode surface leads to the complete formation of SEI layer. Image is redrawn from reference. Copyright 2018, Springer Nature.[175]

Even though the advantages of modern LIBs include high specific energy (250-280 Wh kg^{-1}) and long cyclability (~10^3 cycles), there are still many troublesome points to overcome for this technology such as low charging rate, low power density, and possible safety problems.[176] Most of the cathodic materials utilized in commercial LIBs are inorganic materials (e.g. metal oxides or phosphates) while diverse combinations are applied for anodic materials including various carbon nanomaterials, Li metal, metal oxides, and Li alloys with Si or Sn.[177] To achieve fast-charging LIBs with enhanced specific power density for the next generation, improvement of the reaction kinetics at each electrode is required. Three major methods are obvious for that purpose: applying nanoparticles, surface modification, and fabrication of nanocomposites as shown in **Figure 14(a)**.[178,179] However, in the case of applying nanoparticles, the electrical conductivity of electrodes may be reduced and low stability can result from the self-agglomeration caused by large surface energy of the particles. On the other hand, surface modification such as coatings of conductive layers coating (e.g. carbon layers or conductive polymer coatings) may block the intercalation sites, resulting in decreased lithium storage capacity and thus energy density.[180]

The fabrication of nanocomposites is one of the most promising routes to develop improved LIBs. For instance, it already well known that core-shell structured nanohybrids show a synergetic effect for phosphate cathode materials, and the graphene-based oxides/phosphates decoration enhances high rate performance by forming well-dispersed composites at the molecular level as shown in **Figure 14(b)**.[178,181,182] Interestingly, among other carbonaceous materials, hierarchically porous carbon can support composites in many different perspectives. It helps to improve the rate capability performance at a high current level by providing mass transportation pathways (e.g. for Li^+ and counter-ions) and can serve as conductive layer, sometimes even without high-temperature thermal treatment. If redox active sites are present, it can even plays a significant role to increase the energy density by providing Li-storage sites inside the pores.[183–185] The microstructure of carbon-based composite electrodes thus strongly influences lithium storage performance.
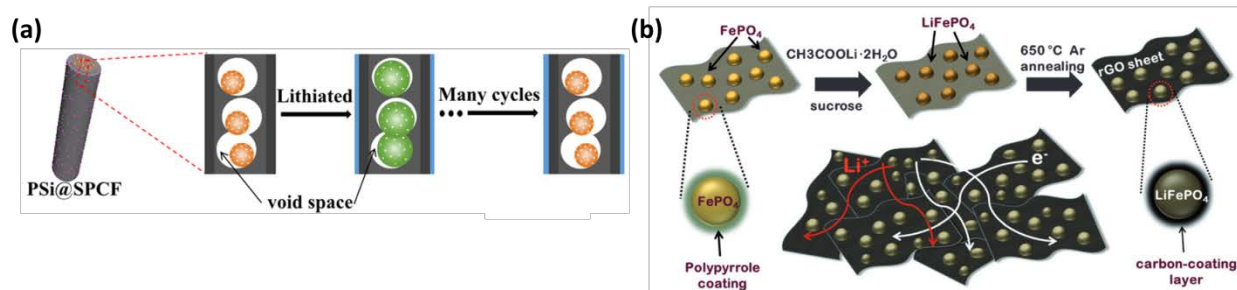
Figure 14. (a) Schematic illustration for composite consisting of porous silicon implanted in sulfur-doped porous carbon fiber (PSi@SPCF). Image is redrawn from reference. Copyright 2022, American Chemical Society.[179] (b) Schematic illustration for core-shell structured $LiFePO_4$/reduced graphene oxide composites as cathode in LIBs. $LiFePO_4$ in the composite is coated with carbon derived from thermally treated polypyrrole polymer. Image is redrawn from reference. Copyright 2014, John Wiley and Sons.[182]

Heteroatom doping (e.g. B, N, S, and P) of the electrode is another useful way to improve the cell performance by increasing storage capacity through the generation of active sites and in some cases electrical conductivity.[133,137,155] This strengthens electrode-electrolyte interactions, leading to enhanced kinetics of the electrochemical processes charging/discharging. However, even by combining the formation of hierarchical pore structure and heteroatom doping at the same time, it is intricate to overcome the problems of LIBs completely. To meet the new market needs for future energy storage systems, LIBs alone can most likely not achieve high energy density and power density at once. For this fulfillment, it is necessary to suggest novel alternative energy storage systems such as the hybridization of LIBs with other energy storage devices.

1.2.4 Electrochemical double layer capacitors (EDLCs)

In general, a capacitor is an energy storage device, consisting of two conductors (i.e., plate electrodes or terminals) which are divided by an insulating material. The charge stored at the surface of the conductive layer has the same number of charges at each electrode, but with a different sign. Depending on the purpose and the targeting application, various designs and sizes can be chosen.

In 1745, the first design of electricity-storing capacitors was proposed by Ewald Georg von Kleist (Germany) and Pieter van Musschenbroek (The Netherlands) independently. This invented design was named after the city 'Leiden', so it was called 'Leyden jar' as shown in **Figure 15**.[186] The inner part and outer part of the glass jar were both covered with metal foil

with the gap between each to prevent the contact which would lead to discharging or arcing of the cell. The conductive metal foil functions as electrodes (anode/cathode), and the glass filling between the two foils functions as a layer that is electrically insulating. Similarly, vacuum, aqueous/non-aqueous liquids, insulating inorganics or polymers can be utilized as dielectrics. When the jar is charged, electrons accumulate and form a negatively charged foil at the one side while the other side of the foil gets positively charged due to lack of electrons and corresponding accumulation of holes. These accumulated/induced charges are discharged when two electrodes are connected with an external circuit, generating electric current.

Figure 15. Structure of electrolytic capacitor prototype, "Leyden Jar". Copyright 1919, Longmans.[186]

In 1857, the German physicist Johann Heinrich Buff firstly observed the electric current generation from a metal oxide layer, and this phenomenon was utilized to fabricate the first electrolytic capacitor invented by Charles Pollak in 1896.[187] This electrolytic capacitor consists of aluminum/aluminum oxide electrodes with alkaline electrolyte as a dielectric layer. Early electrolytic capacitors were fabricated for radio-wave transmitters, wave frequency filters, and altering machine to change current circuits. The capacitor was then further improved in the 20th century with different metal electrodes, solid electrolytes, and various cell architectures.

Especially in 1957, the carbon-based electrolytic capacitor for low voltage operation was firstly proposed by H. Becker.[188] He put porous activated carbon onto aluminum foil, which was then immersed into the electrolyte and separated with a thin insulating layer as dielectric. This carbon-based capacitor was the earliest pioneer with carbon electrodes, generating a far higher capacitance (~1.0 F) than any metal-based electrolytic capacitor at that time per unit mass or volume. This became a fundamental design for many basic EDLCs nowadays.[189–191]

EDLCs are one of the various types of supercapacitors (along with pseudo-capacitors) and they store much more energy than conventional electrolytic capacitors. The capacitance value (per unit mass or volume) of EDLCs is 10-100 times larger than that of electrolytic capacitors.[192] The reason is that EDLCs store charge by reversible adsorption of ions in electrolytes at the electrode-electrolyte interface. This interface is called the electric double layer which was proposed in the 1800s by Helmholtz as described in **Figure 16(a)**.[193,194] Because the ions in the electrolyte rearrange at the interface to mirror the electrode charge make an electrically neutral state, polarized solvent molecules (Inner Helmholtz plane, IHP) and solvated ions (Outer Helmholtz plane, OHP) form a double-layered structure. The formed IHP monolayer separates electrodes from ions in the electrolyte. Consequently, the coulomb charges can be stored within the electric double layer.[193,195] As the distance between the electrode and ion-containing electrolyte layer in EDLCs is on the angstrom (Å) scale, superior capacitance values can be achieved compared to the conventional electrolytic capacitor.[191,196] Thus, the electrically polarized interface can interact with ions easily by electrostatic forces at the electric double layer as shown in **Figure 16(b)**.[197,198] This surface adsorption/desorption process is generally faster than sluggish redox reactions, which are commonly utilized in secondary batteries or pseudo-

capacitors.[199] Compared to LIBs introduced in **Chapter 1.2.3**, EDLCs show a higher rate of charge and discharge and superior chemical stability of the cell.[200] Consequently, the outstanding rate capability and stability enables EDLCs to provide high power density as well as improved cyclability even at high or low operating temperatures.[201,202] The advantage of short-term energy storage and releasing process leads to the application of EDLCs into various fields such as starting engines for electric vehicles (car, bus, and tram), moving initiators for bicycles or elevator operation, and emergency brakes which need a large amount of power within short time range.[190] Even though EDLCs have rapid charging/discharging cycles, their low energy density (~10 Wh kg^{-1}) limits their further commercial application.[203] Therefore, previous researches for EDLCs have been focused on the improvement of energy density without losing its unique characteristics. Efforts into this direction mainly focus on two routes: the development of (1) development of electrolytes with a broad voltage stability window and (2) novel electrode materials with enhanced ion storage capacity.
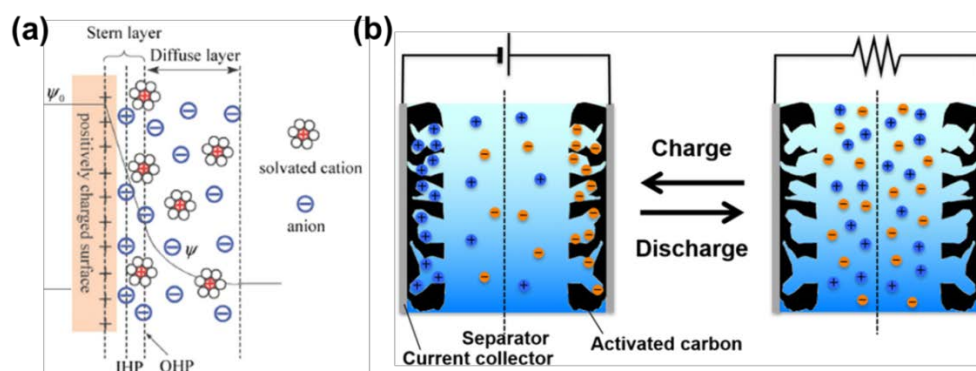
Figure 16. (a) Electric double layer structure with IHP and OHP at the electrode interface. Image is redrawn from reference. Copyright 2009, Royal Society of Chemistry.[194] (b) Schematic diagram showing the general mechanism of EDLCs during charging/discharging. Copyright 2019, Springer Nature.[197]

Electrolytes for EDLCs can be classified as liquid and solid electrolytes, and liquid electrolytes can be further classified as aqueous (acidic, basic, neutral) and non-aqueous electrolytes. However, due to the narrow voltage window of aqueous solution (general voltage window for aqueous solution = 1.5-2.0 V including the overpotential needed for water splitting), it is hard to achieve high power or energy density with aqueous electrolytes even though they have the advantage of high solubility of ions, high ionic conductivity, and high polarity. Therefore, the non-aqueous organic electrolyte are preferred to broaden the operating voltage window (up to 4.0 V), because the energy stored in the capacitor (E) is proportional to the capacitance (C) and the square of operation voltage (V): [204]

$$E = \frac{1}{2} C V^2 \quad \textbf{(Eq. 2)}$$

The organic electrolytes, however, may cause safety problems due to their high toxicity and volatility with a high possibility of explosion. In some cases, they are not suitable for high-voltage operation which brings the risk of overheating of EDLCs.[189] To overcome the problems of non-aqueous electrolytes, non-volatile ionic liquids such as chemicals in **Figure 17(a)** are proposed as promising alternatives. Ionic liquids have large voltage window and operational temperature ranges at the same time with less possibility of explosion. Even though the advantages of ionic liquids, they have comparably high cost and viscosity which hinders ionic transportation in electrolytes and at the electrode interface especially when it has a hierarchical structure. The utilization of ionic liquids is thus in some cases impractical due to the lagging ion dynamics, resulting in low power density.[205] To address the problems of liquid-based electrolytes of EDLCs, solid electrolytes are recently investigated as future-promising candidates. Ion-conductive polymers or defect-rich conductive inorganic materials are applied to reduce the

instability of liquid-based EDLCs and improve the power density. However, the comparably sluggish ionic conductivity of inorganic solid materials or polymers, weak mechanical properties, and high cost are pointed out as remaining challenges of all-solid EDLCs.[206] Recently, gel electrolytes for EDLCs such as **Figure 17(b)** are also largely investigated for the development of flexible EDLCs.[207–209]
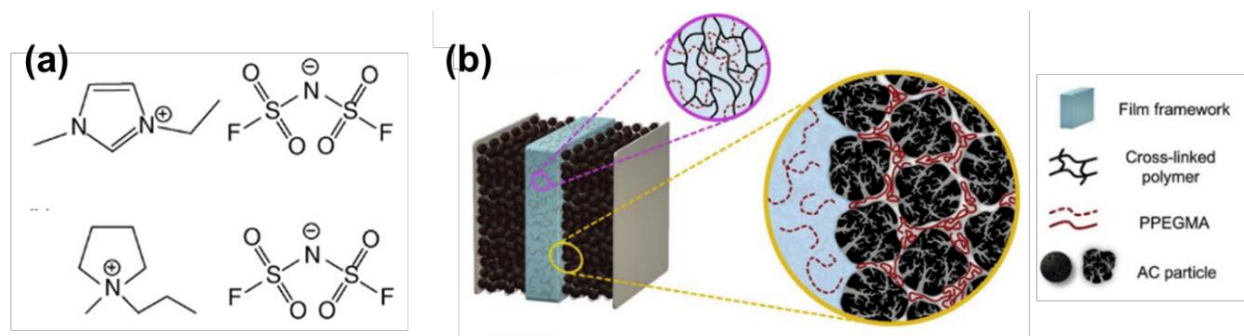
Figure 17. (a) Examples of ionic liquids commonly adopted in energy storage devices: 1-Ethyl-3-methylimidazolium bis(fluorosulfonyl)imide (above), *N*-methyl-*N*-propylpyrrolidinium bis(fluorosulfonyl)imide (below). Copyright 2006, Elsevier.[210] (b) Schematic structure of quasi-solid-state EDLCs with activated carbon electrode and amphiphilic poly[poly(ethylene glycol) methacrylate] (PPEGMA) gel electrolyte. Image is redrawn from reference. Copyright 2020, Elsevier.[209]

For the improvement of the carbon electrodes, various carbonaceous materials have been proposed. As carbon-based materials have a high surface area, chemical/electrical stability, and electrical conductivity, they are the materials of choice for the application in EDLCs. From an engineering point of view, they are also attractive because carbon materials are earth-abundant, non-toxic, and can be manufactured in relatively easy processing steps with comparably low cost. Advantages of carbonaceous materials attracted their application to electrodes, and thus various types of carbon (e.g. porous carbon, CNTs, graphene) have been investigated as electrodes for

supercapacitors. As the surface area plays a crucial role in EDLC electrodes, the tuning of porosity and related pore structure of carbon materials received intense attention and attempts were made not only to tailor them on the mesopores scale, but also on the micro/ultramicropore scale.[94,211] Based on previous reports, the porosity of carbon has a significant influence on their rate capability and the value of specific capacitance which are the two major descriptors for the quality of EDLC electrode materials. The first aspect is the effect of micropores whose pore diameter is comparable to the size of ions in the electrolyte. When the solvated electrolyte ions including their solvation shell approach to the pore, the ions inside the shell can strongly be adsorbed on the carbon pore walls with interactions from both sides and thus be soaked into the pore walls. Because there is the high electrostatic interaction between the ions inside the shell and the polarized carbon pore walls, and adsorbed solvation shell can be partially or fully stripped off due to the size exclusion as depicted in **Figure 18**.[212] This additional energy term of the removal of a solvation shell results in high capacitance, as the whole process itself needs or releases additional energy during the entering and leaving of ions from/to micropores.[211–214] Such effects are not observed on flat surfaces or in larger pores where the capacitance is dominated by the formation of compression double-layers. The second aspect is dominated by the presence or absence of mesopores (2-50 nm-sized pores) which provide facile transportation pathways for ions in the electrolyte. The improved diffusion rate of electrolyte ions helps them to rapidly approach the inner surface of porous electrode particles, resulting in increased rate capability of EDLCs at high current densities. At the same time, the mass-related capacity usually decreases as these additional diffusion pathways bring volume that must be filled with electrolyte but do not contribute to the energy storage capacity as such.[215–217] As electrolyte ions

have to access the interface rapidly at a high rate, additional capacitance derived from micropores only remains available at high current operation if additional mesopores are present.[94,203] Based on these two major aspects, the hierarchical pore design (i.e. a pore structure possessing both micropores and mesopores which are ideally interconnected) of carbon electrodes is recommended for high capacity at high rate. The increased surface area of micropores and efficient diffusion caused by mesopores can show a synergetic effect to achieve high-performing EDLCs.[94] As a result, fabricating a hierarchical pore system of carbon materials has been intensely researched and can be achieved by a templating or etching method.[218]
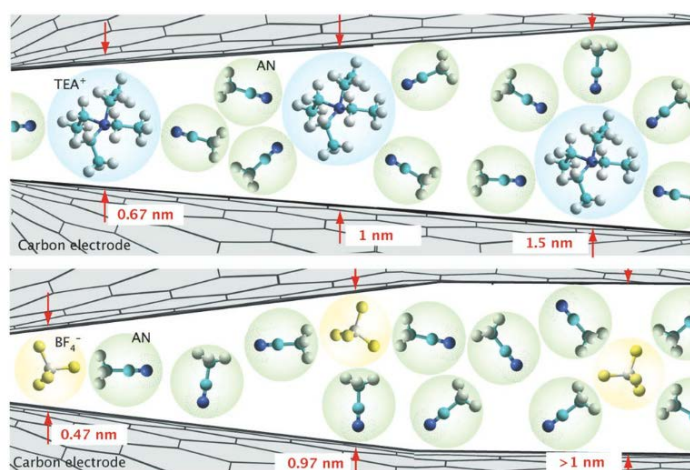
Figure 18. Confinement of ions (TEA$^+$ and BF$_4^-$, TEA$^+$ = tetraethylammonium) solvated by AN (acetonitrile) solvent in micropores of carbon electrode. The ions entered in the pore are bare or only partially solvated. Copyright 2008, John Wiley and Sons.[212]

Besides the use of the hierarchical pore structures, heteroatom doping can also be utilized for carbon-based electrode materials in EDLCs. The surface functionalization with heteroatoms (e.g. nitrogen, oxygen, sulfur) induces surface polarity of the carbon electrode, which is effective to

generate additional capacitance due to enhanced wetting of the electrode surface with electrolyte and the generation of strong binding sites for electrolyte ions.[136] Especially, many efforts have been devoted to developing high-performing nitrogen-rich carbon materials. It was possible to achieve over 300 F g^{-1} within a voltage window of 1.0 V (6.0 M KOH aqueous electrolyte) by combining a pseudo-capacitive effect and improved ion interaction triggered by the highly polarized interface.[219–221] In conclusion, it is a promising pathway to fabricate not only a complex pore structure, but also heteroatom-doped sites in the carbon matrix for the high-performing EDLC electrodes.

1.2.5 Lithium-ion capacitors (LICs)

Despite lots of monumental achievements in LIBs as a worldwide energy storage device, it is insufficient to cover all necessary properties and operation conditions to fulfill the energy storage demand of modern society. On the one hand, more efficient energy storage system in terms of energy density and lifespan at the same time are researched.[158,222–225] In addition, faster charging and discharging rates are demanded for LIBs – ideally without compromising their high energy density. This induced the development of new hybrid devices by combining a high energy density electrode close to LIBs with a high power density and long-term stable electrode close to EDLCs. As the inherited reaction mechanism of LIBs or EDLCs at the electrode is far different, researchers adopted each electrode into one cell with the same electrolyte to utilize the advantage of both LIBs and EDLCs simultaneously. The system consists of the anode from LIBs, the cathode from EDLCs, and a Li-ion-containing salt in a non-aqueous solvent as the

electrolyte.[181,226,227] This combination was determined as one of the successful hybrids, and it is denoted as lithium-ion capacitors (LICs, as described in **Figure 19**).[181,226–229]
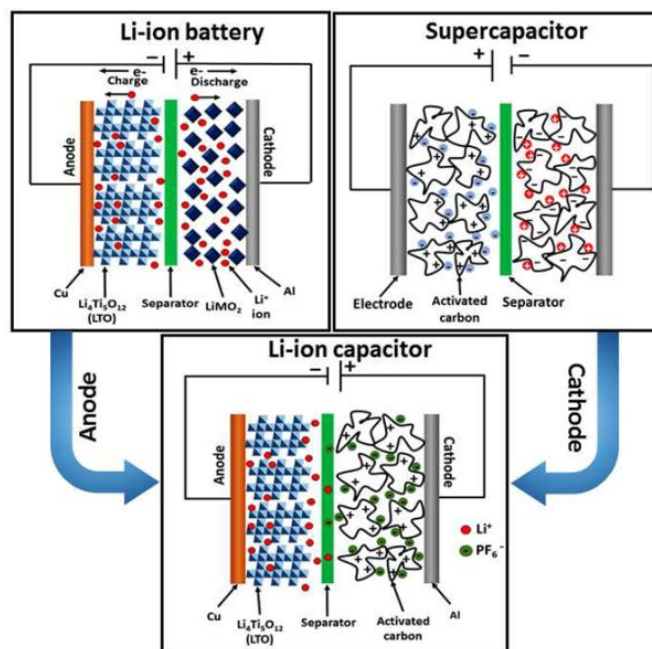
Figure 19. Structure of hybrid LICs with asymmetrical electrodes from LIBs (anode) and EDLCs (cathode). Copyright 2019, Elsevier.[229]

From the mechanistic perspective, charges in LICs are stored asymmetrically by intercalation(or insertion)/removal of Li-ions at the anode while Li-ions at the capacitive cathode are stored in an adsorption-desorption mechanism at the electrode surface. The two different mechanisms at each electrode occur within different potential ranges, which can be helpful to increase the voltage window of operation as well as the energy density.[230,231] In general, the working potential is highly negative at the battery-like anode while it is highly positive at the capacitive-like cathode. From the charging-discharging timescale point of view, LICs provide some advantages in comparison to redox-based systems. In the case of LIBs, the stored specific energy becomes

saturated when the charging time is long and the current is low. However, as shown in **Figure 20(a)**, the amount of stored energy decreases rapidly when higher current is applied due to the inferior diffusion kinetics of Li-ions in a solid-state bulk electrode.[232,233] This energy loss at high current is smaller in LICs because LICs utilize EDLC electrode as a cathode without sluggish intercalation or insertion mechanism. As EDLCs show faster kinetics and a constant rate of energy discharging as shown as black line in **Figure 20(a)**, it enables the hybrid LICs to perform as the most well-suited energy storage device in a certain time range (10 – 600 sec).[234] In summary, as shown in Ragone plot in **Figure 20(b)**, the hybrid LICs thus show an improved power density and lifespan compared to LIBs and an enlarged energy density compared to EDLCs, respectively.
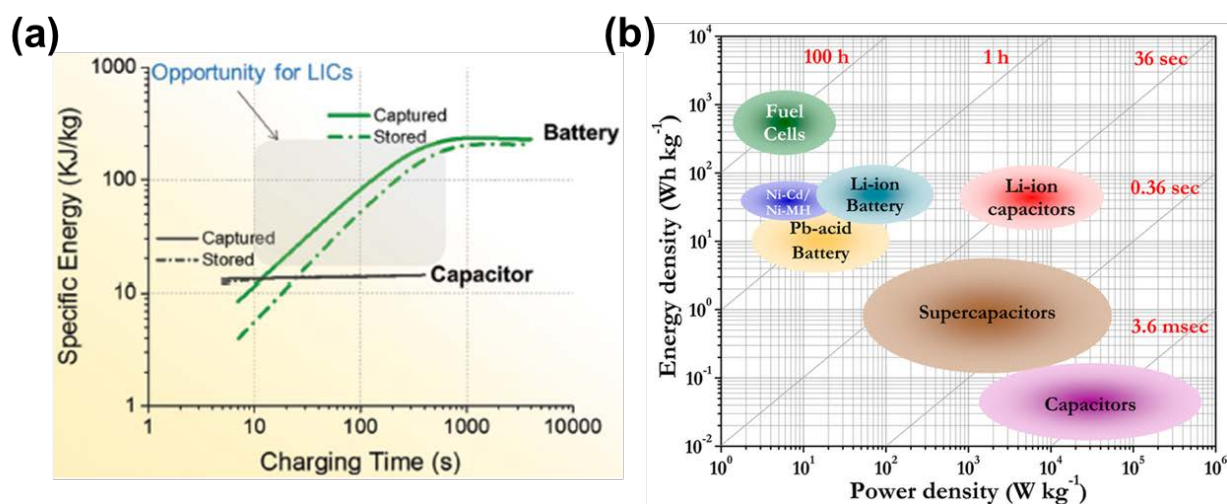
Figure 20. (a) The time-scale region between 10 seconds to 10 minutes is the domain where hybrid LICs can show higher energy and power densities than LIBs or EDLCs alone. Copyright 2017, John Wiley and Sons.[233] (b) Ragone plot of various electrochemical energy storage devices. LICs could achieve their energy density similar to LIBs, while they could also achieve their power density similar to EDLCs at the same time. Copyright 2014, American Chemical Society.[230]

Due to these interesting properties and possibilities, a lot of research has been devoted to LICs since 2001.[228] In one of the pioneering works with an electrode set of activated carbon and nanostructured LTO ($Li_4Ti_5O_{12}$), up to 20 Wh kg^{-1} of energy density was reported, which is about three times larger than that of conventional EDLCs. After this attracting first work, many carbon materials (graphite, activated carbon, CNTs, graphene) were selected as capacitive-cathode due to the high power density and superior stability, while oxide-based electrodes with intercalation type ($Li_2Ti_3O_7$, $LiCrTiO_4$, TiO_2) or insertion type (reduced graphene oxide, Fe_3O_4/F-doped Fe_2O_3, B-doped $Si/SiO_2/C$, Sn/N-rich CNT) were also chosen to achieve the high energy density.[230,233] From the vast amount of researches, the full utilization of the anode capacity under relevant conditions is revealed as a key factor because the kinetics of the faradaic Li-insertion mechanism at the anode is about 10 times more sluggish than the kinetics of capacitive adsorption/desorption at cathode.[235,236] It is worth noting because the total capacity of LICs (C_{Cell}) is influenced not only by the capacity of cathode ($C_{Cathode}$), but also by the capacity of anode (C_{Anode}) (**Eq. 3**).[233] In addition, C_{Cell} is dominated by the electrode which has lower capacity than the other electrode, and thus the mass balancing between two electrodes is generally applied to match capacities of both LIC electrodes.[237] Therefore, the development of an efficient anode with higher loading of lithium capacity and better reversibility is primarily required for high performance of LICs along with the high specific capacity of cathode.

$$\frac{1}{C_{Cell}} = \frac{1}{C_{Anode}} + \frac{1}{C_{Cathode}} \quad \textbf{(Eq. 3)}$$

As LICs are the trade-off device between LIBs and EDLCs, they are considered as an energy storage system to meet the energy and power demand at the same time in various applications

such as electric vehicles but also in micro-scale devices. Furthermore, LICs show high reliability during the continuous cycling, large durability at a temperature from -20 to 70°C, and a low rate of self-discharging voltage drop of usually less than 5% at 25°C.[236,238,239] As LICs have asymmetrical cell structures, Li-ions during the charging-discharging process shuttle between anode and cathode while the counter-ions (e.g. PF$_6^-$ or TFSI$^-$) act differently in the cell. At the cathode interface, these counter-ions in electrolytes are adsorbed into the carbon pores during the charging step.[236] Likewise, Li-ions are intercalated or inserted into the anode. This process consumes not only Li-ions but counter anions in electrolytes and LICs therefore act as a "dual-ion device", which is one reason for their exceptionally faster kinetics than that of LIBs.[240]

However, there are drawbacks to overcome in LICs as well. One of the major challenges is the kinetic imbalance between the battery-like anode and the capacity-like cathode.[241] To make the breakthrough, a possible solution is generating well-distributed nanostructure within the electrode materials which still provide high specific capacity and high rate capability but at the same time ensure improved mass transportation rate. For the development of improved electrode materials, the following criteria are essential because the energy density stored in LICs is calculated as below:[242]

$$\text{Energy density} = \frac{1}{2} \left(V_{max} + V_{min} \right) i\, \Delta t \quad (\textbf{Eq. 4})$$

V_{max} = Maximum operation voltage, V_{min} = Minimum operation voltage

i = Applied current density, Δt = Discharge duration time, assuming a linear discharge slope

The first condition for an electrode with high energy storage capacity is lowering the operation voltage during the lithiation of the anode at the charging step. This helps to achieve the high

V_{max}, and therefore high energy density as well. As a result, metal oxide anode materials are not recommended because the intercalation potential of oxides is comparably high in the range of 1.5 V vs. Li/Li$^+$, leading to a low voltage window and low energy density.[243,244] The second condition is enhanced rate capability at high current density (i). As a kinetic imbalance between the two electrodes in LICs is mostly triggered by the sluggish kinetics at the anode during the high current operation, a highly electro-conductive anode with a well-designed nanostructure a large specific area is required.[233] The third condition is the high specific capacity of the electrode. It elongates the discharge duration time (Δt) so that it results in high energy density. However, most of the previous inorganic materials such as LTO and TiO$_2$ show low capacity values.[245] Finally, the long-term chemical/electrochemical stability of electrode materials is also essential to improve the lifespan of LICs.

Based on the criteria as summarized above, carbon-based electrode materials with hierarchical pore structure could be powerful candidates when applied as anodes in LICs. Compared to many of the oxide-based materials, "porous carbon" electrodes show low Li-insertion potential, large surface area, high specific capacity, and improved kinetics during the charging-discharging process. Additionally, carbon materials often show both high electrical conductivity and chemical/electrochemical stability. Consequently, a well-fabricated porous carbon anode can maximize both energy density (**Eq. 4**) and the lifespan of LICs by applying adequate nanostructure design and modification of the conventional carbon-based anodes.

1.2.6 All-carbon composites and their applications

All-carbon composite materials are highly promising candidates to make a breakthrough of limitations in conventional energy storage devices as they can combine the advantages of individual compounds into one and the same material. For instance, significant breakthroughs have been reported in many electrochemical applications recently.[246] In most cases, the nanohybrid composites consist of an electrically conductive carbon part and a second carbonaceous material with a specific chemical functionality. However, if the composite is prepared by simple physical mixing, it will possibly face the trade-off between electrical conductivity and chemical functionality (i.e. the higher conductivity, the weaker chemical interaction with Li^+ while the higher functionality, the decreased conductivity vice versa, **Figure 21(a)**) even though a homogeneous microscale mixture might be present.[246–249] This trade-off is mainly caused by weak interface contact and overall limited contact area, which leads for instance to increased interface resistance and poor distribution of an externally applied electric field. The improved properties of all-carbon composites are only achievable when the individual components are homogeneously connected on the nanoscale as depicted in **Figure 21(b)** (often denoted as "nanoscale hybrid composite materials"). In such a mixture, electrical conductivity and a certain chemical function that is supposed to fulfill an electrochemical process can be efficiently combined.[250–253]

Several concepts of how to fabricate tailored all-carbon composites have been suggested by previous works already. However, most of the suggestions mainly focused on the CNTs or graphene-based carbon composites. They elucidate the understanding of simple chemical functionalization, but only on the well-defined surface structure.[254–256] Comparably, the porous

carbon domain is not verified in detail yet, but it can be advantageous in terms of strong interaction at the interface and confinement effects that can be utilized in porous systems. The improved interaction between host carbon matrix and guest active materials translates applied electric potential evenly in both materials 3-dimensionally. It can also improve the physical binding to fabricate a more stable and strong composite with better fixation of each phase by less gradient effect which ensures continuous connectivity between hybrid components at high loading. Simultaneously, the confinement effect influences the chemical activity of guest functional materials.[257]
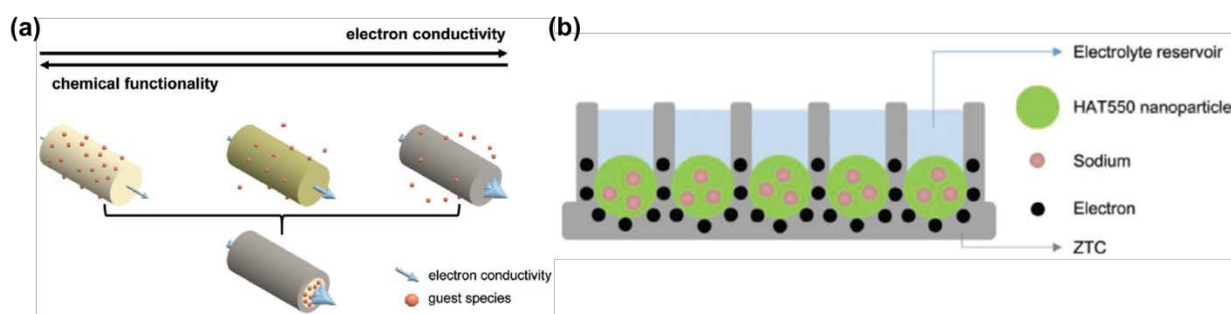
Figure 21. (a) Solution of the trade-off dilemma between electrical conductivity and chemical functionality by all-carbon composites. Image is redrawn from reference. Copyright 2021, John Wiley and Sons.[246] (b) Schematic for explaining the advanced electrochemical properties of HAT/ZTC hybrid composites for sodium ion capacitors. Copyright 2020, Elsevier.[253]

To design the proper all-carbon composites, many considerations should be taken starting with the selection of individual components for the intended application. It is significant to select the appropriate chemical functionality which is identified as possible species to participate in the electrochemical reaction for the optimum performance. Based on that, a set of guest and supporting host carbon is finally determined along with the ratio, geometry, and interface

manipulation. The first main consideration is the question of whether the chemical functionality of active materials in hybrid fulfills the required chemical activity for the targeted reaction process or not.[252,258] Although there is sufficient functionality for the targeted reaction, as the active component often has insufficient electrical conductivity, the hybridization with conductive carbon domain is necessary to design electrochemically functional all-carbon composites. The second main consideration is the question of pore architecture and surface morphology design of the hosting conductive carbon. Providing pores for filling of highly functional materials is crucial, however, the generation of mass transportation channels is also important. Before the loading of the active materials ("the guest"), both the specific surface area and pore volume should be enough to enable the guest to be loaded in the pore. On the other hand, after the loading, there should be residual spaces in the porous carbon to provide free channels for mass transportation of ions or electrolyte molecules. Nevertheless, having larger pores in the host carbon is not always advantageous, even though they can hold a higher loading ratio of the guest and larger empty pores will remain after the loading. As the guest materials themselves should have a small dimension for the facile access at the surface to reduce the gradient of electric potential, smaller pores of the host carbon are sufficient in many cases. The geometry of the pore (e.g. completely open pore vs. vase-type pore with small entrance) has also a significant effect on the performance of hybrid materials.[259,260] When the small entrance jails the active materials inside the pore, it increases stability compared to the surface and can also change their functionality due to the confinement effect. Among lots of considerations for the pore architecture, a hierarchically porous carbon thus can be an attractive pore structure that possesses various pore dimensions and shapes at the same time. Mesopores in this type of host carbon provide larger pores to ensure

efficient mass transportation channels and remain open after the loading of the functional component. On the contrary, micropores can be effectively filled with the guest by the strong binding and sufficient contact area.[261] Of course, all mentioned considerations should be adjusted to the target application properly.

The preparation of hybrid all-carbon composites can be carried out by various strategies. Infiltration of functional materials (or the precursor) into the porous carbon is one of the well-known methods, along with gas-phase deposition (e.g. chemical vapor deposition).[253,262,263] One-pot synthesis is also one of the possible fabrication options, which is a one-step process in which the conductive porous carbon and functional active carbon are synthesized at once such as the method in **Figure 22(a)**.[264,265] Even though it is a single-step process, the non-reacted precursors and decomposed byproducts possibly intervene in the synthesis, possibly leading to a low degree of homogeneity for the hybrid. Recently, numerous cutting-edge techniques (such as laser-induced carbonization described in **Figure 22(b)** and emulsion-templated polymerization) are applied to overcome the drawbacks of the previous composite fabrication methods.[266,267] Nevertheless, no matter what the preparation method is, all these different ways have been attempted to the same final goal: the synthesis of homogenous all-carbon hybrids on the nanoscale. If it makes an inferior distribution of agglomerates or proceeds to the phase separation, the property of the hybrid will be rather similar to physical mixtures of each component without any synergetic effect. In this sense, the generation of surface polarity or functional groups is crucial in certain all-carbon hybrids because it minimizes surface energy at the interface of components to make them a miscible composite.
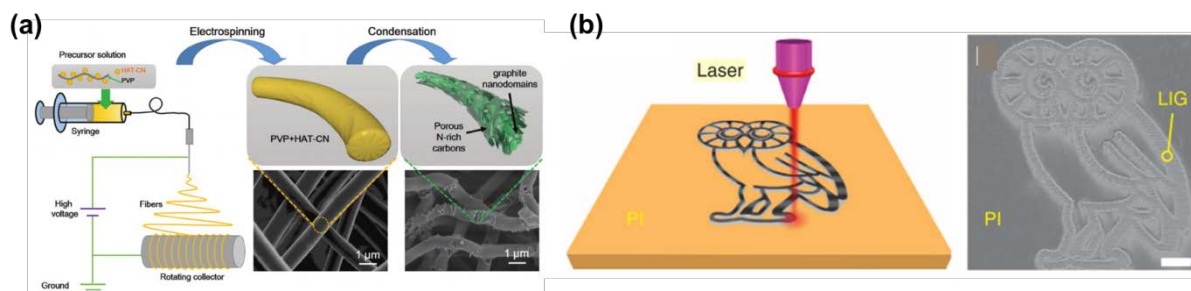
Figure 22. (a) One-pot synthesis of nanohybrid carbon composite fibers by electrospinning the polyvinylpyrrolidone/HAT solution. Copyright 2019, John Wiley and Sons.[265] (b) Laser-induced graphene (LIG) formation from polyimide (PI) polymer for LIG/PI composite materials. Copyright 2014, Springer Nature.[267]

The interface formed between the two components it is crucial to tailor the properties and the stability of the hybrid. From a chemical perspective, the interaction at the interface originates either from intermolecular forces (e.g. van der Waals forces, hydrogen bonding, and $\pi - \pi$ interaction) or chemical bonding (e.g. ionic, covalent) depending on the chemical structure and molecular characters of both components.[268] Unlike other composites, all-carbon composites mainly consist of carbon in both the conductive porous host and the highly functionalized guest. Because of this chemical similarity, all-carbon hybrids may allow for more homogeneous hybridization and stability than other hetero-type composites. Although the individual properties of each carbon-based species are influenced during the composite formation, the properties of the whole carbon composite are different from the pristine materials before the hybridization. It is complicated to design the adequate all-carbon hybrids based on all considerations required as mentioned above. However, all-carbon composites thus have enormous potential for tuning and variation of achievable properties. In addition, countless synthetic pathways can be applied to

optimize the composite due to the independent and tunable properties of individual carbon components.

The resulting benefits of all-carbon composites opened the horizon to various applications, especially in electrochemical energy storage. As carbon-based composite materials have been widely used in this field for many years, all-carbon hybrids are proven as advanced materials with superior properties compared to a single compound or physical mixtures. However, the correlation between the pore structures of all-carbon composites and the electrochemical properties are not explained a lot in the energy storage field yet. Unlike carbon materials with finite structure (such as 1-dimensional CNTs and 2-dimensional graphene), the hierarchically structured carbon-based hybrids possibly induce additional performance improvement by confinement effects and increased surface interaction.

For the application as EDLC electrodes, porous carbon composites are beneficial in terms of conditions as mentioned in **Chapter 1.2.4**. High electrical conductivity and surface area of the composite lead to reduced iR drop of EDLCs during the operation and high capacity by absorbing more ions stably on the surface, respectively.[189,269] As mass transportation is often a rate-determining step in the mechanism of charge storage in EDLCs, a single component or simple mixing approach is in many cases insufficient to achieve the fully utilizable capacitance of the electrode, especially at high current densities. From this perspective, the hierarchical pore structure providing high ion mobility within the electrodes is suitable to overcome this limitation. Along with the pore architecture, the functional carbon in the composite also plays a significant role because it acts as a ligand to hold ions stably at the pore wall thus ensuring strong adsorption and high capacity. Nitrogen-rich active carbon materials are one of the suitable candidates in this

sense as shown in **Figure 23**.[264] The highly polarized surface of N-rich carbon enhances the adsorption energy of electrolyte ions, and especially the graphitic nitrogen in the carbon lattice increases the electrical conductivity of the composite. For the application as LIBs electrode, porous all-carbon composites with heteroatom doping are highly promising even though the redox-based mechanism of LIBs is different with EDLCs which are based on purely physical electrochemical energy storage. This composite can be utilized as an anode where the reduction reaction of Li-ions reversibly occurs during the charging of the battery. As the porous structure with high surface polarity easily attracts Li-ions with stable adsorption, the storage capacity and stability of lithium at the electrode can be improved even at the high current operation.[270]
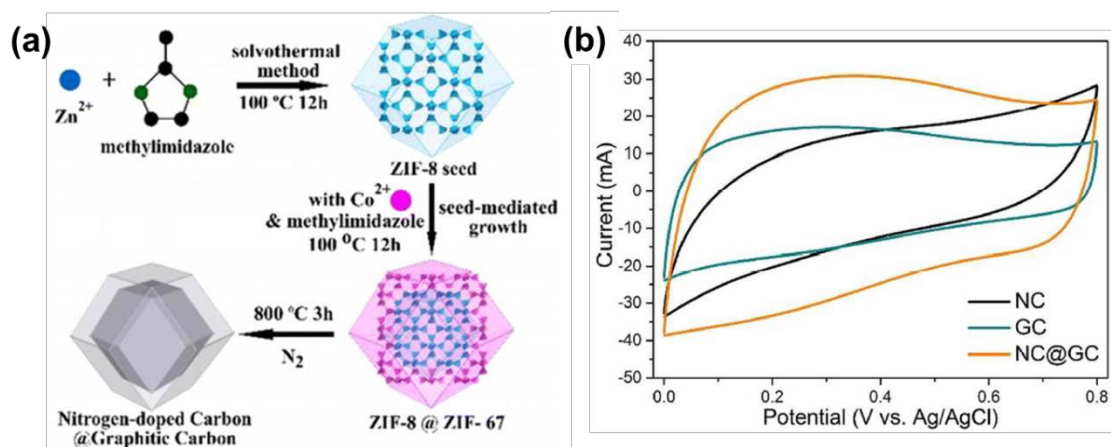
Figure 23. (a) The core-shell designed all-carbon composite materials synthesized from the subsequent carbonization of ZIF-8 (zeolite imidazole framework) core along with ZIF-67 shell. (b) This hybrid shows improved capacity value in cyclic voltammograms compared to NC (core carbon derived from ZIF-8) or GC (shell carbon derived from ZIF-67) alone. Images are redrawn from reference. Copyright 2015, American Chemical Society.[264]

In summary, taking after the success of previous researches with various all-carbon composites within the past years, increased utilization of such composites within the coming period can be

expected. The continuous advancement of porous carbon materials with heteroatom doping will lead to improved possibilities for conceivable combinations and selections. Additionally, materials chemists will face new requests as the challenges in the energy storage research field grow, which naturally stimulates the development of new composite materials. In addition, it is still significant to profoundly investigate the structure-property correlations and optimizations from many different perspectives including material/energy demand (or cost) for the synthesis, electrochemical performance, and yield of the process.

.

2. Research scope

As mentioned above, it is a promising strategy for the fabrication of high-performing electrode to perform the nanoscale hybridization of different carbon-based materials in order to combine their individual advantages, which is sometimes impossible to achieve by one single compound.[271–273] Unlike simple physical mixing on the bulk-scale during electrode preparation, the reason why nanoscale composite formation is essential is that most of the electrochemical energy storage reactions are relying on electron and ion transportation occurring at the same rate and an intimate contact of both parts is therefore crucial.[272,274,275] All-carbon composites with a well-defined structure and composition are needed in order to illuminate structure-property relationships and by that designing proper hybrid nanomaterials for fabricating novel electrode materials for a specific application in a targeted way.

In general, it is complicated to characterize each compound in hybrid materials and their interface. As the correlation between the structure and property can only be clearly verified when in-situ analytical analysis during operation is possible, the realistic solution is to synthesize proper model composites which can be described in structure as defined as possible. Therefore, the appropriate candidate for the carbon matrix should possess well-defined particle size and narrow distribution of pore size, while homogeneously distributed lithiophilic active materials should have well-defined chemical structure and functional groups introduced by a controlled condensation mechanism. It could be a bit apart from the practical use of composite materials, however, this proper modeling makes it easier to characterize the hybrid materials well and thus

provide insights to understand the relationship between structure and property of composites in depth.

As a result, three criteria are set in this thesis to design the model close to the practical hybrid material as depicted in **Figure 24**: (1) Chemical engineering of nitrogen containing lithiophilic active materials, (2) introduction of a well-defined hierarchical pore structure, and (3) use of a carbon matrix with high electrical conductivity. The nitrogen-rich domains present in the composite materials are crucial because they act as active sites interacting with Li-ions by chemical coordination and lead to enhanced electrode wetting with electrolyte. Therefore, hybrid nanomaterials containing nitrogen with electron lone pairs may easily capture Li-ions at an interface, inducing strong bonding which is ideally still reversible under the applied electrochemical reactions. Since the carbons surrounding nitrogen-doped sites are also highly polarized due to the electronegativity of nitrogen, increased surface polarity thereby facilitates interaction with all components within the electrolyte. The hierarchical pore system is also one of the key criteria to fabricate the ideal composite materials. This is because the well-defined pore structure not only improves mass transportation of Li-ions but also provides sufficient space for the infiltration of N-rich precursor molecules as well as a large surface area for lithium ions to be stored. Lastly, the conductive carbon-based framework is also important. Carbon has high electrochemical/chemical stability and high electrical conductivity, which helps to synthesize electrode materials for a long-term application.
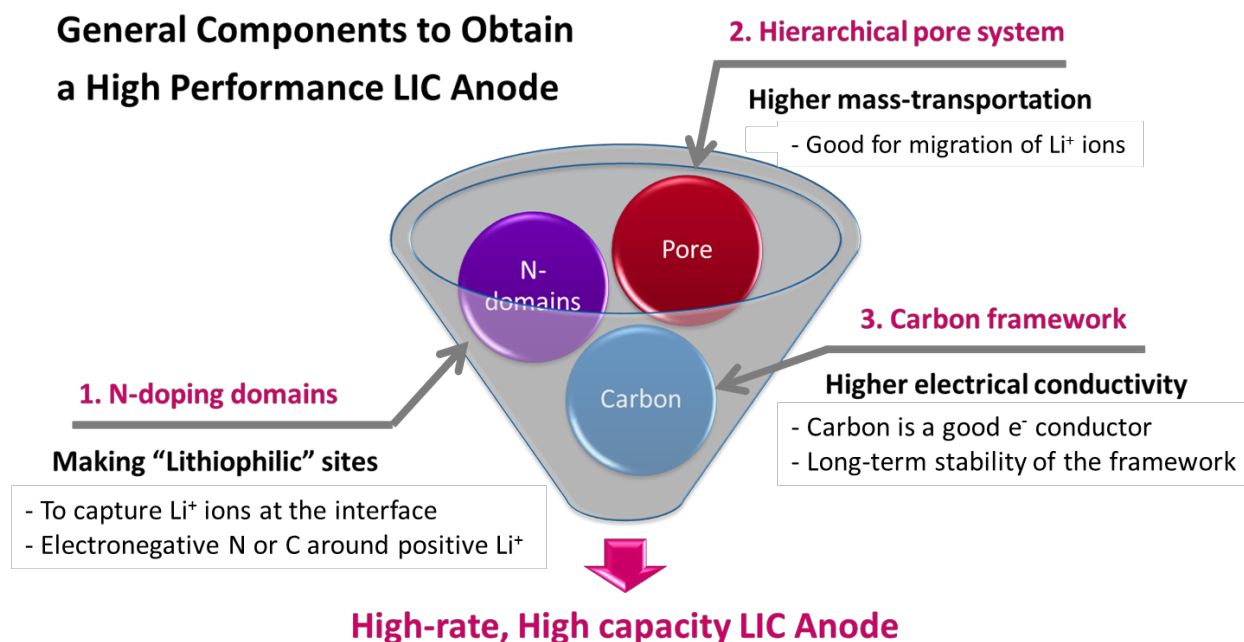
Figure 24. Three criteria for all-carbon composite hybrids to obtain high performing LIC anodes.

Based on the three criteria mentioned above, the subsequent chapter attempts to evaluate this by synthesizing and analyzing certain composite model materials by structure and electrochemical properties. In **Chapter 3**, a meso/microporous carbon zinc oxide-templated carbon (ZTC) particulate material will be synthesized and then an organic precursor HAT-CN (hexaazatriphenylene-hexacarbonitrile) which has a high content of nitrogen will be filled into the pores of ZTC after the condensation. This 0-dimensional all-carbon composite will be firstly analyzed in view of the question how the pore structure in the hybrid can be controlled. By facile change of synthetic parameters and ratios of each component, it will be shown that tunable pore structure of the composite is easily achievable. In addition, the HAT/ZTC hybrid will be examined on how the pore structure is connected to Li-ion storage properties as LIC electrode. In

this regard, the results will allow deeper insights into Li-ion dynamics in different pore systems, and for different HAT:ZTC ratios.

In **Chapter 4**, a commercially available carbon fiber (ACF) will be utilized as a 1-dimensional nanoporous carbon matrix to form various nanocomposites with melamine. Compared to HAT in chapter 3, melamine can be polymerized as nitrogen-rich structure from low cost precursors and in a rather simple synthetic process, resulting in a promising potential for large-scale application. The pore structure of the 1-dimensional fibrous composite is simply modified by the mass ratio of melamine precursor and ACF. Since ACF has ultra-micropores, it will be analyzed by gas physisorption techniques with various absorbates at different temperatures. Based on the analyzed physisorption data, the numerical structure-property relationships will be calculated out not only from total pore volume but more specifically from ultra-micropore volume. Consequently, it will be possible to point out which structural analysis is the most suitable to examine the ultra-micropores, and how these pores affect the LIC performance.

All fabricated electrode materials selected in **Chapters 3 and 4** are all-carbon composites that fulfill the three basic criteria (i.e. they are hierarchical porous carbon materials with high surface polarity) as suggested above. From analyzing the following results it will be possible to get a better understanding on how hybrid all-carbon composites interact with lithium ions on the nanoscale as well as how structural properties affect the energy storage performance. Based on this understanding derived from the applied model materials, it will become possible to provide rational design strategies towards practical hybrid materials for efficient electrodes in LICs.

3. 0-Dimensional HAT/ZTC all-carbon composite materials for lithium storage[*]

3.1 Background and current research

As discussed in **Chapter 1.2.3 and 1.2.4**, both LIBs and EDLCs are major energy storage, however, LIBs have high energy density (250-280 Wh kg^{-1}) with low power density (1 kW kg^{-1}) while EDLCs have low energy density (~10 Wh kg^{-1}) with high power density (10 kW kg^{-1}), respectively.[158,181,226,233,276] To overcome this trade-off, the development of hybrid LICs with fast charging speed, large capacity, and long lifespan is a worldwide goal for the near future as explained in **Chapter 1.2.5**.[276–279] The nanoscale all-carbon composite hybrids in **Chapter 1.2.6** may overcome this dilemma.[253,280] To achieve the all-carbon composites with heteroatom-rich porous structure in small dimensionality as suggested in **Chapter 2**, ZTC is one of the excellent candidates due to its well-developed hierarchical pore structure and conductive carbon matrix. The utilization of ZTC has been applied recently for sodium ion capacitor anodes and it has been shown that ZTC with uniform mesopores and nitrogen-rich carbon synthesized within ZTC as host by condensation of HAT-CN[153,281] can significantly improve the energy storage capacity and rate capability of the sodium ion capacitor anode in comparison to the individual compounds or their physical mixture.[253] The low electrical conductivity of HAT-derived carbon is compensated by the high conductivity of hosting ZTC matrix and thus electron transport and

metal storage can be combined in such a composite material. Even though this proof-of-principle has been successful, structural characteristics of the materials and their influence on the electrochemical characteristics are poorly understood and remain to be optimized. For instance, the loading of nitrogen-rich carbon should be chosen as high as possible to increase the number of ion adsorption sites without decreasing the electrical conductivity of the overall composite too much. It also remains an open question if comparable effects and conclusions as observed for sodium storage with such composites hold also true for the storage of smaller lithium cations as in LICs.[282,283]

To address these questions, a series of all-carbon composite materials with different HAT-CN loading has been synthesized at different temperatures. A fast and a slow drying procedure have been applied to investigate the influence of the homogeneity of the composites. The differences in textural and chemical properties between the samples have been investigated and are linked to the properties of the materials when applied as anode materials for LICs. It becomes evident that all these "regulation screws" have an important influence on the pore structures and chemical properties of the resulting composite materials. This, in turn, has strong influence on their electrochemical properties.

3.2 Hierarchically porous ZTC carbon and N-rich HAT for the composite formation

Figure 25(a) illustrates the procedure to prepare HAT-ZTC composite materials. ZTC was first synthesized through the hard templating method using 20 nm-sized ZnO nanoparticles as porogen and sucrose as carbon precursor following a recently reported procedure.[253] After the heat treatment at 950°C under inert atmosphere and washing with hydrochloric acid solution, ZTC with hierarchical micro- mesopore structure was obtained. In the next step, HAT-CN monomers were dissolved in dimethylformamide (DMF) and infiltrated into ZTC at a HAT-CN:ZTC mass ratio of 2:1, 4:1, 6:1, and 8:1, to produce composites denoted as HAT2, HAT4, HAT6, and HAT8, respectively. The influence of the evaporation rate of DMF was studied by applying different drying procedures after the mixing. Slowly evaporated composites (denoted as "s-HATX") were dried in a drying oven under air at 60°C for 2 days first followed by heating in a vacuum oven. On the contrary, the fast evaporated composites ("f-HATX") were dried directly in the vacuum oven at 60°C overnight. After infiltration of ZTC with HAT-CN, the latter was condensed through additional heat treatment at 550, 700, or 1000°C to form HAT-ZTC composite materials. A physically mixed sample (denoted as "pm-HAT-ZTC") obtained by grinding ZTC and HAT-CN (treated at 1000°C) in a mortar was also synthesized to investigate the impact of composite formation.
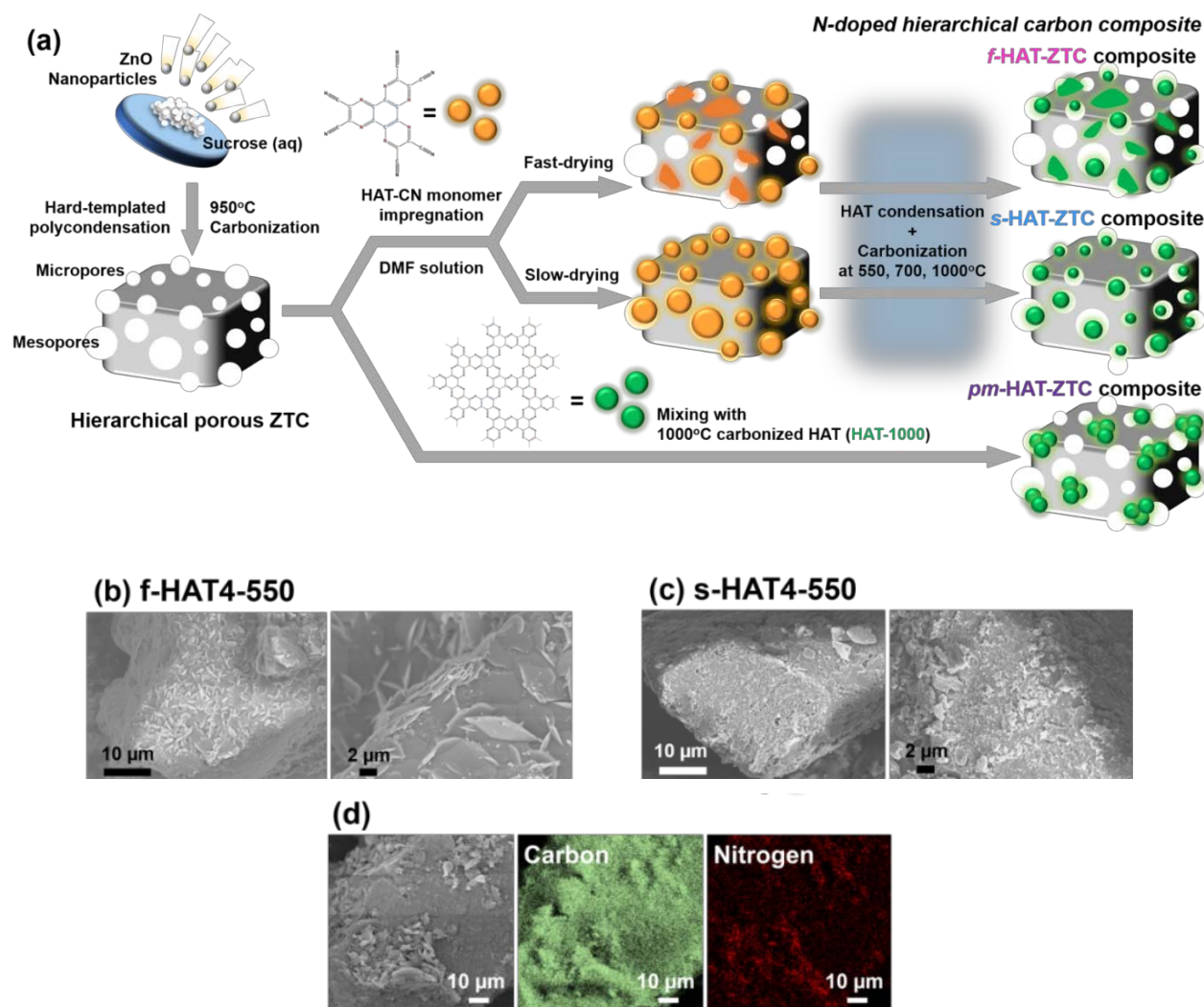
Figure 25. (a) Synthesis of HAT-ZTC composites. Depending on the different method for HAT loading, the composites are denoted as fast-evaporated (f-HAT-ZTC), slow-evaporated (s-HAT-ZTC), and physically-mixed (pm-HAT-ZTC) composite. SEM images of (b) f-HAT4-550 and (c) s-HAT4-550 as well as (d) EDS mapping of carbon and nitrogen distribution in f-HAT4-550.

Elemental analysis (EA) shown in **Table S1** has been exemplarily performed for composites that underwent fast drying after condensation at different temperatures. Pure ZTC, pure HAT-1000, and pm-HAT-ZTC have been measured for comparison. For a given condensation temperature of f-HATX samples, the nitrogen content is higher in all cases after loading with a higher amount of

HAT-CN. In addition, it can be seen that the nitrogen content decreases with increasing condensation temperature, in agreement with previous studies.[253] Condensation of bulk HAT-CN at 700°C or below leads to the formation of a C_2N-like material with a high content of pyrazinic nitrogen.[284–286] In contrast, the material obtained from HAT-CN condensation at 1000°C is a rather ordinary N-doped carbon with a lower overall nitrogen content, mainly bonded in graphitic structure motives. Thermogravimetric analysis (TGA) curves of the ZTC infiltrated with different amounts of HAT under N_2 and synthetic air atmosphere are shown in **Figure S1(a)**. As ZTC is not losing mass upon heating under inert atmosphere, higher loading with HAT is the reason for higher mass loss during heating up to 1000°C. Under air, all HAT-loaded ZTCs expectedly show full mass loss up to ~700°C. From the corresponding DTG curves shown in **Figure S1(b)**, it can be seen that the condensation of HAT-CN starting at a temperature slightly above 500°C is followed by oxidative decomposition and/or depolymerisation of the materials slightly below 700°C. As can be seen in **Figure S1(c) and S1(d)**, the physical mixture, HAT-1000 and the f/s-HAT4-550 composites expectedly show complete mass loss upon heating to 600-700°C under synthetic air as well. The physical mixture of polymerized HAT and ZTC as well as HAT-1000 has apparently lower thermal stability in comparison to the composites. The highest temperature necessary for full mass loss is observed in s-HAT4-550. This indicates that there is a difference in structure and resistance against thermal decomposition or oxidation between the two composites.

As shown in scanning electron microscopy (SEM) images in **Figure 25(b) and 25(c)**, f-HAT4-550 has a non-homogeneous HAT-derived carbon distribution with some disk-like particles present on the surface of ZTC. Such morphology is typical for HAT-CN and its condensation

products as shown in **Figure S2**. EDS mapping shown in **Figure 25(d)** confirms a relatively low uniformity of HAT-CN deposition on ZTC after fast drying as the amount of nitrogen present on the external surface of ZTC shows clear differences between different areas. In contrast, s-HAT4-550 does not contain apparent HAT-like structures on the external surface of the ZTC. This is indicating that unwanted deposition of HAT-CN outside the internal pores of the ZTC host carbon occurs when the solvent is evaporated fast. Slow drying seems to be crucial to obtain a uniform composite with the HAT-CN uniformly embedded inside ZTC pores.

3.3 Structural characterization of HAT/ZTC composites

N_2 physisorption analyses shown in **Figure 26(a)** and summarized in **Table S2** result in a type IV(a) isotherm for pristine ZTC with a high nitrogen uptake below a relative pressure of $p/p_0 = 0.1$ with a constant slope from 0.1-0.7, and a hysteresis loop in the range from $p/p_0 = 0.7$-1.0. This indicates that a large volume of micropores is combined with mesopores in this material leading to a high specific surface area of 1520 m^2 g^{-1} and a total pore volume of 2.55 cm^3 g^{-1}. All mesopores seem to be well accessible as no sign of cavitation can be seen in the isotherm. In contrast, HAT-1000 shows a type I isotherm which proves its predominantly microporous structure.[79] The isotherm of pm-HAT-ZTC sample lies between that of HAT and ZTC but with low mesopore content resulting from the HAT-1000:ZTC mass ratio of 6:1. As can be seen in the inset of **Figure 26(a)**, the shape of the hysteresis loop of ZTC is fully maintained, revealing that physical mixing of HAT does not affect the pore system of ZTC. Unlike the physical mixture, however, f-HAT and s-HAT composites (data is exemplarily shown for s-HAT4-550 and f-HAT4-550 in **Figure 26(a)**) show changed hysteresis loops with signs of cavitation and reduced total pore volume in comparison to the physical mixture. This is a clear sign that the pore structure of ZTC is altered and filled with HAT condensation products. s-HAT4-550 shows a lower total nitrogen uptake and a more significant change of the hysteresis loop in comparison to f-HAT4-550. This confirms that a larger portion of the ZTC mesopores is filled with HAT-derived carbon after slow drying.
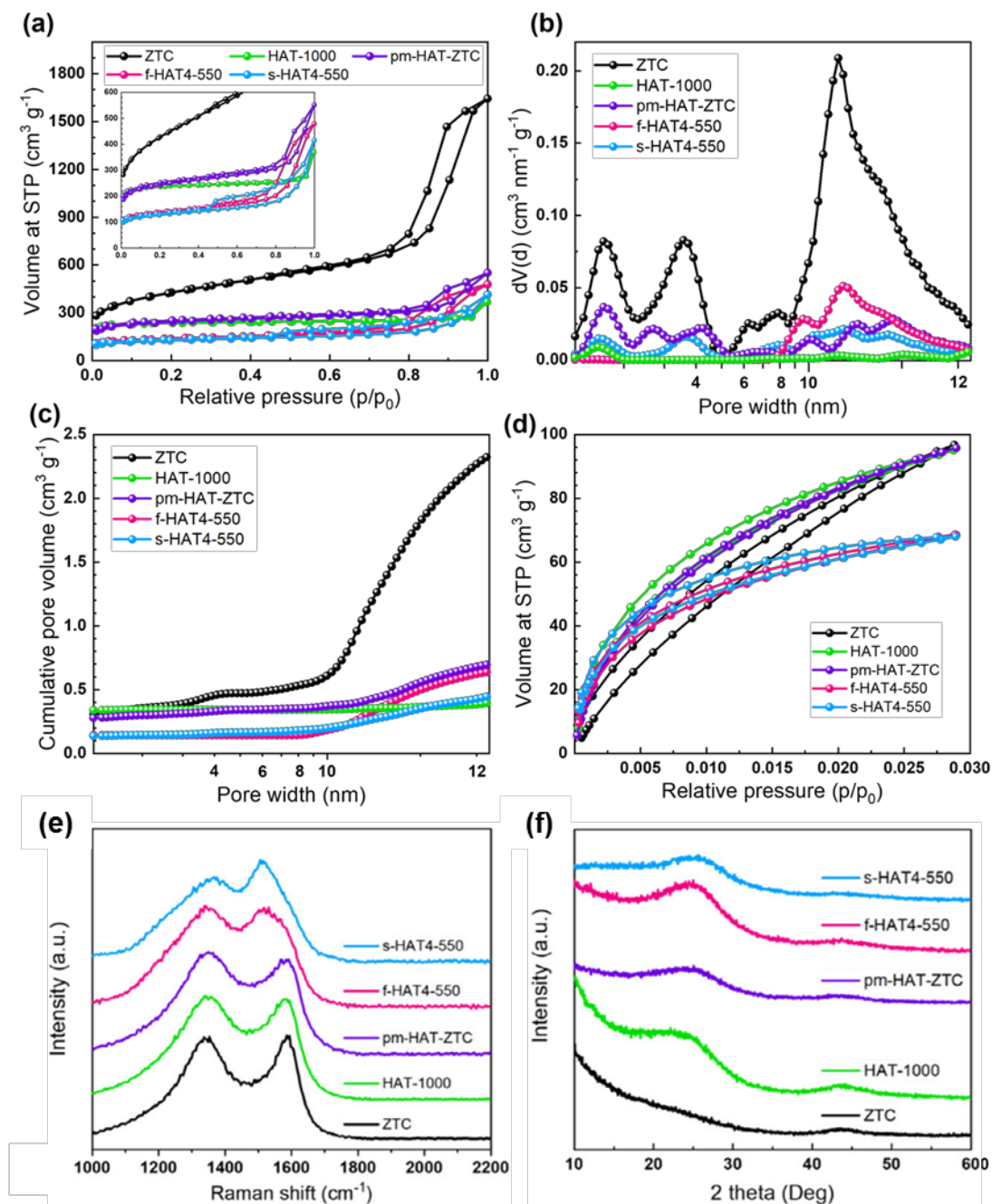
Figure 26. (a) N_2 physisorption isotherms (77 K) and corresponding (b) differential and (c) cumulative pore size distributions as well as (d) CO_2 physisorption isotherms. Materials characterization of ZTC, HAT-1000, pm-HAT-ZTC, f-HAT4-550, and s-HAT4-550 by (e) Raman spectra, and (f) powder XRD diffraction patterns.

These structural differences between the samples are also becoming visible in the differential and cumulative pore distribution curves shown in **Figure 26(b) and Figure 26(c)**, respectively. In case of pristine ZTC, there is a contribution to the total pore volume coming from micropores below 2 nm as well as from mesopores centred at ~4 nm and 10-12 nm. The physical mixture pm-HAT-ZTC has pores in the same size range. A minor but notable contribution to the overall pore volume still seems to originate from unfilled ZTC pores with diameters above 10 nm. The pore size distribution of ZTC changes significantly after loading with HAT-CN and its condensation but depends on the applied drying process. In both composites, the micropore volume decreased in comparison to unfilled ZTC. A larger volume of large pores is still present after fast drying. This is again confirming a more homogeneous infiltration of the ZTC pore system with HAT-CN when slow drying is applied. ZTC micropores are apparently all well filled with HAT-CN but slow solvent removal seems to be crucial for deposition of the precursor molecules for nitrogen-rich carbon inside the larger pores of ZTC instead of deposition on the external surface of the particles. Nitrogen physisorption data of the entire series of prepared composites as well as the condensation products of pure HAT-CN at different temperatures and the corresponding pore size distributions are shown in **Figures S3-S10** and summarized in **Figure S11 and Table S2**. The fact that higher condensation temperature of bulk HAT causes an increase in SSA and pore volume is known from previous studies[153,281] and also becoming obvious in all composite materials independent of the drying method and loading of HAT-CN. This in combination with the lower condensation yield at higher temperature (i.e., the higher mass loss of the sample) is responsible for the observed increase of the mass-specific porosity of the composites with a given loading and drying procedure. As another general trend, it appears

that the SSA and pore volume of all composites decrease at higher HAT-CN loading at all temperatures applied and for both drying methods. This is reasonable as the condensation products of HAT-CN have less SSA and the pore volume than ZTC, so the corresponding values of the composites decrease at higher content of N-doped carbon. Finally, for all loadings and condensation temperatures, the slow drying method results in composite materials with lower total pore volumes in comparison to the fast drying method. This confirms that a more homogenous pore filling can be achieved with slow drying over a wide range of HAT/ZTC ratios.

CO_2 physisorption isotherms have been measured at 273 K for selected samples as well and are shown in **Figure 26(d) and Figures S4, S5, S6, and S10**. All nitrogen-doped carbon-containing samples show strong interaction with CO_2 as shown by the high uptake at low relative pressures in the range $p/p_0 = 0 - 0.005$. The total CO_2 uptakes at $p/p_0 = 0.03$ is in line with the micropore volumes detected by nitrogen physisorption measurements. Micropores of ZTC seem to be blocked after loading with HAT-CN and condensation. In all cases, the isotherms are becoming a rather linear shape for materials with lower nitrogen content, that is, with lower HAT-CN loading or with higher condensation temperature. This is caused by the fact that the surface of nitrogen-doped carbons has a stronger interaction with polarizable CO_2 molecules which can be expected to act as "lithiophilic sites" as well.

Raman spectra are shown in **Figure 26(e) and Figure S12**. All spectra can still be fitted with a 4-band model.[280] It is becoming obvious that the width of the peaks decreases with lower content of HAT-derived carbon and after condensation at higher temperatures. While condensation at 550 or 700°C leads to remarkably nitrogen-rich materials with a high content of pyrazinic nitrogen and minor contribution of 6-membered carbon rings (responsible for the D-

band), ZTC and composites containing HAT-derived carbon condensed at 1000°C rather show the Raman characteristics of ordinary defect-rich and porous sp^2-dominated carbon materials with shaper and more intense D-bands but less intense and broadened D_2 and A bands. G-bands are shifting towards larger wavenumbers with higher condensation temperature due to the decreasing contribution of C-N bonds and the increasing dominance of C-C bonds. Such materials are expected to have a lower intrinsic affinity to Li-ions but at the same time a higher electric conductivity.

Powder X-ray diffraction (XRD) patterns have been measured and are shown in **Figure 26(f), Figure S13 and S14**. All materials show XRD curves as typical for highly porous carbon materials without long-range ordering. In some cases, broad reflexes at ~26° and ~47° can be seen which are characteristic for stacking into graphite-like domains. Their intensity is, however, not directly representative for the "graphitization" in such a material as it can be overshadowed by scattering intensity from the pore systems at low angles. This scattering intensity is high for ZTC and generally increasing when HAT is carbonized at higher temperatures, which is in line with the physisorption measurements. In all samples where HAT was carbonized at 1000°C the (002) reflection at 26° only appears as shoulder whereas the (101) reflection at 47° appears relatively sharp. As a clear difference, it can be seen that the XRD patterns of f-HAT samples are rather similar to bulk HAT-derived carbon materials for a given condensation temperature as compared to the corresponding s-HAT material. This is another indication for the structural differences caused by the chosen drying protocol.

3.4 Structure-related electrochemical performance of the composite as LIC anode materials

Regarding to the application in LIC anodes, the resistances of composite and cell are of crucial importance as well. This has been experimentally confirmed by measuring electrochemical impedance spectroscopy (EIS). The Nyquist plots displayed in **Figure 27(a)** elucidate that all composite electrodes have different resistance. Among all samples, s-HAT4-550 has lower intrinsic resistance in comparison to ZTC and other composites.[287,288] This difference may arise from the uniform carbon coating on the surface of ZTC after slow drying. The nonpolar ZTC surface with lower content of heteroatoms does not have high-energy stabilization sites for Li-ions and electrolyte solvent molecules, resulting in the formation of an inferior interface between electrode and electrolyte. On contrary, HAT containing composites ensure high affinity between Li-ions and the electron-donating nitrogen atoms contributing a strong chemical interaction in contrast to rather capacitive Li storage into the pores of ZTC.[289,290] Homogenous distribution of nitrogen-rich carbon in s-HAT4-550 leads to reduced resistance compared to f-HAT4-550, while pm-HAT-ZTC lies between ZTC and HAT-1000.

Full electrochemical characterization of the all-carbon composites and related reference samples has been carried out to conclude on the relationships between their structures and properties as anode materials in LICs. **Figure 27(b)** represents the relationship of the 1st lithiation capacity as shown in **Figure S15** and the irreversible capacity loss (calculated by the gap between the 1st lithiation capacity and the reversible capacity of the second cycle) with the total pore volume and BET surface area. Larger pore volume and SSA clearly induce an increased portion

of irreversible capacity due to the SEI layer formation which seems proportional to the surface area of the electrode that is accessible for the electrolyte. High surface area ZTC shows large capacity decay after the 1st cycle. The changed pore structure and pore filling by composite engineering with N-doped carbon slightly decreases the capacity loss in the composite electrodes. However, even after composite engineering, huge capacity loss occurs as it is typical for highly microporous and defect-rich carbons. This disadvantage could possibly be minimized by the use of artificial SEIs or solvent-free electrolytes.[291,292] Galvanostatic charge-discharge profiles between 0.0 and 3.0 V (vs. Li/Li$^+$) of a half cell test at a current density of 0.1 A g^{-1} are shown in **Figure 27(c)**. Under the conditions of these measurements, all curves represent a rather capacitor-like behaviour shape dominated by sloping capacity without clear plateaus due to the absence of complete and specific electron-transfer processes between electrode and lithium ions. Although ZTC displays the highest capacity at the initial cycling, it degrades rapidly to 381.7 mAh g^{-1} in the 5th cycle. On the other hand, s-HAT4-550 maintains a capacity of 411.2 mAh g^{-1} in the 5th cycle. This is not only significantly higher than the capacity achieved by HAT-1000 and pm-HAT-ZTC but also exceeds f-HAT4-550. Although the nitrogen-content and chemical bonding motives in both samples are comparable, the intimate contact between both phases and more homogeneous structure of s-HAT4-550 apparently has a significant positive impact on the lithium storage. s-HAT4-550 not only prevails over other materials in terms of capacity but also in terms of rate capability as summarized in **Figure 27(d) and Figure S16**. At 0.1, 0.2, 0.5, and 1.0 A g^{-1}, the averaged discharging capacities are calculated as 409.4, 322.8, 247.8, and 180.2 mAh g^{-1}, respectively.
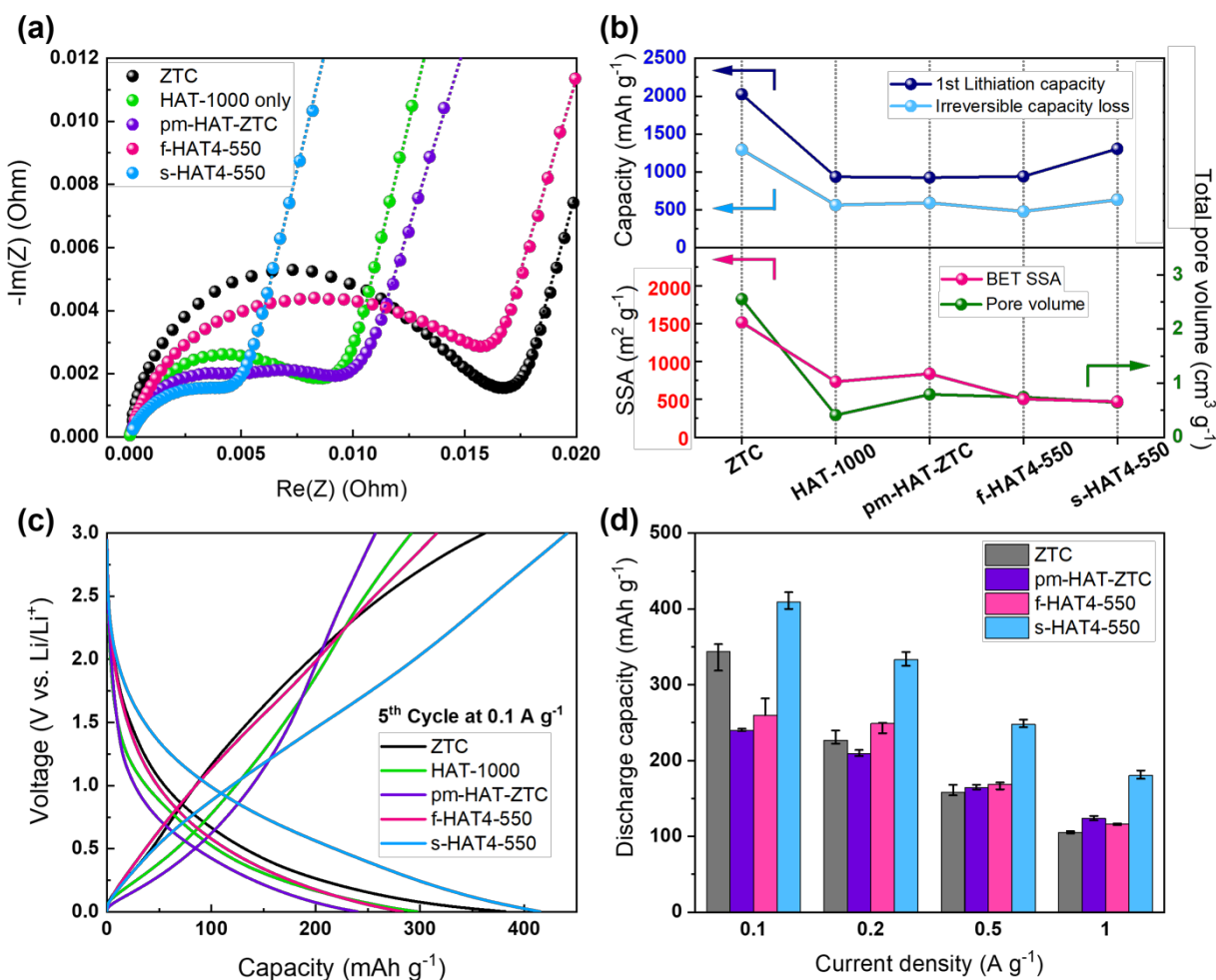
Figure 27. (a) Nyquist plots, (b) correlation between the 1st cycle irreversible capacity of LIC and the pores structures, (c) charge-discharge voltage profiles (5th cycle) at 0.1 A g⁻¹, and (d) comparison of discharge capacity measured at different current rate (averaged by 4 cycles each at 0.1, 0.2, 0.5, 1.0 A g⁻¹) of ZTC, HAT-1000, pm-HAT-ZTC, f-HAT4-550, and s-HAT4-550.

All capacity data for samples obtained at different temperature, ratio, and drying rate are summarized in **Figure S17**. Interestingly, the capacitance does in tendency increase after carbonization at higher temperatures for composites that underwent the fast drying procedure but show different behaviour for the slowly dried materials. This could indicate that a redistribution of HAT-derived N-doped carbon takes place at condensation temperatures higher than 550°C.

The negative effect of inhomogeneous mixing between ZTC and HAT-CN after fast drying can thus be minimized when the condensation is carried out at higher temperature.
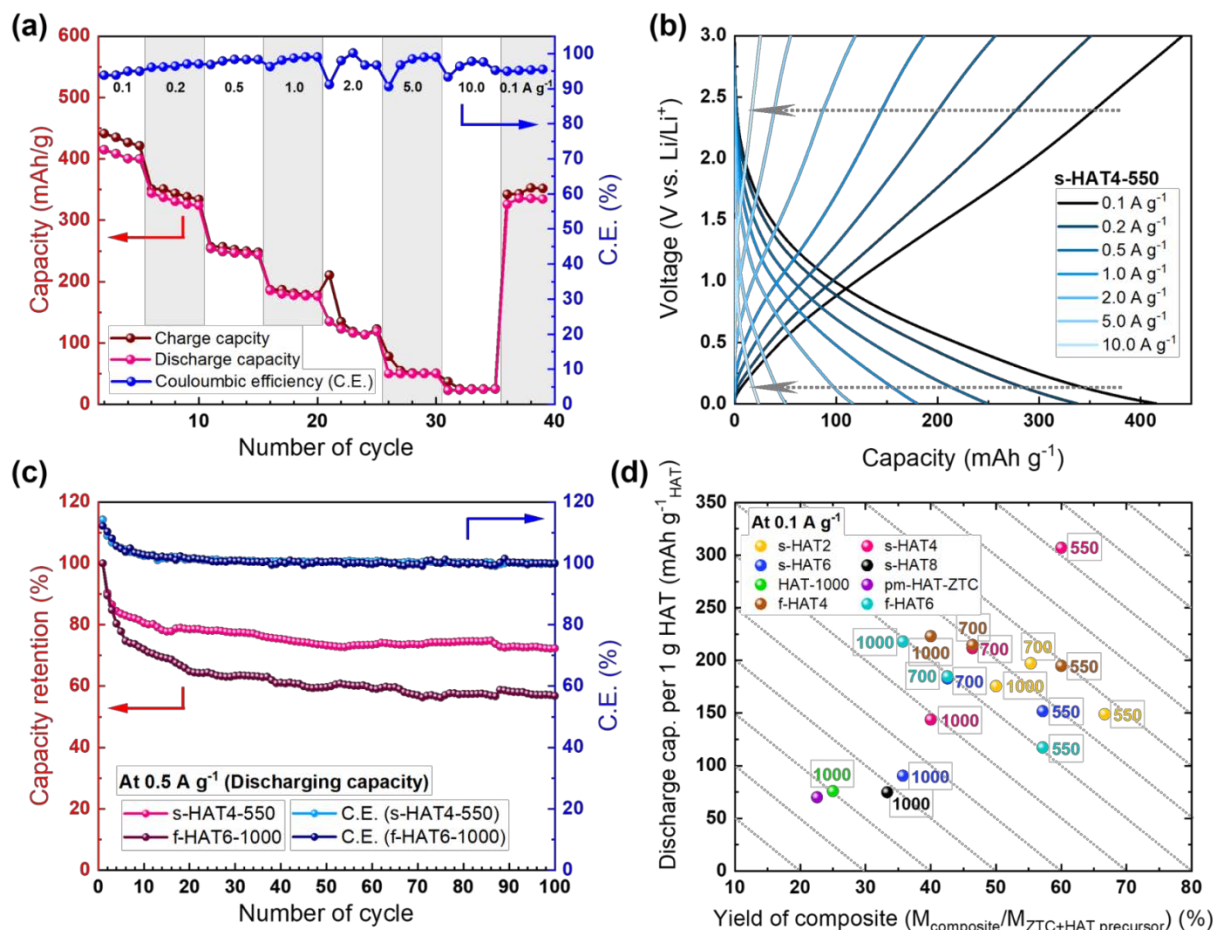
Figure 28. (a) Rate capability test of s-HAT4-550 from 0.1 to 10 A g^{-1}, and (b) galvanostatic charge-discharge profiles of each current rate. (c) Long-term operation result (100 cycles at 0.5 A g^{-1}) of s-HAT4-550 and f-HAT6-1000 with the coulombic efficiency (C.E.) and discharging capacity retention compared to the initial capacity. (d) Specific discharge capacity of composites per unit mass (gram) of HAT-derived N-doped carbon plotted against condensation yield.

The rate capability of s-HAT4-550 was investigated in the range from 0.1 to 10 A g^{-1} as shown in **Figure 28(a) and 28(b)**. At 2, 5, and 10 A g^{-1}, the averaged specific capacities are 122.4, 57.3,

and 27.6 mAh g^{-1}, respectively with corresponding coulombic efficiencies of 97.9, 96.8, and 96.1%. A long-term cycling test shown in **Figure 28(c)** also confirms that s-HAT4-550 has a high reversibility during continuous charging-discharging. Even though the initial capacity of f-HAT6-1000 is higher, it rapidly decayed compared to s-HAT4-550 as shown in **Figure S18**. After 100 cycles of operation at 0.5 A g^{-1}, the capacity retention of f-HAT6-1000 is 57% while that of s-HAT4-550 maintains 72% of its initial capacity. The capacity comparison for f-HAT composites is summarized in **Figure S19**.

Within such an optimization study, it is also practically important to maximize the capacity per used mass of HAT-CN precursor. In **Figure 28(d)**, discharging capacity of all composites measured at 0.1 A g^{-1} divided by the mass of HAT-derived N-doped carbon are plotted versus the condensation yield (including the unchanged mass of ZTC). Among all composites, s-HAT4-550 shows the highest condensation yield and 307.1 mAh g^{-1} of capacity per gram of HAT-derived carbon. For comparison, the yield and capacity per HAT-derived carbon of f-HAT6-1000 is 35.7% and 90.5 mAh g^{-1}, respectively. This is showing the importance of raw material use for the composite design, which is another important aspect that has to be taken into account in addition to simple electrochemical data.

Based on the criteria suggested in **Chapter 2**, it was successful in this chapter to bridge the pore structure of lithiophilic all-carbon composites and the electrochemical properties of LICs. Based on this discovery, it is expected that there could be also a similar relationship between the pore architecture and LIC performance in higher dimensions. Therefore, in the next chapter, the influence of hierarchical pore structure on the electrochemical performance of LICs with 1-dimensional all-carbon composites will be discussed.

4. 1-Dimensional all-carbon composite materials for lithium storage

4.1 Background and current research

In **Chapter 3**, powder-based all-carbon composites (HAT/ZTC) were applied as anode for LICs. It proved that the lithiophilic pore structure of the composite influences the interaction between lithium ions and the anode surface, leading to enhanced lithium storage capability. Both a high density of interaction sites and an enlarged interface area with high porosity are helpful to enhance the capacity of LICs.[230,233] However, it remains a difficult task to achieve uniform lithiophilic sites and the necessary electric conductivity at once by 0-dimensional all-carbon composites. This is because of the random size and shape of carbon powder and the interfacial resistance between each composite carbon particle. Hence, electrode materials combining 1-dimensional carbon substrates to make all-carbon composites are a promising alternative.[265,293] In particular, nitrogen-rich and hierarchically porous fibers are a suitable couple for anode in LIC if they have chemical compatibility facilitating nanoscale mixing. At the same time, they are fulfilling complementary tasks, namely Li-ion storage in N-doped and electron transport through the 1-dimensional carbon matrix. While 1-dimensional composites are getting more and more established and synthetic approaches towards such nanoscale hybrid materials are constantly developed,[253,279,293] systematic studies, as well as understanding of the influences of the ratios of the individual compounds and the porosity of the nano-mixtures are still not abundantly available.

To provide a more profound understanding of the pore structure-electrochemical performance relationships in 1-dimensional system, melamine-derived uniform N-rich carbon has been engineered into nanohybrids with porous carbon fiber matrices in this chapter. Melamine is used as precursor for N-rich carbon(nitride) that is uniformly coated and condensed over the pristine carbon material through deposition from the gas phase in an infrared (IR) oven,[294,295] leading to homogeneous distribution of lithiophilic sites within a conductive framework. A simple change of the ratio of carbon fibers to melamine has been applied to control the chemical composition and pore structure of the hybrids. Electrochemical characterization of the synthesized materials as LIC anodes allows concluding on the influence of micropores or ultra-micropores and of N-rich lithiophilic sites on Li storage capacities and rate capabilities.

4.2 Synthesis of microporous carbon fibers infiltrated by melamine
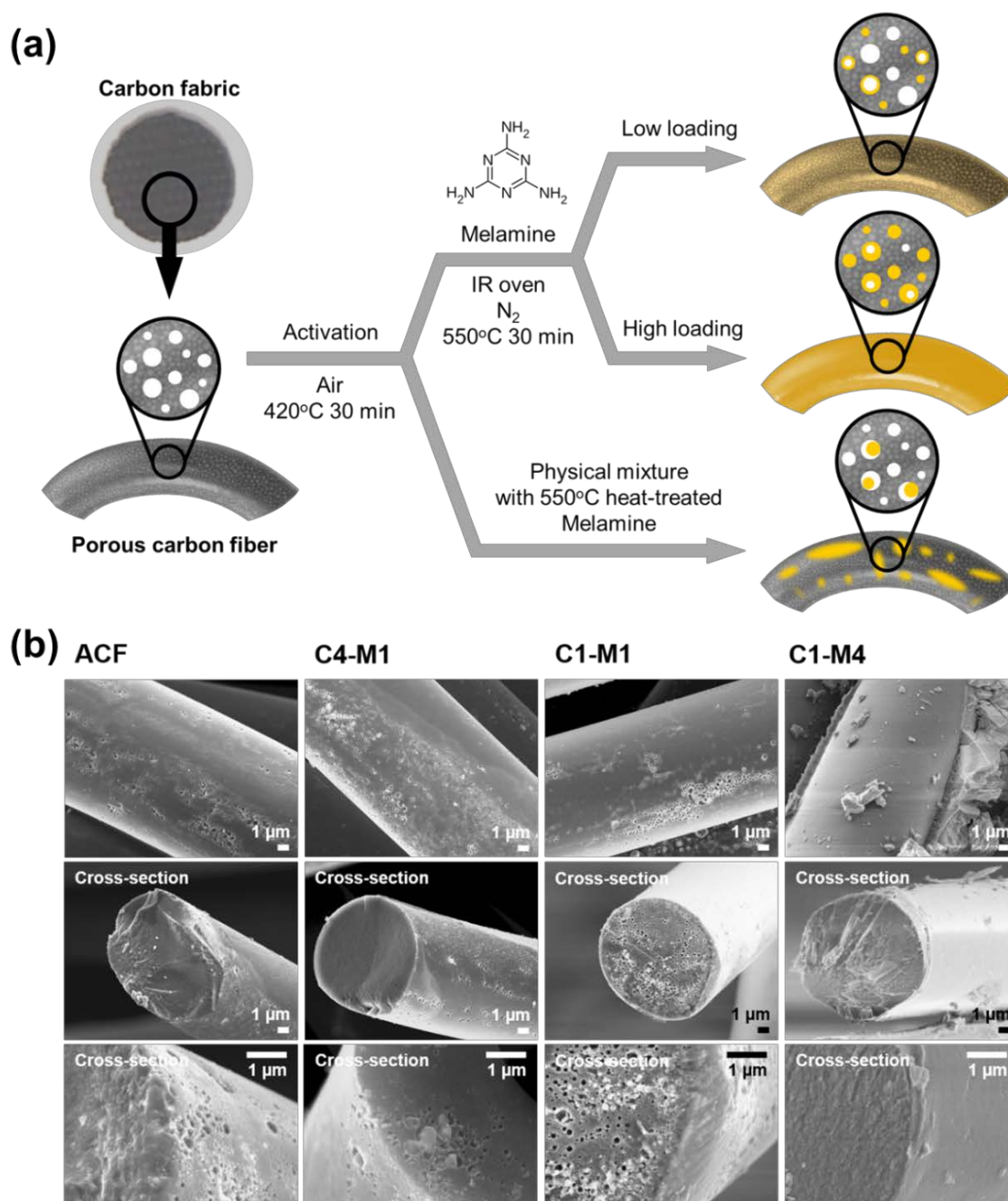
Figure 29. (a) Preparation of carbon fiber/melamine hybrid materials (Cx-My) with different amounts of melamine as well as (b) SEM images of ACF and Cx-My materials prepared with low (C4-M1), medium (C1-M1), and high (C1-M4) melamine content.

Figure 29(a) depicts the preparation procedure of nanohybrid materials by condensation of melamine on commercially available porous carbon fibers (Kynol activated carbon fabric ACC-5092-20 with $1800 \, m^2 \, g^{-1}$ of specific surface area) as the conductive framework. Oxygen-containing surface functional groups introduced by activation of the carbon fibers at 420^oC for 30 min under ambient air increase the surface polarity of carbon and provide anchoring sites for melamine deposition thus ensuring sufficient wetting of the carbon surface and the formation of a homogeneous nano-mixture.[296,297] For that purpose, melamine and ACF were mechanically mixed and placed in a crucible into an IR oven followed by fast heating to $550°C$ for 30 min under N_2 flow to decompose, redepositing and polymerizing melamine (a typically applied precursor and temperature for synthesis of carbon nitride, C_3N_4) to a nitrogen-rich carbon phase inside of the ACF by a chemical-vapour deposition-like process.[262,298]. Prepared composites are denoted as Cx-My, where x and y represent the mass ratio of ACF (x) to melamine powder (y) before the heat treatment. For the preparation of the physical mixture pm-C1-M2, melamine was heated in the IR oven to 550^oC for 30 min and mixed with ACF in the same ratio as N-rich carbon and ACF are present in C1-M2 after thermal infiltration (assuming that the heating does not affect the mass of ACF). **Figure 29(b)** shows the SEM images of ACF, C4-M1, C1-M1, and C1-M4. The fiber-like morphology is maintained after melamine loading and condensation. While samples with less melamine precursor still have apparently an open porosity comparable to the ACF, C1-M4 seems to be overloaded with N-rich carbon as it has a rather dense appearance and even contains typical flake-like polymerized melamine on its external surface. Energy-dispersive X-ray spectroscopy (EDX) measurements of the sample C1-M2 shown in **Figure S20** prove that nitrogen-containing species indeed infiltrated pores over the entire cross

section of the fiber during thermal infiltration. EA data and the areal weight of composite electrodes as shown in **Table S3 and Figure S21**, respectively, also suggest that the higher content of melamine in the precursor mixture improves the weight content of nitrogen. This renders direct vapour-phase infiltration of ACF with decomposed melamine a suitable method for the synthesis of carbon/N-rich carbon composite materials with controllable nitrogen content. The overloading of ACF in case of C1-M4 can also be seen in the optical images of various nano-mixtures as shown in **Figure S22**. The material prepared with the highest melamine loading clearly has a much brighter colour resulting from condensed melamine on the external surface of the carbon fibers. This also indicates that the external condensation of melamine in the highly loaded sample increases the areal mass compared to the limited increase from C1-M1 to C1-M2.

4.3 Pore structure analyses of Cx-My composites with different absortives

SEM images of melamine treated at 550°C (Mel-550), C1-M2, and the pm-C1-M2 are shown in **Figure S23**. Mel-550 indeed shows the typical flake-like morphology. In case of pm-C1-M2, the external surface of carbon fibers is covered with large chunks of condensed melamine resulting in an appearance that is comparable to the overloaded C1-M4 composite. However, filling of the narrowest pores in the ACF is unlikely to occur with simple physical mixing.
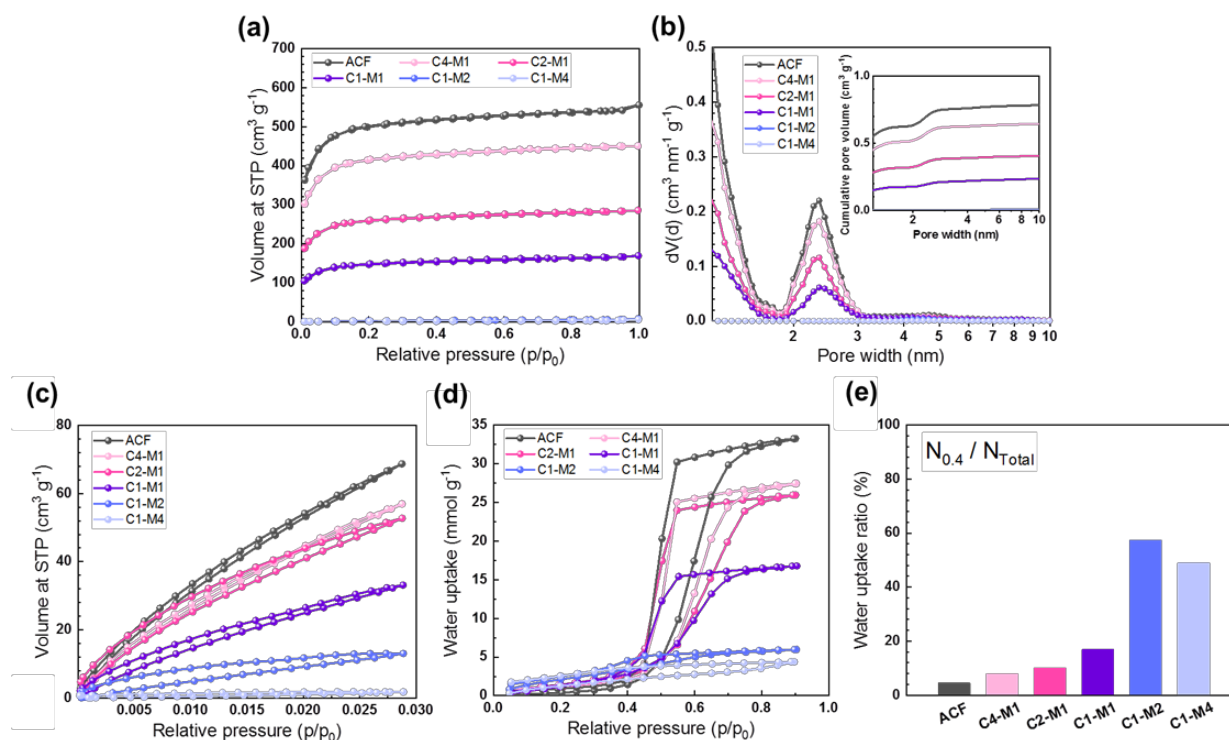
Figure 30. (a) N_2 physisorption isotherms (77 K) of Cx-My materials, (b) corresponding differential and cumulative (inset) pore volume. The physisorption isotherms by (c) CO_2 at 273 K and (d) water vapor at 298 K. (e) Ratio between the water uptake at $p/p_0 = 0.4$ ($N_{0.4}$) and the total water uptake (N_{total}).

Results of gas physisorption analyses with different adsorptives are shown in **Figure 30** and **Table S4**. N_2 physisorption isotherms at 77 K shown in **Figure 30(a)** indicate that ACF and Cx-My mixtures have a type I isotherm, as typical for microporous materials.[79] As expected, the V_{Total} of the composites decreases as the content of melamine increases. Based on the areal mass of electrodes summarized in **Figure S21**, the mass increase of fabricated Cx-My in comparison to the ACF ranges from ~20% to more than 100%. On the other hand, the corresponding decrease of the V_{Total} exceeds the mass ratio of melamine loaded. This further suggests that condensed melamine is not only located on the surface of carbon fibers but that a rather large amount is infiltrated inside of the micropores of ACF, supporting the hypothesis of a nanoscale hybrid material formation by the performed thermal decomposition-redeposition strategy. This is also confirmed by pore size distributions shown in **Figure 30(b)**. The pore volume of ~2.5 nm sized pores and especially of the pores below 1.0 nm is reduced as the content of melamine increases without any severe change of pore size. The quantity of adsorbed N_2 goes down close to zero for the highly loaded composites C1-M2 and C1-M4. On the one hand, condensed melamine leads to complete blocking of the pores of the ACF, but the presence of smaller pores that remain undetected by nitrogen at cryogenic temperatures cannot be ruled out. CO_2 has not only a smaller kinetic diameter (3.30 Å) than N_2 (3.64 Å), but an approximately 3 times higher quadrupole moment than N_2.[102,153,281] It is therefore most likely a more suitable adsorptive for analysis of the ultra-micropore structure and the Li^+ interactions at the electrode-electrolyte interface in LICs. CO_2 physisorption analyses are performed at two different temperatures (273 K as shown in **Figure S24** and 298 K as shown in **Figure 30(c)**), and corresponding ultra-micropore volumes ($V_{Ultramicro}$) calculated by the non-linear density

functional theory (NLDFT) are summarized in **Table S4**. The data confirms the trend observed from N_2 physisorption analysis that higher melamine loading leads to blocking of pores due to the formation of nanoscale carbon/N-rich carbon materials. Water physisorption analyses can be an even more reliable method to analyze porosity that is available for Li^+ storage due to the small kinetic diameter of H_2O molecules and their high polarity.[299,300] Water physisorption isotherms shown in **Figure 30(d)** again indicate that the total water uptake (N_{Total}) is reduced as the ratio of melamine-derived carbon in Cx-My increases, but the adsorbed amount does not go down to zero even for C1-M4. While ACF and the composites with lower melamine loading have high water uptake with the typical broad hysteresis that is observed for microporous carbon materials,[299] C1-M2 and C1-M4 have a less pronounced hysteresis. This is most likely due to their smaller micropores which do not provide enough space for phase transitions of water molecules. Accordingly, the water uptake at $p/p_0 = 0.4$ ($N_{0.4}$) in relation to N_{Total} at the highest relative pressure is significantly higher for C1-M2 and C1-M4 as shown in **Figure 30(e)**. This comparison confirms their pronounced hydrophilic character and small pore size as water-pore interactions seem to be dominant in comparison to the other samples where water-water interactions play a more important role.[285,301,302]

4.4 Structure-related electrochemical performance of the composite as LIC anode materials
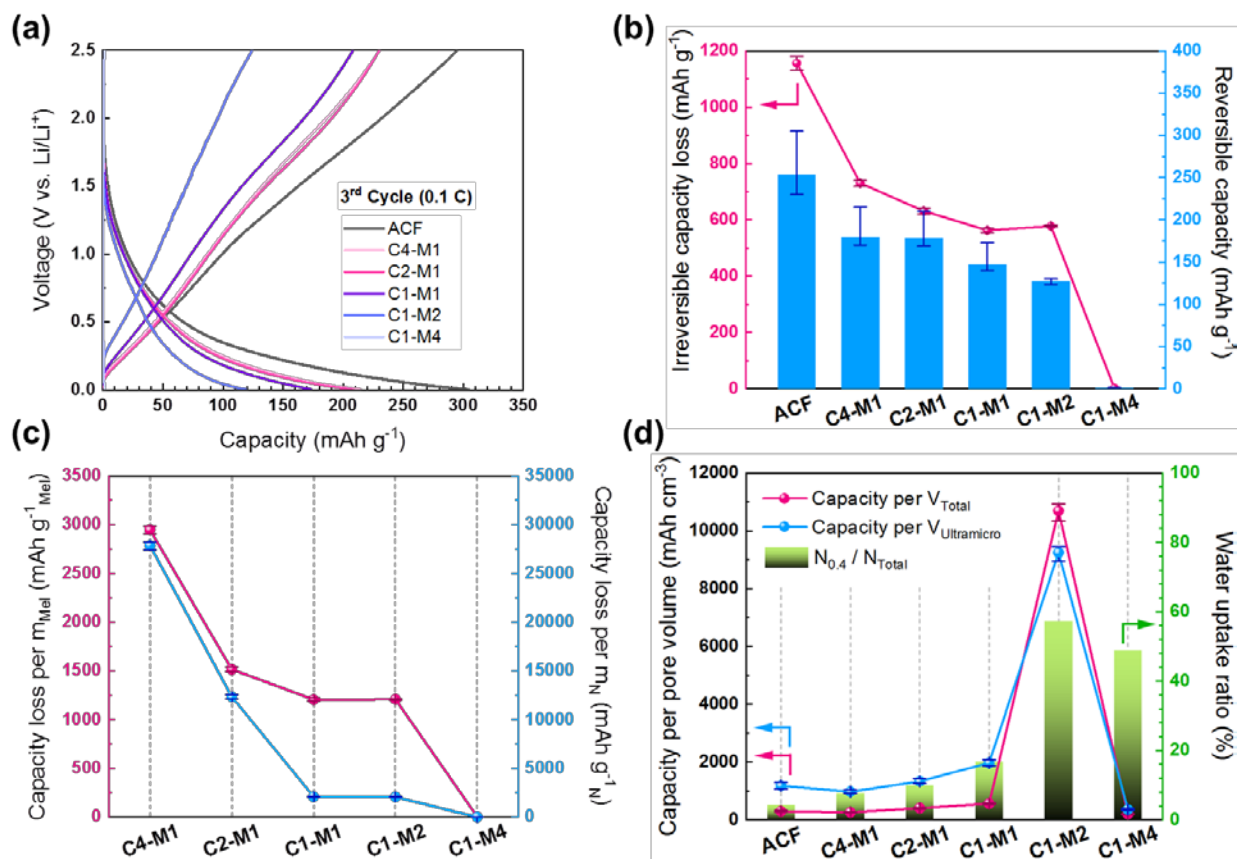
Figure 31. (a) Galvanostatic voltage profiles of the 3rd cycle (at 0.1 C) of ACF and Cx-My materials and corresponding (b) irreversible capacity loss and reversible capacity. (c) Correlation between the irreversible capacity loss and the m_{Mel} and m_N as well as (d) correlation between reversible capacity, the pore structure (V_{Total}, $V_{Ultramicro}$), and water uptake ratio ($N_{0.4}/N_{Total}$) calculated from water physisorption analyses (see Figure 30(e)).

The electrochemical performance of the Cx-My samples as LIC anode material has been investigated to conclude on the influence and interplay between the ratio of N-rich carbon/carbon

and the porosity on the Li storage capacity and mechanism. Galvanostatic voltage profiles of Cx-My materials and ACFs measured in half-cell tests as shown in **Figure S25** at a rate of 0.1 C (3rd cycle) are summarized in **Figure 31(a)**. From 3.0 – 0.0 V vs. Li/Li$^+$, the profile is dominated by sloping capacity which refers that ACF and composite electrodes store Li-ions at the electrode-electrolyte interface mostly by a capacitive mechanism without significant contribution of charge transfer.[303,304] As shown from the averaged data from three experiments as displayed in **Figure 31(b)**, ACF shows not only the highest capacity but also the highest initial irreversible capacity loss (calculated by subtracting capacity in the 3rd cycle from the 1st lithiation capacity as shown in **Figure S26**) due to its high V$_{Total}$ and specific surface area, providing many defect sites available for the irreversible formation of the SEI layer.[305] The emerging plateau (~0.3 V vs. Li/Li$^+$) during the first cycle most likely represents beginning of partial electron transfer from the carbon materials to lithium ions.[306] Likewise, **Figure 31(c)** shows that there is a decrease of the irreversible capacity loss with an increasing content of melamine (m$_{Mel}$) and nitrogen (m$_N$) in the Cx-My materials.

Moreover, the pore structure of the composite also largely affects the reversible capacity values as shown in **Figure 31(d)**. The capacities per V$_{Total}$ and V$_{Ultramicro}$ are both the highest in C1-M2. This is following a similar tendency as the N$_{0.4}$/N$_{Total}$ calculated from water vapor physisorption shown in **Figure 30(e)**. As discussed, water is a very suitable probe molecule to conclude on the Li storage properties of the Cx-My materials.[307] C1-M2 with its pronounced hydrophilic character represents the highest reversible capacity per pore volumes as well. Likewise, the pore volume available for Li storage is best to be determined by the adsorption of a polar gas whereas

the pore volume from established adsorptives like N_2 and Ar at cryogenic temperatures can easily lead to misleading expectations on the electrochemical properties of a given material.[308]

To investigate the C-rate dependence of LIC electrodes from Cx-My materials, rate capability tests were conducted in the range from 0.1 to 1.0 C as shown in **Figure 32(a)**. At a low rate of 0.1 C, C4-M1 shows 180 mAh g^{-1} discharge capacity (averaged over 4 experiments), while ACF has 254 mAh g^{-1} at the same rate. 127 mAh g^{-1} are measured for C1-M2 at 0.1 C as summarized in **Figure S27**. Even though the capacities of Cx-My at low current rate are smaller than that of ACF due to their inferior initial capacity, the capacity of Cx-My at 1.0 C of high rate becomes comparable (averaged discharge capacities of ACF, C4-M1, and C1-M2 at 1.0 C are 19.6, 17.3, and 5.5 mAh g^{-1}, respectively). Nitrogen present in Cx-My increases the polarity of electrodes and enhances electrolyte wetting as well as the lithium transport in small pores especially at high rate.[309] This tendency is also observed in other Cx-My composites in **Figure S28**, and corresponding averaged discharge capacities are shown in **Figure 32(b)**.

Discharge capacities set in relation to V_{Total} (**Figure 32(c)**) and $V_{Ultramicro}$ (**Figure 32(d)**) elucidate that C1-M2 shows superb capacity at all rates. This implies that the contribution of micropores and ultra-microporous with lithiophilic sites to the capacity is not negligible even at high current rate. A long-term cyclability test as shown in **Figure 32(e) and Figure S29** confirms that C1-M2 maintains stable cycling during 50 charge-discharge cycles at 0.1 C. The capacity retention of C1-M2 and ACF after this test equals to 74.7% and 61.1% of their initial capacity, respectively.
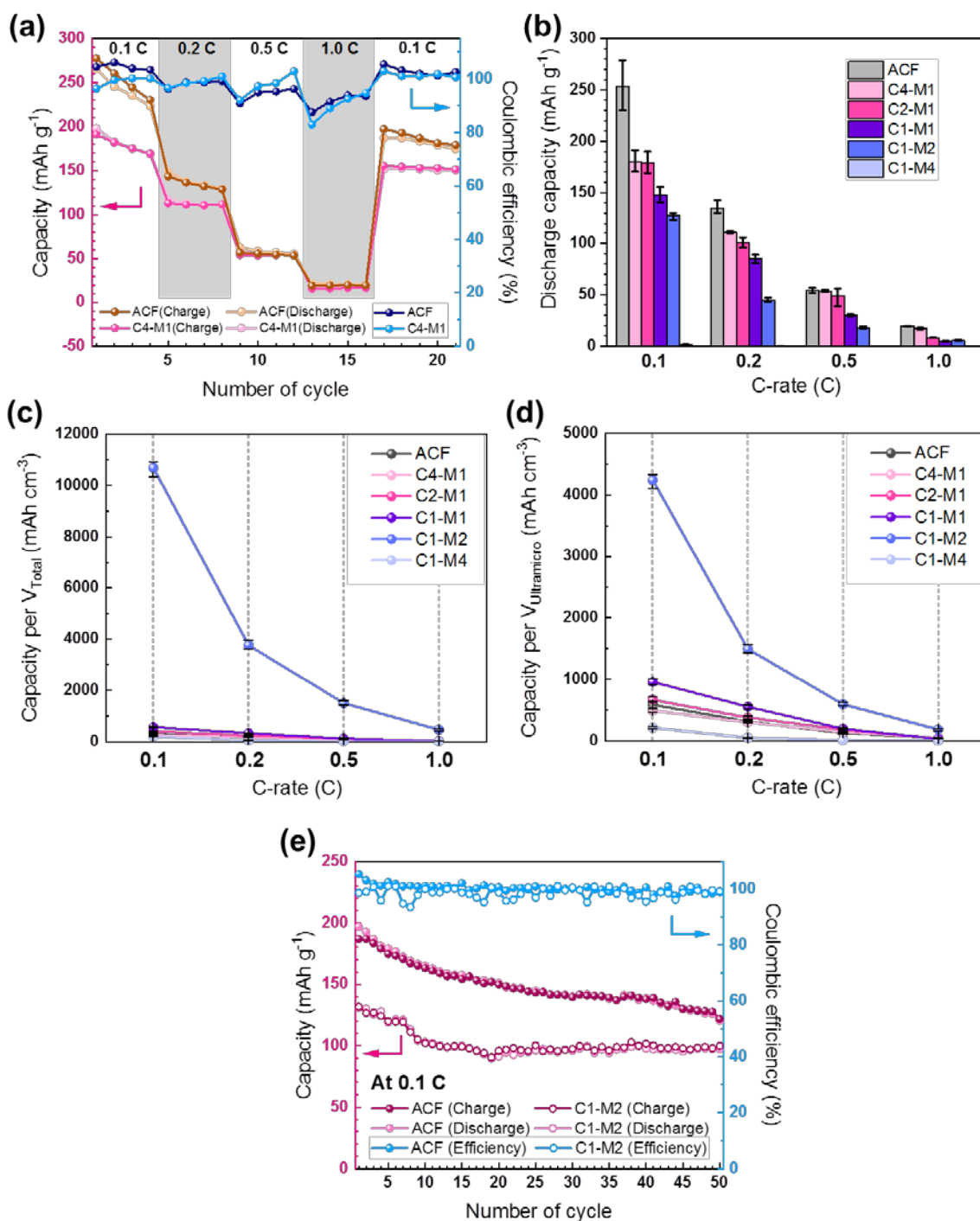
Figure 32. Rate capability tests of (a) ACF and C4-M1 from 0.1 to 1.0 C-rate, (b) discharge capacities of ACF and Cx-My materials at different C-rates, and corresponding correlation between discharge capacities and (c) V_{Total} or (d) $V_{Ultramicro}$. (e) Long-term cyclability test of ACF and C1-M2 during 50 cycles at 0.1 C.

5. Conclusions and perspectives

The goal of this thesis was to synthesize lithiophilic all-carbon composites with various pore structures to investigate how structural characteristics are expressed as electrochemical characteristics when the material is used as a LIC electrode material. For this purpose, hierarchically porous carbon was prepared, and a series of different composites was rationally synthesized with a nitrogen-rich noble carbon-based material. Pore structure was controlled through facile changes of synthetic factors such as a ratio of carbon vs. nitrogen-containing materials or the application of a different drying protocol during the synthesis. As a result, the finite composite formation on the nanoscale was achieved. To understand the structure-property relations of composites as electrode materials in LIC, various gas adsorption analyses (N_2, CO_2, and H_2O at different temperatures) were conducted and set in relation with the electrochemical tests. Two main composite systems were elucidated for understanding the correlation between pore structure and the performance of LIC.

In the first chapter as described in **Figure 33** (**Chapter 3**), a particle-like (0-dimensional) all-carbon composite was investigated. Porous all-carbon composites between ZnO-based hard-templated carbon and nitrogen-containing HAT-CN derived N-doped carbon were fabricated and applied as anode materials in Li-ion capacitors. The textures and chemical compositions of the composites are influenced by the loading method and ratio of HAT-CN and by the condensation temperature. Slowly dried s-HAT composites have a more uniform HAT distribution whereas f-HAT composites that underwent faster drying have a less homogeneous mixing between both

compounds. In the latter case, redistribution between HAT-derived N-doped carbon and ZTC can occur after condensation at temperatures above 550°C. High nitrogen content and homogenous mixing on the nanoscale improve the adsorptive storage of Li-ions at the interface between electrolyte and composite materials. Consequently, the capacity achieved by s-HAT4-550 is superior to the reference materials (ZTC and HAT-1000) and other composites (pm-HAT-ZTC, f-HAT4-550) independent of the chosen current density. These results of this optimization study elucidate the crucial relationship between the LIC cell performance, and the textures and chemical compositions of all-carbon composite materials. Last but not least, it should be stressed out that all the materials discussed here show capacitive lithium storage properties without a distinct plateau. Redox-based processes are likely to occur if such materials would be utilized as cathodes in LIBs and it remains an interesting question, if and how much improvement can be expected when such a hybridization strategy would be applied on the other side of the device.

In the second project (**Chapter 4**), a fiber-structured (1-dimensional) all-carbon composite was investigated. Homogeneous nitrogen-rich all-carbon nanohybrid materials (Cx-My) were fabricated by simple heating of the mixture of porous carbon fibers and melamine in an IR oven. The V_{Total} and $V_{Ultramicro}$ are regulated by the ratio of mixed melamine and carbon fibers, which also influences the surface polarity of the mixtures. N_2, CO_2, and water physisorption analyses at different temperature showed different polarities and pore accessibilities depending on the size and polarity of the adsorptives. Among them, water physisorption provided the most conclusive insights into the interplay between pore structure and lithiophilic character of the surface and the properties of the Cx-My when applied as anode materials in LICs. Nanoscale mixing of both compounds is necessary to efficiently combine lithiophilic sites and electric conductivity.

Likewise, the content of nitrogen-doped carbon and remaining pore volume need to be carefully optimized. Even though increased loading of melamine in Cx-My reduced the absolute values of the capacity, it enhanced the reversibility of Li-ion storage due to the decrease of irreversible processes. Cx-My hybrid materials also showed an enhanced rate capability and a long-term stability compared to the ordinary activated carbon fibers. Especially, C1-M2 showed the highest capacity per V_{Total} or $V_{Ultramicro}$ even at the high current rate, suggesting water physisorption can be a powerful tool to understand the correlation between the pore structure and the electrochemical performance of LICs.

Figure 33. Hierarchical composite materials of electrically conductive highly porous templated carbon matrices with a nitrogen-rich carbon material are synthesized and characterized as anode model materials for lithium-ion capacitors. Controlling uniformity, content of lithiophilic sites, and pore structure of the composite is the key factor to achieve high and stable capacity. Structure-property relationships of HAT/ZTC composites are analyzed in detail in Chapter 3.

In conclusion, the results summarized from these two topics showed that the design of homogeneous all-carbon composites was crucial for the properties of the LIC electrodes. Especially, controlling or fine-tuning of pore structure was essential to obtain further improvement, which led us to understand the fundamental knowledge of correlations between structural characteristics and electrochemical properties of composites.

Even though there are open questions such as the mechanism of Li transport in the composites or the changes of the pore systems during the charging-discharging process, it seems to be important to provide materials with additional pathways and interacting sites. Another carbon matrix possessing a hierarchical pore network and high electrical conductivity could be further employed to investigate the structure-related Li storage properties and could also be optimized towards its volumetric lithium storage properties which are often the more crucial benchmark for practical applications. On the other hand, N-rich precursors with different types of heteroatoms which induce a high surface polarity (or lithiophilicity) at the electrode-electrolyte interface could be beneficial to widen the possibility to derive other types of interactions between the alkali metal ions and active sites. Consequently, various sets of all-carbon composites could be fabricated, resulting in novel composite materials not only for LIC electrodes but also for a new range of applications like LIBs, electrochemical capacitors, and catalysis.[233,246]

Moreover, to achieve a "dream-electrode", it is possible to utilize other hybrid candidates with the similar principles discussed here besides all-carbon hybrid composites. Most of the fundamentals also can be applied to carbon/non-carbon composites such as electrically conductive carbon hybrid with non-carbonaceous functional materials which interact with Li-ions by their high surface polarity.[264] Or, hybrids between conductive non-carbonaceous matrix

and carbon with high contents of functional groups are possible vice versa: Even though they are not much feasible in reality since carbon-based materials have high chemical stability and high electrochemical reversibility at relevant conditions. No matter which material combinations would be the most effective composite system, the understanding fundamentals and lessons from researches on all-carbon hybrid materials are critical to expanding the boundary, which links to comprehension of other inorganic materials as well.

The traditional way (heat-treatment or infiltration) of all-carbon hybrids synthesis also can be changed to alternative methods such as gas-phase deposition or laser-induced carbonization.[262,267] As rarely investigated these methods could provide different points of view and clues about confinement effects in the porous composites as well as details about the individual reaction mechanisms. Consequently, such alternative synthetic approaches could lead to further clearer elucidation for the ambiguous scientific questions behind carbon-based hybrid materials.

6. Appendix

6.1 List of abbreviations

Abbreviation	Full name
LIC	Lithium-ion capacitor
LIB	Lithium-ion battery
EDLC	Electrochemical double layer capacitor
SBA	Santa Barbara amorphous-type material
MOF	Metal-organic framework
ZTC	ZnO-templated carbon
HAT-CN	Hexaazatriphenylene-hexacarbonitrile
ACF	Activated carbon fiber
IR	Infra-red
EA	Elemental analysis
SEM	Scanning electron microscopy
EDX	Energy-dispersive X-ray spectroscopy
TGA	Thermogravimetric analysis
BET	Brunauer-Emmett-Teller theory
IUPAC	International Union of Pure and Applied Chemistry
SSA	Specific surface area
QSDFT	Quenched solid density functional theory
NLDFT	Non-linear density functional theory

XRD	X-ray diffraction
EIS	Electrochemical impedance analysis
f-	Fast-evaporated
s-	Slow-evaporated
pm-	Physically-mixed
V_{Total}	Total pore volume
$V_{Ultramicro}$	Ultramicropore volume
m_{Mel}	Mass of condensed melamine after the heat treatment at $550^{o}C$
m_N	Mass of nitrogen
EC/DEC	Ethylene carbonate/Diethyl carbonate
SEI	Solid electrolyte interphase

6.2 Characterization methods

Elemental analysis (EA)

EA is the technique to quantify the elemental chemical composition of a sample by combustion. EA is preceded by three sequential steps: (1) the combustion step, (2) the reduction step for generating small-molecule gases, and (3) the separation/detection of the formed gases. In detail, the loaded sample is heated up to 1000°C under an oxygen atmosphere to fully oxidize it. After that, the sample is turned into small gas molecules such as nitrogen, water, and carbon dioxide. Finally, these generated gas molecules are classified and quantified. In general, EA detects hydrogen, carbon, nitrogen, and sulfur, which are measured by the thermal conductivity sensor to obtain precise quantification results. Here, a Vario Micro model is utilized for achieving the EA result of C/H/N/S with the combustion analysis as mentioned above, and Mrs. Antje Völkel[2] produced data available in this thesis.

Scanning Electron Microscopy (SEM)

SEM is an imaging technique based on interactions between the target specimen and and electron beam with high energy. The electron beam is generated in the vacuum chamber by an accelerated electron gun which is located at the top of the microscope and vertically directed towards the sample. By the utilization of electromagnetic field, this electron beam is accelerated and focused as a fine spot by subsequent lenses to obtain meaningful analyzable signals. The resulting signals contain information about the surface morphology and the chemical composition of the target.

[2]Max Planck Institute of Colloids and Interfaces, Am Mühlenberg 1, 14476 Potsdam.

When the incident beam interacts with the specimen, X-rays and three types of electrons are mainly produced: secondary electrons, backscattered electrons, and Auger electrons. SEM generally detects secondary electrons and backscattered electrons from the produced signals. In this work, the signal of secondary electrons is mainly used for imaging.

The excited secondary electrons can be detected at the surface of the target, because these electrons generally have a low energy level and move only close to the surface for escaping from the specimen. As a result, this signal is significantly sensitive to surface properties. It is possible to understand the topology of the target surface since released electrons are mostly cumulated at the edge curvatures or points. Moreover, the brightness of images can be fluctuated by the angle of the incident electron beam. This is because the contrast gradient of the scanned image or intensity of the signal is determined by the increased amount of secondary electrons. Based on the contrast difference depending on the surface properties, SEM imaging provides 3-dimensional images by monitoring signals from the interaction between incident electrons and the specimen during scanning over it.

Unlike secondary electrons, backscattered electrons are applied when the specimen consists of distinct chemical components with high contrast (e.g. heavy metal decorated carbon catalyst). This is because the contrast of images is determined by the number of backscattered electrons. Heavy atoms (i.e. atoms with a higher atomic number) release more backscattered electrons, and the domain with a high concentration of these atoms is detected as brighter images than the domain without them. In addition, as they possess comparably higher energy than that of secondary electrons, it is effective to image the sample in deeper regions where a large penetration depth is needed.

For the better quality of imaging, conductive metal such as gold and platinum is sputtered on the target with a few nanometer thicknesses, which facilitates the efficient release of the electrons by making the surface more conductive. Thus, even the nanometer-sized structures also can be visualized. In this work, Leo Gemini 1550 (Zeiss) SEM is utilized in Max Planck Institute of Colloids and Interfaces, Potsdam.

Energy Dispersive X-Ray Spectroscopy (EDX)

EDX is the method that is often coupled to SEM to obtain qualitative chemical information about the specimen. It is suitable for understanding elemental composition by identifying the energy fingerprint of specific individual X-ray generated from certain elements of the sample. This X-ray is irradiated when the accelerated electron beam excites the electrons in the inner orbitals, resulting in holes at inner shell of the atom. After this release of the electron, generated electron-hole is then occupied by the electrons of the outer shell with higher energy which releases X-ray radiation. The energy of the released X-ray is determined by the energy gap between the energy state of the inner shell and the outer shell. This X-ray shows characteristic lines at the distinct energy level, which are detected in the emission spectrum. Commonly, the spectrum lines are notated as the origin of the shell as K- or L-line where electrons are initially excited. Detected characteristic lines are unique depending on the type of element so that it is possible to determine which kind of element is contained in the sample as well as the atomic content by measuring the number of released X-ray photons. Such detections enable both qualitative and quantitative EA.

This EDX machine is generally attached at SEM to utilize the same source of electron beam. However, the penetration depth of the electron beam accelerated from the beam source of SEM

is low so that the chemical composition of the sample can be analyzed only near the surface with a broad area.[310] Even though EDX is not a suitable technique for bulk analysis as noted above, it is facile and useful to comprehend the local elemental distribution of the sample surface with different techniques including point, line, and mapping analyses. EDX analyses were carried out using X-Max (Oxford instruments) after the Pt sputtering by Mrs. Heike Runge.[3]

Thermogravimetric Analysis (TGA)

TGA is a combustion method that allows quantifying physical phenomena (adsorption/desorption of gasses, the loss of solvent, phase transition) and chemical phenomena (pyrolysis, oxidation, the residue after the complete thermal decomposition).[311] It is commonly utilized to evaluate the thermal stability of the sample. TGA analysis detects the mass change of the sample at the constant rate of heating up to 1000°C in a controlled atmosphere (e.g. in inert, oxidative, reductive gas, or in vacuum). During the thermal decomposition process, this mass change is recorded as a function of time of temperature. In general, TGA can be coupled with a mass spectrometer (MS) or Fourier-transformed infrared spectroscopy (FT-IR) to analyze the generated gases from the decomposition. By this, detailed information on the composition of the sample and the decomposition mechanism during the heating can be collected. In this work, TGA analyzer located in Max Planck Institute of Colloids and Interfaces was used for the analysis with Pt crucible and 10 mg of sample within the error of 1 mg.

---

[3]Max Planck Institute of Colloids and Interfaces, Am Mühlenberg 1, 14476 Potsdam.

Gas Physisorption Measurements

The gas physical adsorption (physisorption) is an effective, well-known analysis to investigate not only the porous structure of the materials, but also the texture of the pores including pore dimension, surface polarity, and geometry. The process of physisorption is driven by van der Waals interactions between the surface of the porous specimen (adsorbent) and the gas molecules (adsorptive). As van der Waals force is a weak intermolecular force, the physical adsorption is largely affected by the pore architecture as well as the interaction between adsorbent-adsorptive. The shape of the physisorption isotherm is affected by all parameters above as well as the related pore properties including V_{Total}, SSA, and pore size distribution. Those can hence be calculated based on the measured physisorption curves. In 2015, the IUPAC announced the pore classification by the width of pore and which is named into three groups: macropores (width > 50 nm), mesopores (50 > width > 2 nm), and micropores (width < 2 nm).[79] More specifically, the micropore can be further classified as supermicropores (2 > width > 0.7 nm) and ultramicropores (width < 0.7 nm).

To obtain the physisorption isotherms, either a gravimetric or a volumetric measurement is applied after the selection of gas. In general, several subcritical fluids at cryogenic temperature (N_2 at 77 K or CO_2 at 273 K) are utilized for high-resolution gas adsorption analyses. Among these fluids, nitrogen physisorption is the most well-established technique to obtain pore properties (V_{Total}, SSA, and pore size). The measured physisorption curve is projected as the amount of absorbed gas at the surface of the adsorbent vs. the relative pressure (p/p_0) calculated from the saturation pressure (p_0) at the given temperature and the measured pressure (p).
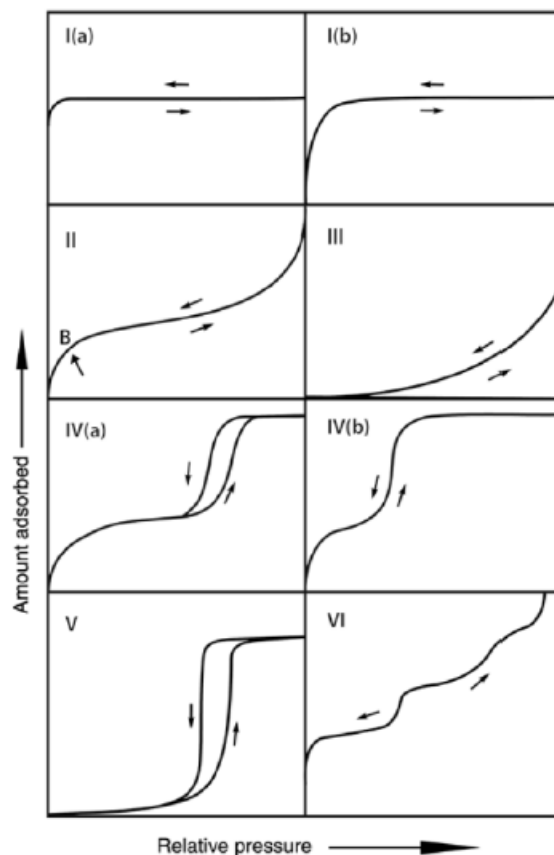
Figure 34. Classification of physisorption isotherms by IUPAC.[79]

As described in **Figure 34**, the obtained N_2 physisorption isotherms can be differentiated into 8 different types as suggested by IUPAC in 2015.[79] When the majority of pore width is ranged in size of micropore (i.e. ultramicropore or supermicropore), the type I shape is achieved. N_2 filling in ultramicropore derives type I(a) isotherm, while supermicropore derives type I(b), respectively. The main difference between type I(a) and type I(b) is the onset filling in micropore, the amount of absorbed gas at a low relative pressure range (p/p_0 ~0.01), which is affected by pore morphology, size, and surface roughness or nature of adsorbent. In the case of ultramicropore (type I(a)), the filling process entirely relies on the interaction between solid and gas at the pore interface, resulting in a continuous onset filling at p/p_0 < 0.01. On the other hand, not only the

interaction between adsorbent solid and adsorptive gas but also the increased intermolecular force among adsorptive gas molecules in the larger supermicropore involve simultaneously during the onset filling, resulting in lower amount of N_2 adsorption at $p/p_0 < 0.01$ range (type I(b)). On the other hand, when the specimen has macropores, the N_2 physisorption isotherm is displayed as a type II. This is because the accumulated nitrogen molecules first form a monolayer at the surface of adsorbent, and the subsequent layers are cumulated on this monolayer as a multilayer. The unique feature of type III and type V isotherm is the small amount of absorbed N_2 molecules at low p/p_0, indicating the surface of the adsorbent is not fully covered with adsorbate gas due to the lack of strong binding between them. As a consequence, these type III and type V isotherms are achieved when the binding energy between porous adsorbent and adsorbate N_2 molecule is relatively weak. A type IV isotherm is a common shape for mesoporous samples. The hysteresis of the isotherm originates from the capillary condensation of N_2 (i.e. gas-liquid transformation) in the volume-confined mesopore. The different shape of hysteresis between type IV(a) and IV(b) is occurred by the pore width difference. The type IV(a) isotherm is achieved when the width of the mesopore is above a critical size (2 nm) for capillary condensation, while type IV(b) is achieved when the pore width is smaller than 2 nm, resulting in adsorption and desorption at similar pressure.[312] A type VI isotherm indicates that the adsorbed N_2 forms a stepwise multilayer at the surface of a non-porous specimen.

For the calculation of V_{Total} and SSA from the N_2 physisorption isotherm, the BET (Brunauer-Emmett-Teller) method is widely used for porous materials.[313,314] The BET method can be applied for meso-/microporous adsorbents based on the assumption that (1) the adsorbed gas

molecules form a continuous multilayer at the porous surface, and (2) the adsorption enthalpy between the first adsorbate layer and the surface of the porous material is different from that of the adsorbate layer between subsequent multilayers. From **Eq. 5** and **Eq. 6**, SSA is measured. In the **Eq. 5**, p/p$_0$ is the relative pressure, V_{ads} is the total volume of adsorbed adsorbates, V_M is the volume of adsorbate at the monolayer, and A is the adsorption constant:

$$\frac{(p/p_0)}{V_{ads}\,(1-p/p_0)} = \frac{1}{A\,V_M} \cdot \frac{p}{p_0} + \frac{1}{A\,V_M} \qquad (\textbf{Eq. 5})$$

When the left term of **Eq. 5** ($\frac{(p/p_0)}{V_{ads}\,(1-p/p_0)}$) is plotted as a function of p/p$_0$, V_M can be calculated from the slope of the resulting plot or intersection at the y-axis after extrapolation. By using this V_M value from **Eq. 5**, SSA can be finally achieved. In equation **Eq. 6**, N_A stands for the Avogadro constant, S_{N_2} stands for the surface area of a single N$_2$ molecule in a dense package (0.162 nm^2), V_{mol} stands for the volume of an ideal gas, and m_{ads} stands for the mass of the adsorbent.

$$\text{SSA} = \frac{V_M \cdot N_A \cdot S_{N_2}}{V_{mol} \cdot m_{ads}} \qquad (\textbf{Eq. 6})$$

For the advanced calculation of SSA, the density functional theory (DFT) is utilized as a tool for microscopic analysis of micro-/ mesopores. Especially in this thesis, advanced quenched solid density functional theory (QSDFT) is applied to determine SSA and pore width due to the surface roughness and non-homogeneous heteroatom doping in the nitrogen-rich porous carbon composites.[315]

As N$_2$ physisorption analysis is limited for analyzing the pore larger than 0.45 nm, CO$_2$ physisorption is applicable as an alternative adsorbate to understand the microporosity of the

sample. At 273 K, CO_2 has 26141 torr of high saturation pressure (p_0), and it is only 31 K below the critical temperature (304.1 K). It makes CO_2 physisorption possible to investigate micro-sized pore (d < 2 nm) of adsorbent with a short period of time. This is due to the fact that the improved molecular kinetics at elevated temperatures, and the increased gas uptake in the range of 1 to 760 torr (absolute pressure) where the measurement of p/p_0 for micropores is conducted.[316] In addition, CO_2 physisorption analyses are beneficial for heteroatom-rich microporous materials such as metal-organic frameworks (MOFs), nitrogen-rich carbon composites, and zeolites thanks to high quadrupole moment of CO_2, leading to facile interaction with the adsorbent which has a high surface polarity (e.g. polar functional groups, heteroatom-doped sites). Even though it is intricate to investigate the detailed pore properties from CO_2 physisorption which is influenced by various factors, CO_2 physisorption is one of the useful techniques to understand the microporous structure of the adsorbent.[317]

As an alternative method, water vapor (H_2O) physisorption also provides vast amounts of information about the micropore system. Water vapor has a smaller kinetic diameter (0.265 nm) than that of CO_2 or N_2 at cryogenic temperature, making it possible to fill the ultra-micropores where CO_2 and N_2 cannot approach.[318] Additionally, water shows 1.855 D of high dipole moment, which leads to a strong interaction (i.e. hydrogen bonding and dipole-dipole interaction) not only between water molecules themselves but also between water and polar functional groups or heteroatoms at the surface of adsorbents. Water physisorption isotherms measured for carbon materials are therefore largely influenced by the surface characteristics (surface roughness, morphology), pore structure (porosity, pore size), and the surface polarity (contents of heteroatoms, density of polar functional groups, topology of functional groups) depending on the

measured temperature. Along with CO_2 physisorption, collected information from water physisorption generates a complementary understanding of pore structure and surface polarity. The hydrophobic porous specimen generally displays a type V shape of water physisorption isotherm with hysteresis as shown in **Figure 34**, while non-porous samples with small amounts of polar functional groups exhibit type III isotherm. In these cases, the obtained water vapor pressure at the onset point gets similar to the saturation vapor pressure of water. On the other hand, the initial uptake of water vapor enhances at the low p/p_0 region when the surface polarity of the adsorbent increases, resulting in type I, II, or IV isotherm. To achieve the gas physisorption and related results in this work, apparatus manufactured by Quantachrome Instruments (Quadrasorb apparatus) was used.

X-Ray Diffraction (XRD)

XRD is a technique to characterize crystalline materials to verify their crystallinity, atomic spacing, and lattice parameters. The reason why X-ray is attempted as a suitable analysis for crystalline specimens is that the wavelength of X-ray is in the same range as the atomic spacing. In this regard, using X-rays makes it possible to obtain meaningful information from nanometer-sized atom arrangement since it also possesses the same range of wavelength (1.0-1.0×10^{-5} nm). Commonly, monochromatic Cu-K_α radiation (0.15 nm of wavelength) is widely used, which is generated in the X-ray tube by the impact between the stationary/rotating Cu target and the focused electron beam accelerated by high voltage. Emitted X-ray through this collision is a combination of X-ray with the continuous spectrum and monochromatic X-ray whose wavelength is characteristic depending on the type of target. Between them, a monochromatic X-

ray with a unique line spectrum is applicable to XRD analysis.

When the loaded specimen is exposed to an incident X-ray beam, the scattering happens in a way of either elastic or inelastic diffraction. In XRD experiments, elastic coherent scattering (i.e. Rayleigh scattering) is mainly analyzed. If the sample is highly crystalline with an ordered structure, it amplifies the signal of diffraction a lot by a constructive interference (synchronized wavelength of diffraction). This constructive interference only occurs when the phase shift of waves (Δ) between incoming X-ray and diffracted X-ray is an integer multiple (n) of the wavelength of X-ray (λ). As the pathway of light is variable depending on the incidence angle of X-ray (θ) and the interatomic spacing (d) of parallel lattice planes, the condition for the constructive interference can be summarized as Bragg's law. (**Eq. 7**) XRD instruments record this scattering intensity as a function of angle (θ), resulting in the final diffraction pattern of the sample. The conditions satisfying Bragg's law induce the peak in the pattern due to the constructive interference. The size of the crystalline domain also affects the diffraction pattern. The smaller size of ordering broadens the peak due to the lattice imperfection and insufficient interference.

$$\Delta \; = \; n\,\lambda \; = \; 2\,d\sin\theta \quad \text{(Bragg's law, } \textbf{Eq. 7}\text{)}$$

The lattice plane for peaks in the diffraction pattern can be designated by corresponding Miller Indices (hkl) which is theoretically defined from the intersection between the unit cell of sample and reciprocal lattice of it. In practice, the JCPDS database card of previously reported materials provides a clue to unveil the lattice structure by comparing peak positions and the shape of the diffraction pattern. Additionally, as the incidence angle and the diffraction angle are both the

same as θ, 2θ values are adopted for the diffraction pattern data. If a powder sample is analyzed, a wide range of 2θ is recommended to confirm all possible diffraction directions because of the random orientation of the crystalline lattice in the powdered sample. In this work, a Bruker D8 Advance instrument (Cu-K$_\alpha$ radiation) in Max Planck Institute of Colloids and Interfaces was employed for collecting XRD diffraction patterns.

Raman Spectroscopy

Raman spectroscopy is a tool for the analysis of the lattice crystal or the amount of doping/defect site by detecting molecular vibration of the sample. This vibrational technique allows elucidation of local crystallinity, lattice stress, and defects, especially for carbon materials. After the loading of the sample, the monochromic laser beam with a certain energy level (Infra-Red, Visible, Ultra-Violet) as the light source is exposed to collect the resulting scattered laser using the lens. This obtained scattered light then passes through a sequential pathway with an interference filter (spectrophotometer) and charge-coupled analyzer, which gives a Raman spectrum of the sample. When applied light scatters the photons of the target, most of the scattered photons have the same energy as that of incident photons because laser is wavelength-synchronized. This scattering is called Rayleigh scattering, and thus the wavelength of the initial laser is exactly preserved after the scattering. That is, the excited electrons by the energy from the applied laser emit exactly the same energy when they fall back into the ground state as a form of scattered light. In this regard, Rayleigh scattering is considered elastic. Unlike Rayleigh scattering, only a few amounts of scattered photons are detected, whose frequency is changed from initial light frequency. This is called inelastic Raman scattering or Raman Effect as described in **Figure 35(a)**

and (b). As Raman scattering causes vibrational or rotational energy transitions in molecules or crystal lattices, the difference between applied laser energy and the scattered energy thus can be translated into the energy of vibration or rotation. The origin of Raman Effect is the interaction between photons of applied laser and the electric dipole of the molecule. When the energy of inelastic scattering is higher (or lower) than the initial energy, it is called Anti-Stokes (or Stokes). This resulting energy change generates a Raman peak shift by corresponding wavenumbers (cm^{-1}). The amount of the shift ($\bar{v}$) can be calculated by **Eq. 8** using the wavelength of incident laser (λ_{in}) and the scattered laser (λ_{out}).

$$\bar{v} = \frac{1}{\lambda_{in}} - \frac{1}{\lambda_{out}} \qquad \textbf{(Eq. 8)}$$
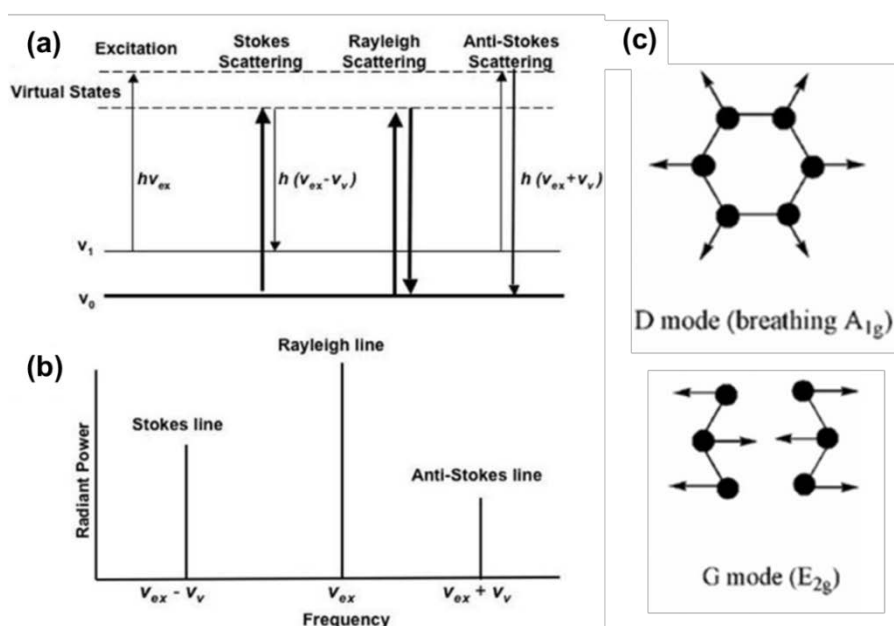
Figure 35. (a) Energy diagram of elastic Rayleigh scattering and inelastic Raman scattering (Stokes and Anti-Stokes) and corresponding (b) Raman peak shift in Raman spectra.[319] (c) Vibrational modes of carbon atoms generating D and G bands. Copyright 2015, John Wiley and Sons.[320]

Materials that lead to the occurrence of Raman shift (that is, a change in polarizability) are considered as Raman-active materials. For example, carbon materials are Raman-active and produce a characteristic D-band ($\sim$1350 cm^{-1}) and G band (between 1500-1600 cm^{-1}). These two bands arise from the different vibrational modes of six-membered carbon atoms with specific symmetry depicted in **Figure 35(c)** (A_{1g} symmetry with breathing-mode occurs D-band, E_{2g} symmetry occurs G-band). In general, defective carbon (e.g. less crystalline structure or heteroatom doped lattice) enhances and broadens D-band, so it is possible to determine which materials have more disorders in the lattice by comparing the peak ratio of D- and G-band. In addition, the peaks can be shifted because of the electron density of carbon. For instance, as the electronegative nitrogen doping shifts D-band to the high wavenumber, it can be indirectly confirmed whether a successful synthesis has been achieved.[321] In this work, a Witec Raman Microscope with the green laser source (532 nm) in Max Planck Institute of Colloids and Interfaces is utilized.

6.3 Experimental part

6.3.1 List of chemicals

Chemical	Chemical formula	Purity	Supplier
Hydrochloric acid	HCl	37%	Sigma-Aldrich
Ethyl alcohol	C_2H_5OH	$\geq$ 99.8%	Sigma-Aldrich
Sucrose	$C_{12}H_{22}O_{11}$	> 99.5%	Sigma-Aldrich
Sulfuric acid	H_2SO_4	98%	Merck
Zinc chloride	$ZnCl_2$	$\geq$ 98%	Alfa Aesar
Zinc oxide nanoparticles	ZnO (20 nm)	99%	Nanosturctured & Amorphous Materials, Inc.
Sodium hydroxide	NaOH	$\geq$ 98%	Sigma-Aldrich
Hexaketocyclohexane octahydrate	$C_6H_6 \cdot 8\ H_2O$	99%	Alfa Aesar
Diaminomaleonitrile	$C_4H_4N_4$	> 96%	TCI
Acetic acid	CH_3COOH	$\geq$ 99%	Sigma-Aldrich
Nitric acid	HNO_3	65%	Merck
Acetonitrile	CH_3CN	99.8%	Sigma-Aldrich
Dimethylformamide	C_3H_7NO (without stabilizer)	99.8%	Sigma-Aldrich
Carbon fiber Kynol ACC-5092-20	C	-	Kynol
Melamine	$C_3H_6N_6$	99.95%	Sigma-Aldrich
Carbon black (Super-P)	C	99%	Alfa Aesar
Sodium carboxymethyl cellulose	$[C_6H_7O_2(OH)_x(OCH_2COONa)_y]_n$ M_W ~250000 Degree of substitution = 0.7	99%	Sigma-Aldrich
Lithium	Li	99.9%	Sigma-Aldrich

Lithium hexafluorophosphate	$LiPF_6$	$\geq$ 99.99%	Sigma-Aldrich
Ethylene carbonate	$C_3H_4O_3$, anhydrous	99%	Sigma-Aldrich
Diethyl carbonate	$(C_2H_5O)_2CO$, anhydrous	$\geq$ 99%	Sigma-Aldrich

6.3.2 Synthesis of materials

Synthesis of ZTC

8.0 g of ZnO nanoparticles (20 nm, Nanostructured & Amorphous Materials, Inc.) were mixed with 7 g of sucrose (>99.5%, Sigma-Aldrich) into 13 mL of distilled water. After formation of a homogeneous dispersion, 0.4 g of powder NaOH were added and stirred. The mixture was then transferred to a petri dish and heated under air at 100°C for 3 hours and then to 160°C for 6 hours to polymerize the sucrose. Samples were then moved to a horizontal tube furnace for carbonization at 950°C for 2 hours under Ar flow with a ramping rate of 1°C min^{-1}. After cooling, samples were washed at least 3 times overnight with 1.0 M aqueous HCl solution. Final ZTC materials were filtered and dried at 60°C in air.

Synthesis of HAT-CN

HAT-CN has been synthesized according to a previously reported procedure.[281,322] After mixing of hexaketocyclohexane octahydrate (4 g, 12.6 mmol, Alfa Aesar, 99%) and diaminomaleonitrile (10.88 g, 100.8 mmol, TCI, >96.0%), the mixture was refluxed for 2 hours with 150 mL acetic acid (>99%). The resulting salt was then filtered and washed at least 3 times with 25 mL hot acetic acid. 60 mL of nitric acid (30%) was used to suspend black products and heated up to 100°C for 3 hours. When the reaction was finished, the solution was cooled down overnight in

ice water. After filtration, obtained particles were refluxed in acetonitrile (400 mL) for 2 hours to yield ~2.3 g of an orange product.

Synthesis of HAT/ZTC composites

HAT/ZTC composites were prepared by mixing HAT-CN and ZTC powder in inhibitor-free dimethylformamide (DMF) solvent. For HAT2 composites, 350 mg HAT-CN and 175 mg ZTC are mixed in 3.0 mL of DMF. For HAT4, 500 mg HAT-CN were mixed with 125 mg ZTC, for HAT6 600 mg HAT-CN were mixed with 100 mg ZTC and 600 mg HAT-CN were mixed with 75 mg ZTC to obtain HAT8. After 1 hour of sonication and stirring overnight, the dispersion was moved into a drying oven at 60°C under air atmosphere for 2 days. Afterwards, composites were moved to a vacuum oven at 60°C overnight. f-HAT composites have been obtained by the same drying procedure but without the first vacuum-free drying step. After DMF evaporation, mixtures were grinded well and carbonized in the tube furnace at different temperatures (550, 700, 1000°C) for 1 hour under Ar flow with a ramping rate of 4°C min^{-1}. Resulting composites are denoted as f- or s-HATX-Y, while X represents the mass ratio of HAT divided by ZTC and Y represents the HAT carbonization temperature. The pm-HAT-ZTC sample was prepared by grinding ZTC and HAT-1000 (HAT-CN carbonized at 1000°C). The mass ratio between HAT-1000 and ZTC was 6:1.

Synthesis of Cx-My composites

A sheet of ACF purchased from Kynol (Model number: Kynol ACC-5092-20, thickness = 0.55 mm, specific surface area ~1800 m^2 g^{-1}) was heated under air at 80°C for 30 minutes with a

ramping rate of 4^oC min^{-1}, and then to 420^oC for 30 minutes to generate oxygen-containing functional groups without severe degradation of carbon. All prepared carbon substrates were cut into rectangular shape with a mass of ~100 mg (~2 cm × 3 cm). For reaction with melamine, carbon substrates were loaded into an alumina boat into the quartz tube of a horizontal tubular IR oven. Melamine powder (99.95%, Sigma-Aldrich) was placed next to the carbon fibers on the side of the gas inlet. In the composites denoted as Cx-My, (x) stands for the mass of carbon fibers and (y) represents the mass of pristine melamine powder before the heat treatment. After covering the boat with aluminium foil, it was placed in the centre of IR oven. The oven was heated to 550^oC for 30 min with a high ramping rate of $10^{°}C$ sec^{-1} under continuous N_2 flow. The synthesized composites were collected after the oven cooled down to room temperature. The physically mixed pm-C1-M2 composite has been prepared by mixing activated carbon fibers (12.3 mg) and thermally treated (550^oC, 30 minutes in the IR oven with N_2 flow) melamine (11.0 mg). The corresponding nominal mass ratio between ACF and N-rich carbon in this physical mixture would correspond to the C1-M2 composite.

6.3.3 Characterization of materials

Characterization for f/s-HAT/ZTC composites

Scanning electron microscopy investigations of the composites has been carried out with a Leo Gemini 1550 (Zeiss) and EDX mapping was performed by X-Max (Oxford instruments) accessorized at the same instrument. The acceleration voltage was 3 kV for SEM images 10 kV for EDX mapping. TGA was collected using a thermo microbalance TG 209 F1 Libra (Netzsch) and analysed by the Proteus (8.0.0) software package. A platinum crucible was used for the

measurement in nitrogen or synthetic air (80:20 ratio of N_2:O_2) flow of 20 mL min^{-1} with a N_2 purge flow of 20 mL min^{-1} (heating rate = 10 °C min^{-1}). A Quadrasorb apparatus (Quantachrome Instruments) was used to measure N_2 and CO_2 isotherms. 20–40 mg of samples were placed into the 9 mm bulb cell and degassed overnight under vacuum at 135°C. N_2 physisorption was carried out at 77 K, and CO_2 physisorption was carried out at 273 K. V_{Total} was calculated from the nitrogen physisporption isotherms at p/p$_0$ = 0.95, and SSA was calculated utilizing the multi-point BET model (p/p$_0$ = 0.05 – 0.20). QSDFT was applied to the adsorption branches of the N_2 isotherms to calculate the pore distribution by assuming the carbon pores with a slit/cylindrical shape. X-ray diffraction patterns have been recorded by a D8 (BRUKER) in the 2 theta range from 10° to 60° with a scan rate of 0.05^o sec^{-1} and a Cu-Kα source (λ = 1.54 Å). Raman spectra were measured by a Witec Raman Microscope (532 nm of green laser at the power of 1.0 mW) and obtained bands are fitted by Gaussian functions.

Characterization for Cx-My composites

All SEM and EDX results have been collected on a Leo Gemini 1550 (Zeiss) and X-Max (Oxford instruments) accessorized at the same instrument. The applied acceleration voltage was 3 kV for SEM images, and 10 kV for EDX, respectively. EA has been measured by combustion analysis using a Vario Micro device. N_2 and CO_2 physisorption measurements have been carried out by using a Quadrasorb apparatus. ~50 mg of samples were used for all measurements and degassed overnight under vacuum at 180°C. N_2 and CO_2 isotherms have been measured at two different temperatures (77 K and 298 K for N_2, 273 K and 298 K for CO_2). V_{Total} was calculated from the nitrogen physisorption isotherms (77 K) at p/p$_0$ = 0.99, while SSA has been determined

based on the multi-point BET model (p/p$_0$ = 0.02–0.15). QSDFT was utilized with the adsorption curves of N$_2$ isotherms (77 K) to calculate pore distributions by assuming carbon surfaces with mixed slit/cylindrical pore geometry. V$_{Ultramicro}$ has been calculated based on CO$_2$ physisorption by applying NLDFT. Water physisorption has been measured at 298 K on a Quantachrome Autosorb IQ instrument. Before the measurements, ~50 mg of each sample were degassed first under vacuum at 150 $^{\circ}$C for 20 hours.

f/s-HAT/ZTC composite electrode fabrication and electrochemical measurements

Before the electrode fabrication, Cu foil (25 µm) was cleaned by acetone and cut into disks of 10 mm in diameter. For the preparation of the electrode ink, 16 mg of active materials, 2 mg of carbon black (Super-P, Alfa Aesar), and 2 mg of sodium carboxymethyl cellulose binder (Sigma, average Mw ~250000) were mixed in 1.0 mL of Milli-Q water. After making the ink, it was sonicated 1 hour and stirred overnight. 30 µL of the final ink was dropped onto the Cu disk, dried at 60°C in an open oven overnight, and stored in a vacuum oven at 60°C. The areal loading of the fabricated electrode was between 0.6 – 1.0 mg cm^{-2}. EIS and charge-discharge half-cell tests were measured with a MPG-2 potentiostat/galvanostat (BioLogic). For all electrochemical cell tests, a Swagelok cell design was adopted. The cell assembly was carried out in an Ar gas filled glove box (H$_2$O and O$_2$ level < 0.5 ppm) with a Li metal cathode (Sigma, 10 mm disk), Celgard 2320 separator (13 mm disk) and 100 µL of 1.0 M LiPF$_6$ dissolved in 1:1 (v/v) EC/DEC electrolyte. The EIS spectra were measured at open circuit voltage with a range from 1.0 mHz to 20 kHz at an amplitude 10 mV. Galvanostatic charge-discharge LIC tests were performed between 0.1 – 10 A g^{-1} with 0.002 – 3.0 V cutoff voltage at room temperature.

Cx-My composite electrode fabrication and electrochemical measurements

Cx-My composites were cut into circular shape (diameter = 10 mm), followed by drying at 60°C under vacuum overnight. Prepared Cx-My electrodes were assembled into a Swagelok-based half-cell design into an Ar filled glove box (H_2O and O_2 levels below 0.5 ppm) with Li metal (diameter = 10 mm, Sigma) as the counter electrode and Celgard 2320 as separator (diameter = 13 mm). 150 µL of 1.0 M $LiPF_6$ dissolved in EC/DEC in 1:1 (v/v) ratio was used as electrolyte. All electrochemical cell tests were conducted with the same half-cell design on a MPG-2 potentiostat/galvanostat (BioLogic). EIS was measured at 0 V vs. open circuit with 10 mV of amplitude and 1.0 mHz to 20 kHz of frequency range. Galvanostatic charge-discharge tests for LICs have been performed between 0.002 and 2.5 V as a cutoff voltage at room temperature. C-rates are calculated based on theoretical capacity of graphite (372 mAh h^{-1}).

.

6.4 Supplementary information

6.4.1 Supplementary tables

Table S1. Carbon and nitrogen weight content of ZTC, f-HATX-Y, HAT-1000, and pm-HAT-ZTC determined by EA.

Sample	C (wt%)	N (wt%)
ZTC	78.1	0.40
f-HAT2-550	67.6	14.1
f-HAT2-700	70.7	7.9
f-HAT2-1000	77.5	1.4
f-HAT4-550	58.8	21.9
f-HAT4-700	67.3	14.5
f-HAT4-1000	87.4	3.4
f-HAT6-550	54.7	27.5
f-HAT6-700	59.2	22.6
f-HAT6-1000	85.8	5.1
f-HAT8-1000	77.5	6.0
HAT-1000 only	81.9	5.6
pm-HAT-ZTC	69.5	5.0

Table S2. Total pore volume and SSA of ZTC, s/f-HATX-Y samples, HAT-1000, and pm-HAT-ZTC from N_2 physisorption measurements at 77 K. The pore volume was calculated at a relative pressure of $p/p_0 = 0.95$ (adsorption curve). SSA was calculated by utilizing the multi-point BET model in $p/p_0 = 0.05 – 0.20$ range.

| Sample	Total Pore Volume $(cm^3 g^{-1})$	BET SSA $(m^2 g^{-1})$
ZTC	2.6	1520
s-HAT2-550	1.4	666
s-HAT2-700	1.8	998
s-HAT2-1000	2.2	1320
f-HAT4-550	0.7	504
f-HAT4-700	1.1	1030
f-HAT4-1000	1.6	1340
s-HAT4-550	0.6	470
s-HAT4-700	0.8	749
s-HAT4-1000	1.2	1150
f-HAT6-550	0.6	407
f-HAT6-700	1.0	779
f-HAT6-1000	1.7	1140
s-HAT6-550	0.5	495
s-HAT6-700	0.7	669
s-HAT6-1000	1.2	1060
s-HAT8-1000	0.6	657
HAT-1000 only	0.4	733
pm-HAT-ZTC	0.8	838

Table S3. Weight content of carbon and nitrogen in pristine carbon fibers, ACF, melamine treated at 550°C (Mel-550), Cx-My composites, and physically mixed pm-C1-M2 measured by EA.

Sample	C (wt%)	N (wt%)
Pristine	98.8	0.31
ACF	93.9	0.26
Mel-550	55.9	34.3
C4-M1	94.7	2.62
C2-M1	91.5	5.11
C1-M1	64.6	26.8
C1-M2	62.4	27.9
C1-M4	50.7	41.1
pm-C1-M2	86.8	8.27

**Table S4.** Total pore volume, SSA calculated by BET, and ultra-micropore volume of Cx-My and reference materials.

| Sample	Total Pore Volume ($cm^3 g^{-1}$)	BET SSA ($m^2 g^{-1}$)	Ultra-micropore Volume ($cm^3 g^{-1}$)
ACF	0.86	1850	0.43
Mel-550	0.023	20	0.002
C4-M1	0.70	1540	0.37
C2-M1	0.44	958	0.27
C1-M1	0.26	542	0.15
C1-M2	0.012	13	0.030
C1-M4	0.0065	3	0.006
pm-C1-M2	0.43	923	0.23

6.4.2 Supplementary figures
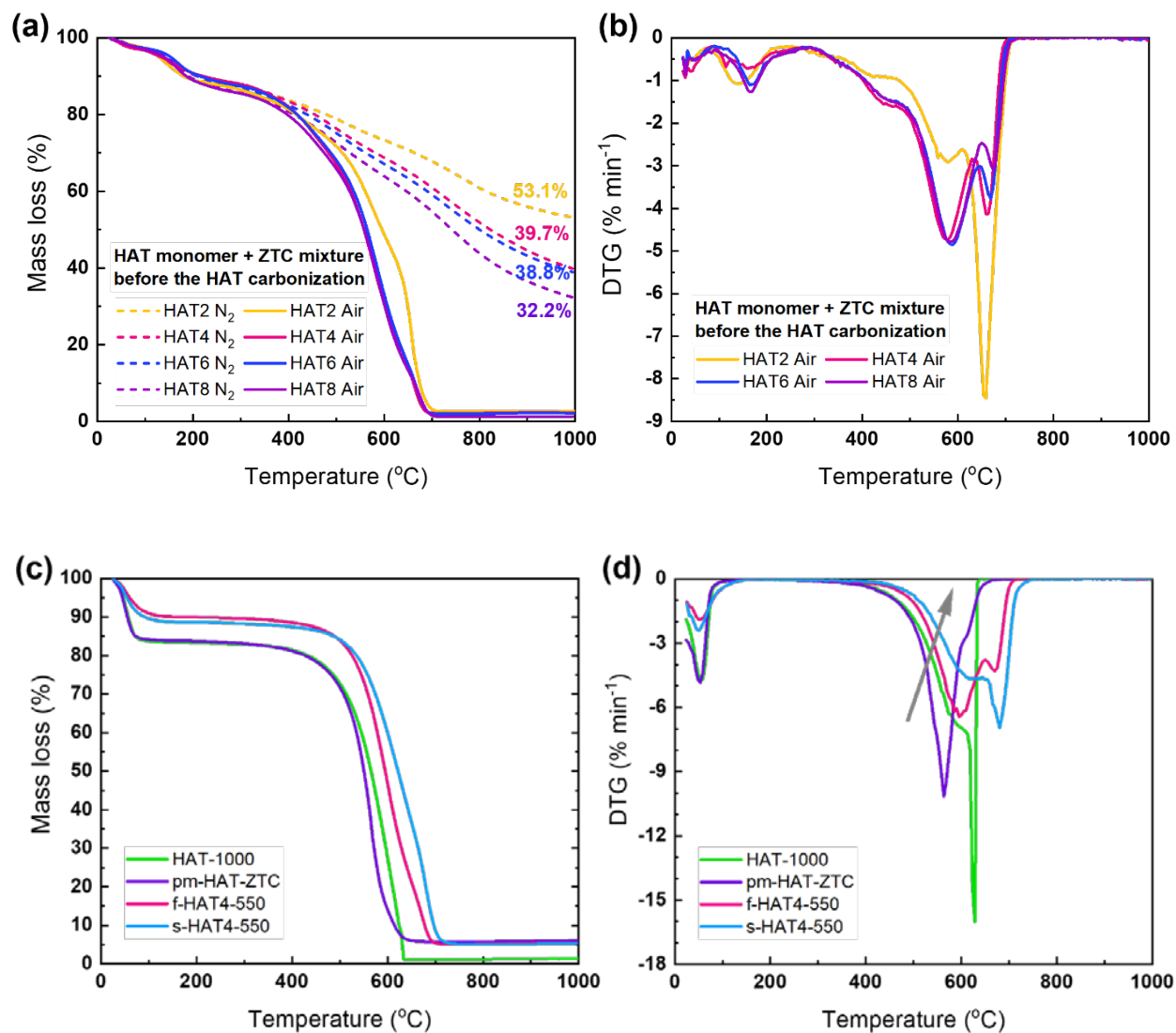
Figure S1. (a) TGA curves under N_2 and synthetic air and (b) first derivatives of the measurements under synthetic air of the mixtures between different ratio of uncondensed HAT-CN and ZTC as well as (c) TGA curves under synthetic air and (d) corresponding first derivatives of different composite materials.
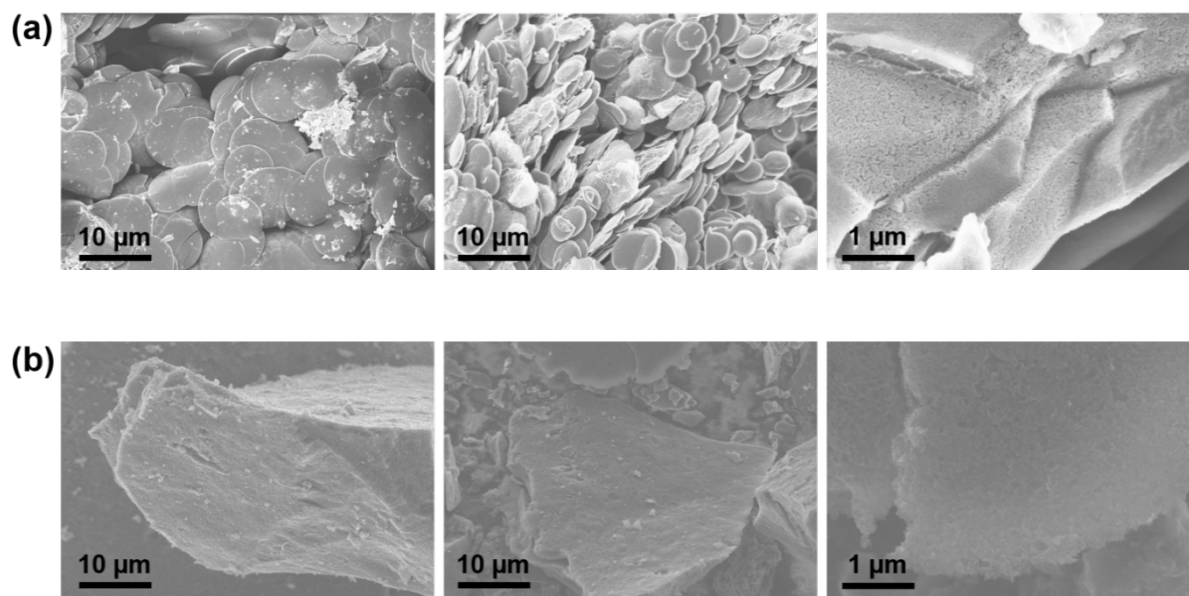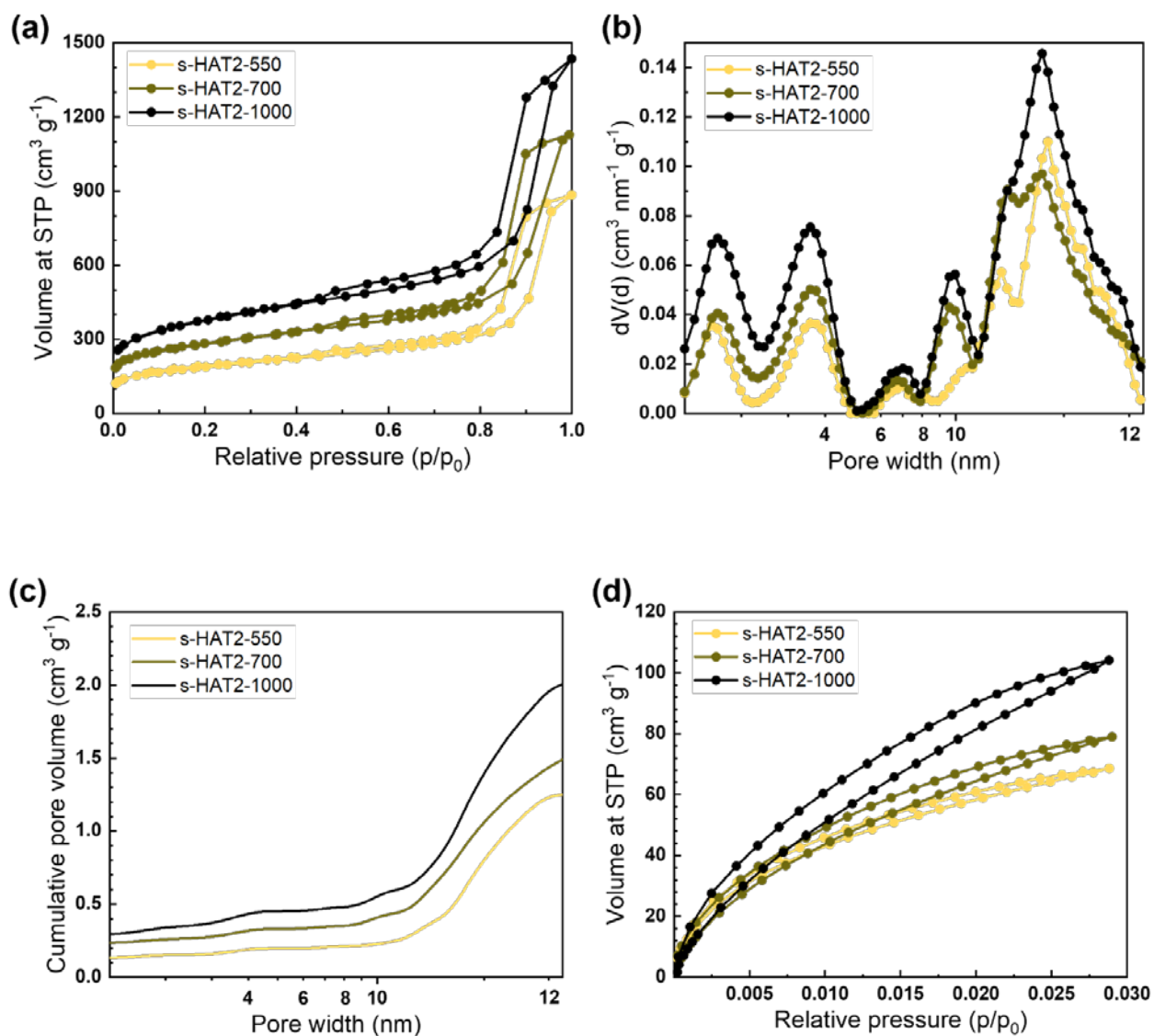
**Figure S2.** SEM images of (a) HAT-1000 and (b) ZTC carbon.
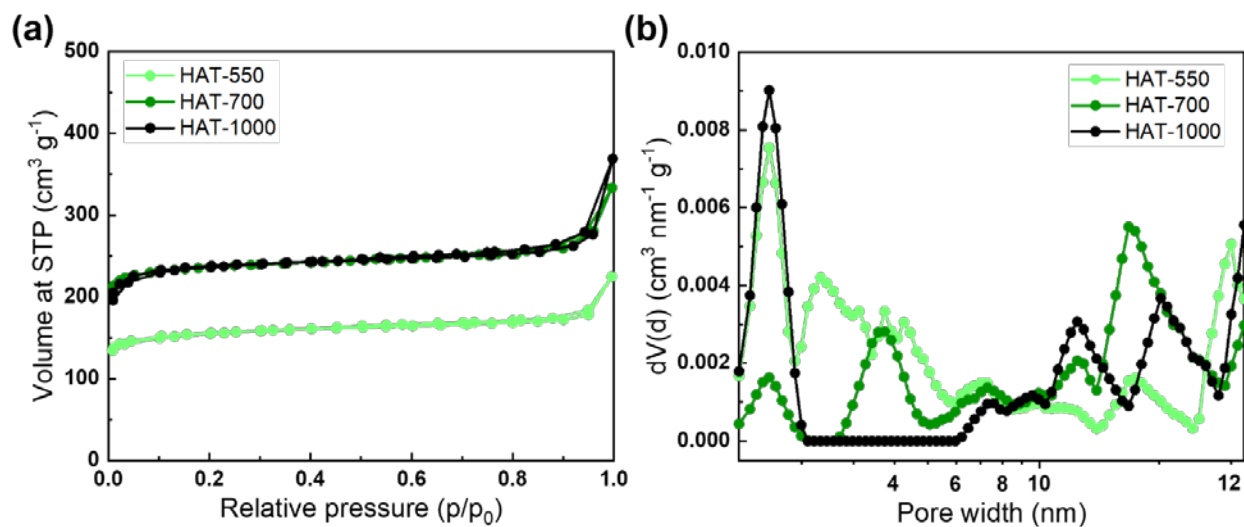
Figure S3. (a) N_2 physisorption isotherms (77 K) of HAT-derived carbon without ZTC after condensation at different temperatures and (b) corresponding pore distribution curves calculated using QSDFT.
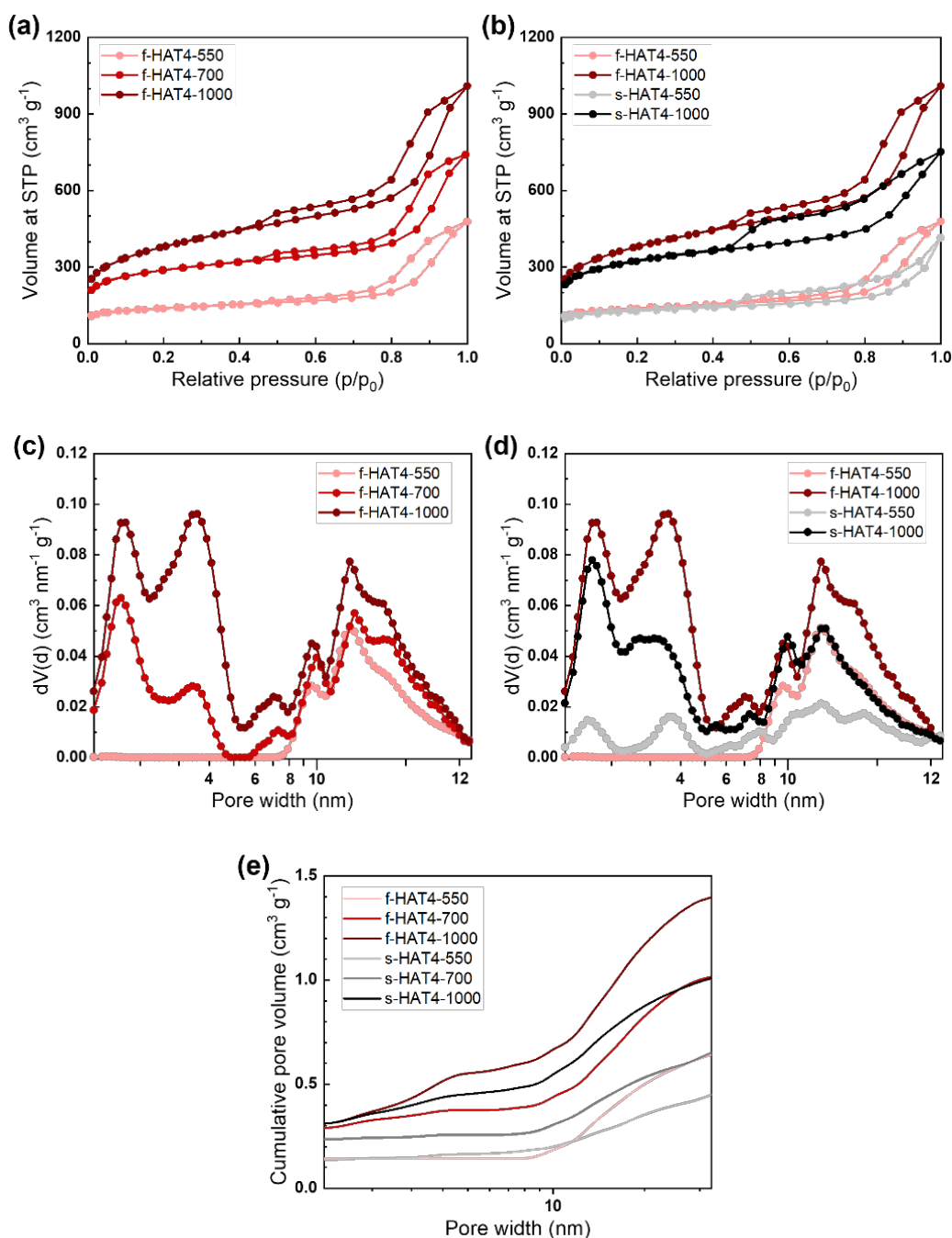
Figure S4. (a) N_2 physisorption isotherms (77 K) of s-HAT2 composites with different condensation temperature, corresponding (b) differential and (c) cumulative QSDFT pore distribution curves, and (d) CO_2 isotherms (273 K).
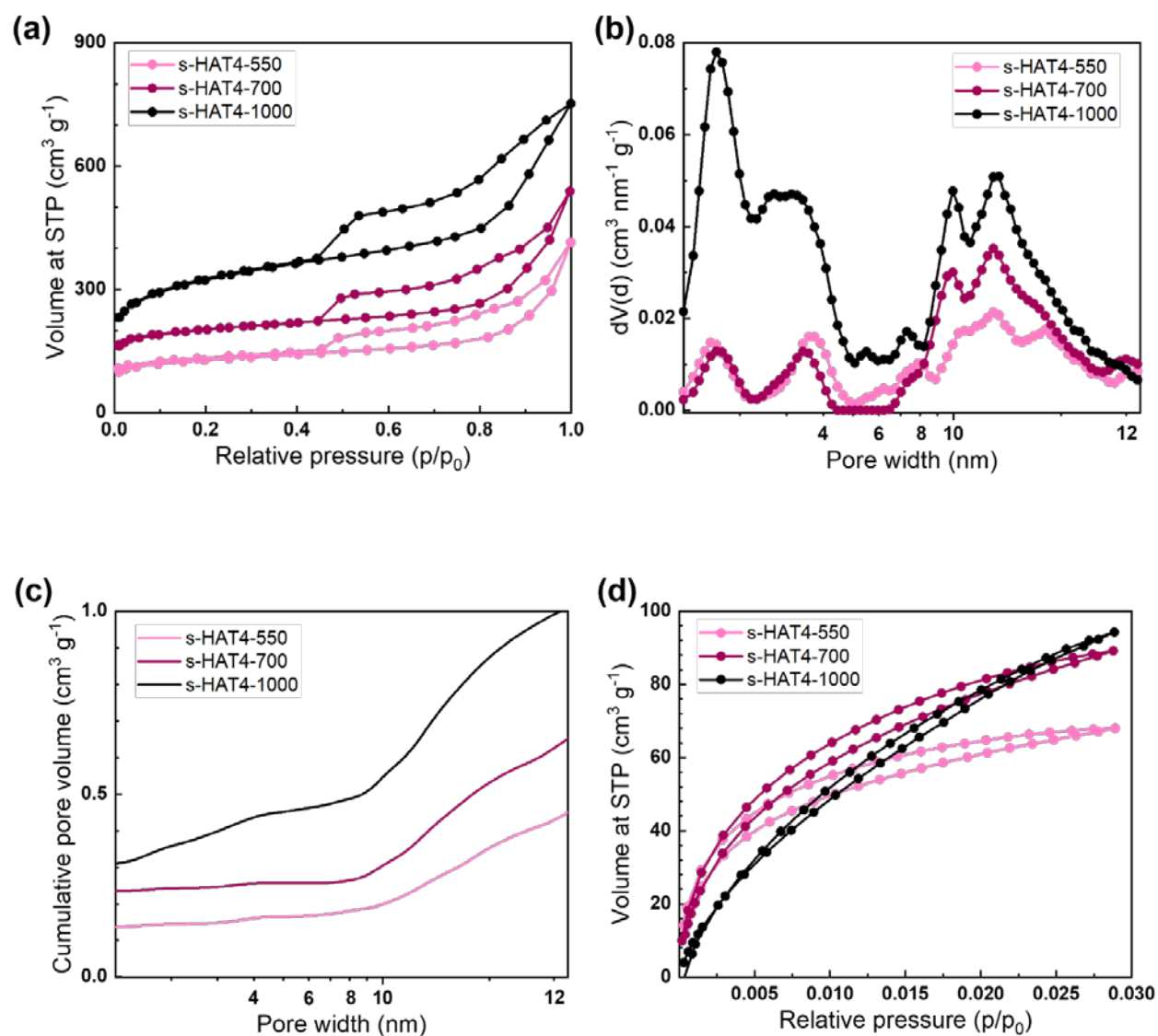
Figure S5. (a) N_2 physisorption isotherms (77 K) of s-HAT4 composites with different condensation temperature, corresponding (b) differential and (c) cumulative QSDFT pore distribution curves, and (d) CO_2 isotherms (273 K).
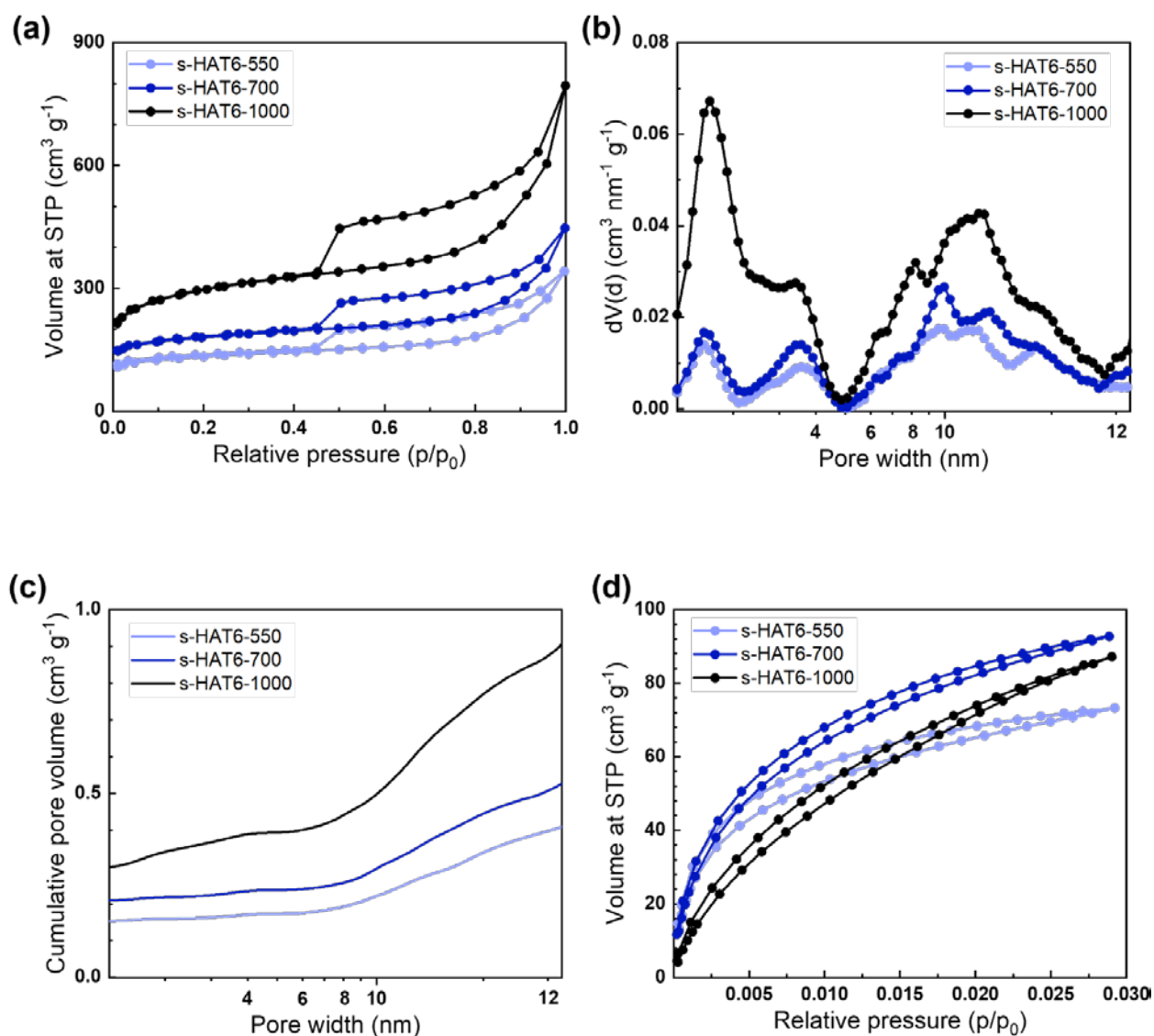
Figure S6. (a) N_2 physisorption isotherms (77 K) of s-HAT6 composites with different condensation temperature, corresponding (b) differential and (c) cumulative QSDFT pore distribution curves, and (d) CO_2 isotherms (273 K).
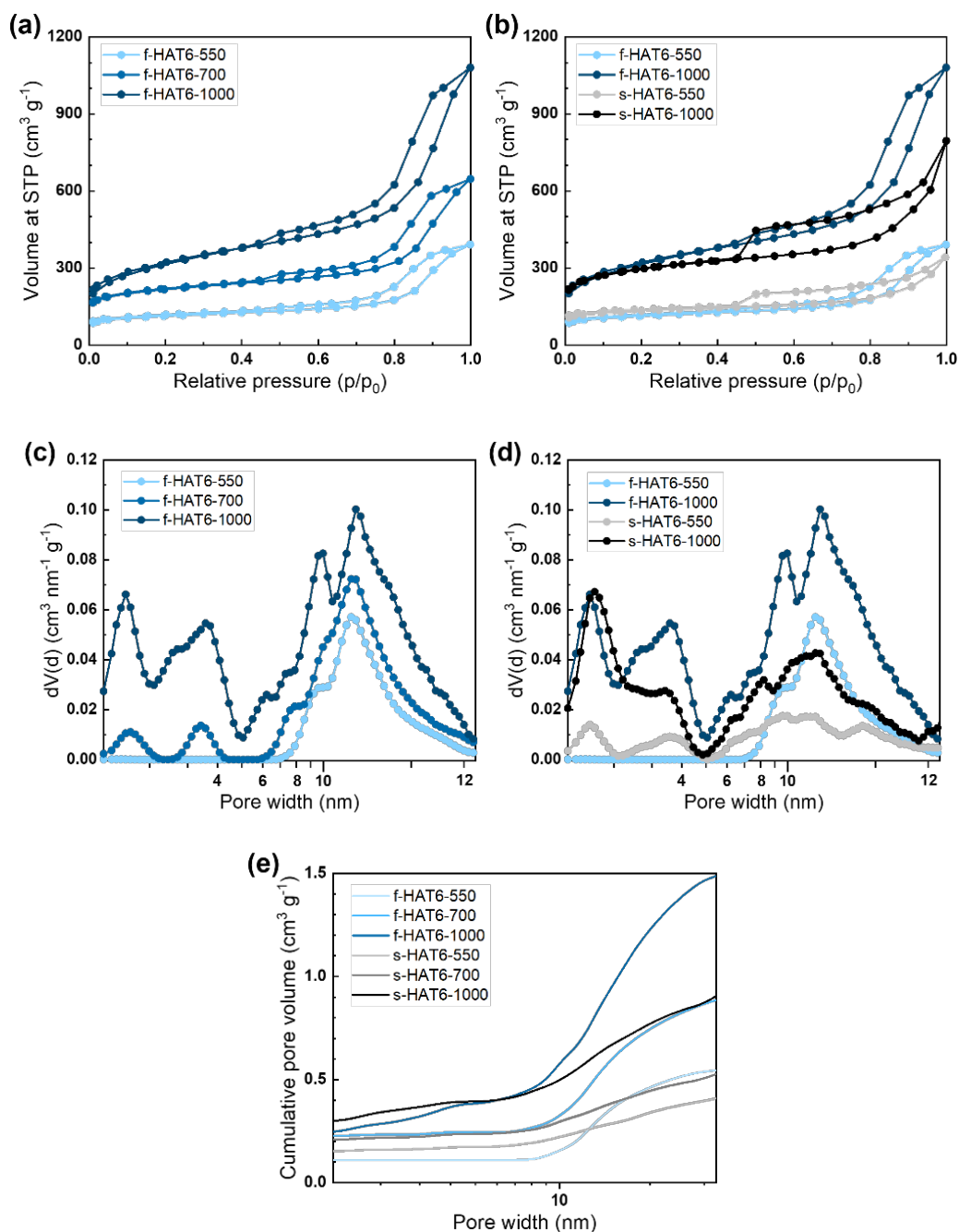
Figure S7. (a) N_2 physisorption isotherms (77 K) of f-HAT4 composites with different condensation temperature, (b) comparison of the isotherms of f-HAT4 and s-HAT4 composites after condensation at 550 and 1000°C as well as corresponding (c) and (d) differential and (e) cumulative QSDFT pore distributions.
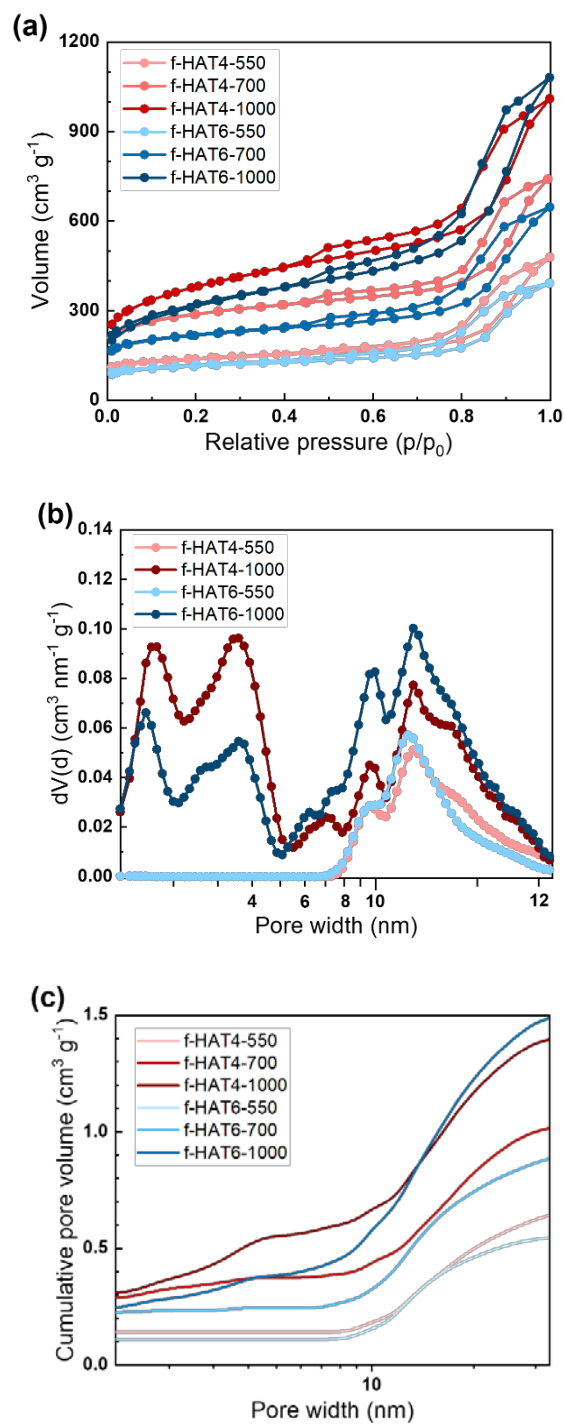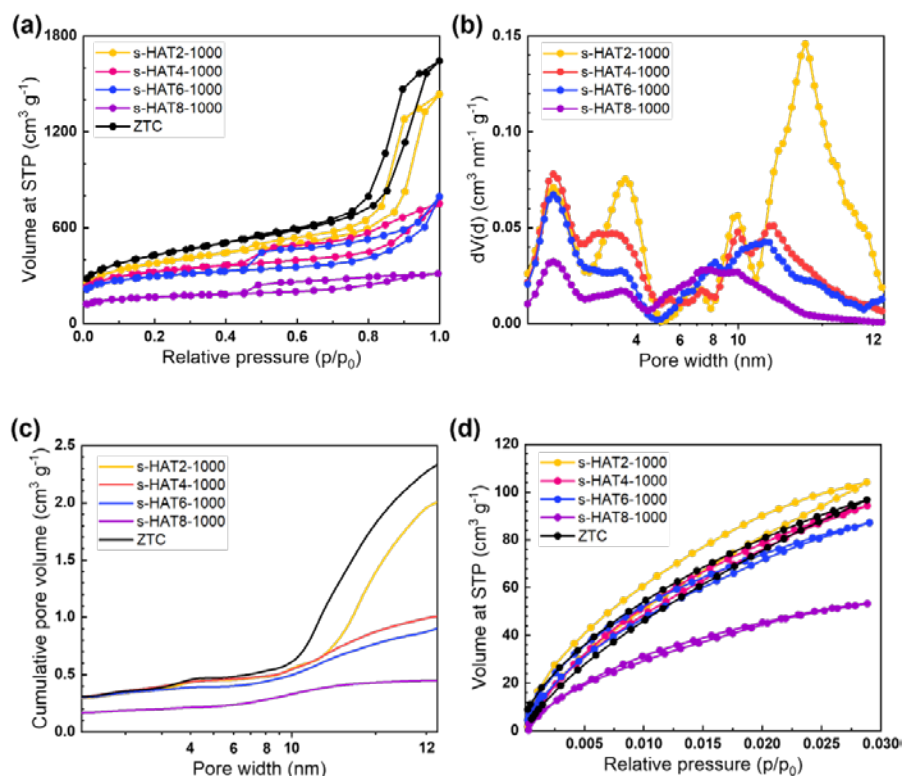
Figure S8. (a) N$_2$ physisorption isotherms (77 K) of f-HAT6 composites with different condensation temperature, (b) comparison of the isotherms of f-HAT6 and s-HAT6 composites after condensation at 550 and 1000°C as well as corresponding (c) and (d) differential and e) cumulative QSDFT pore distributions.

Figure S9. (a) N_2 physisorption isotherms (77 K) of f-HAT4 and f-HAT6 composites with different condensation temperature with corresponding (b) differential and (c) cumulative QSDFT pore distribution curves.

Figure S10. (a) N_2 physisorption isotherms (77 K) of s-HAT composites condensed at 1000^oC with different loadings of HAT, corresponding (b) differential and (c) cumulative QSDFT pore distribution curves, and (d) CO_2 isotherms (273 K).
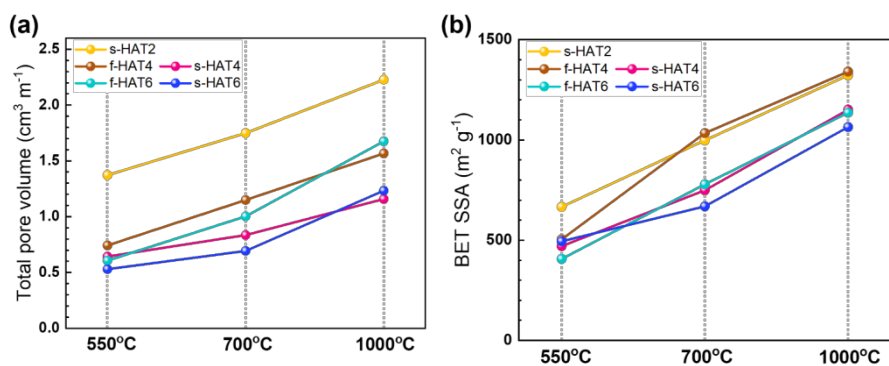
Figure S11. Summary of (a) total pore volume and (b) BET specific surface of area of all HAT/ZTC composites.
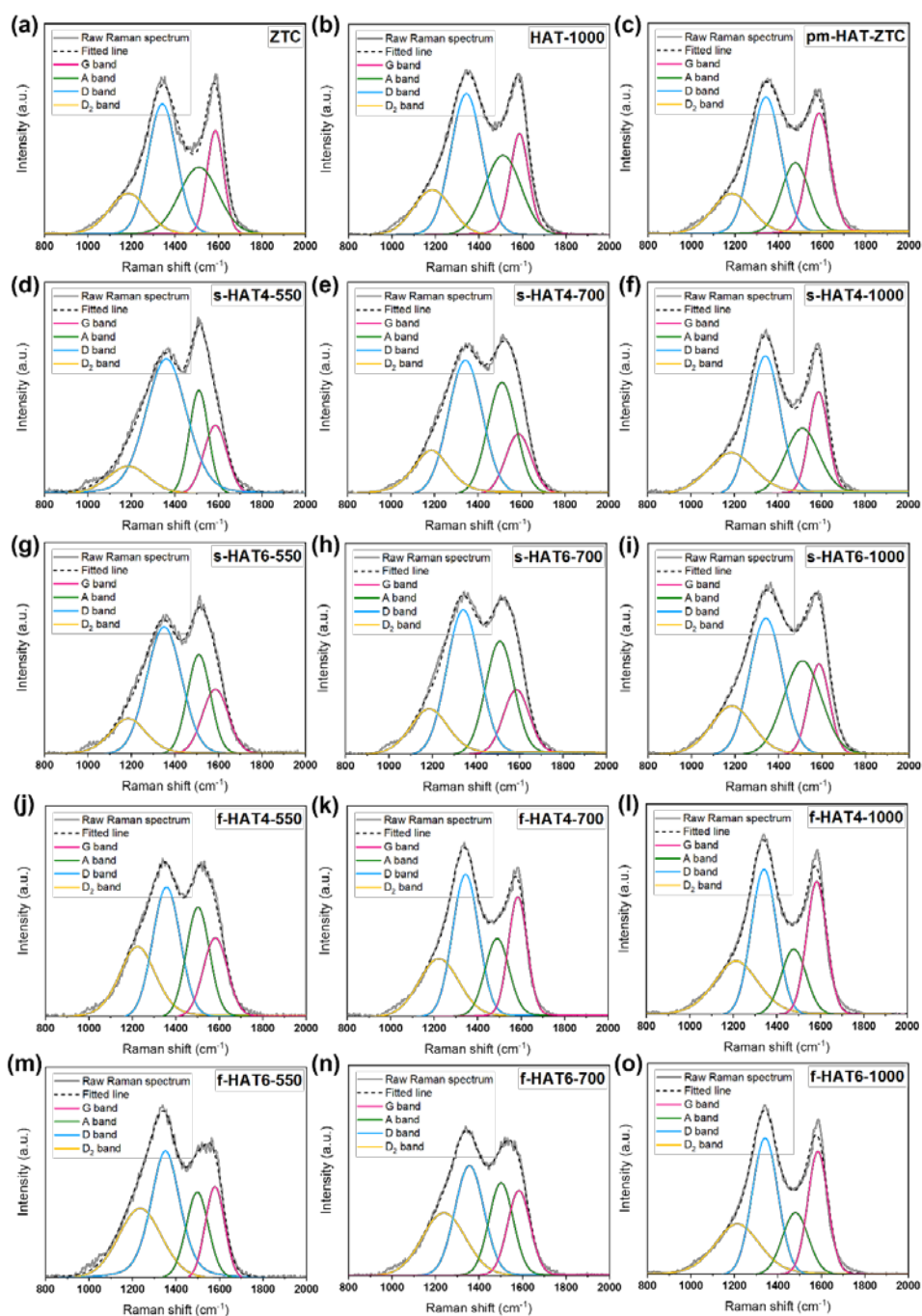
Figure S12. Raw Raman spectra of each composite and fitted curves by D, G, A, and D_2 bands with Gaussian functions. Each spectrum was measured with 532 nm of green laser with 1.0 mW of power and 100 times of accumulation.
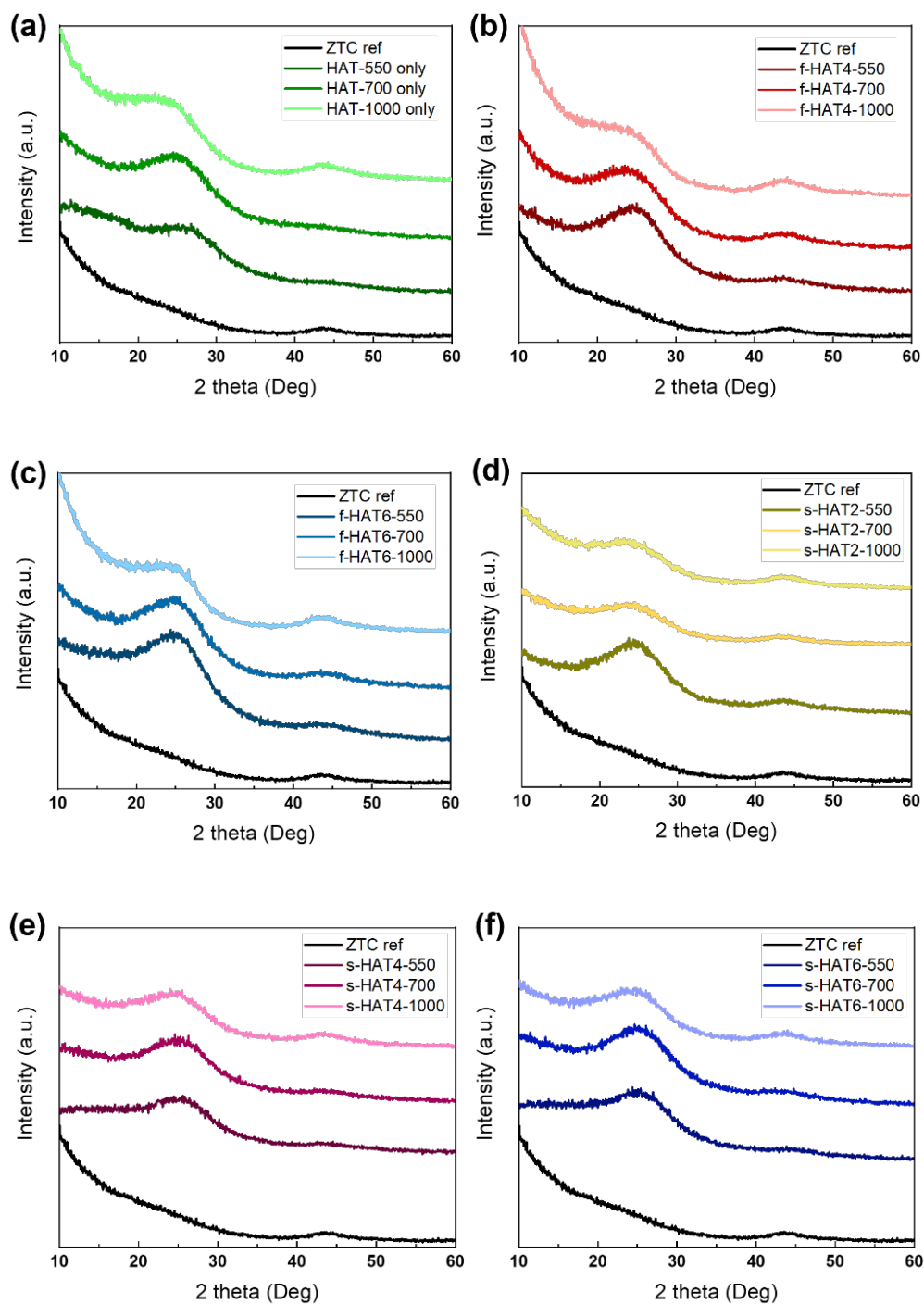
Figure S13. XRD patterns of (a) HAT only samples, (b) f-HAT4-Y, (c) f-HAT6-Y, (d) s-HAT2-Y, (e) s-HAT4-Y, and (f) s-HAT6-Y composites.
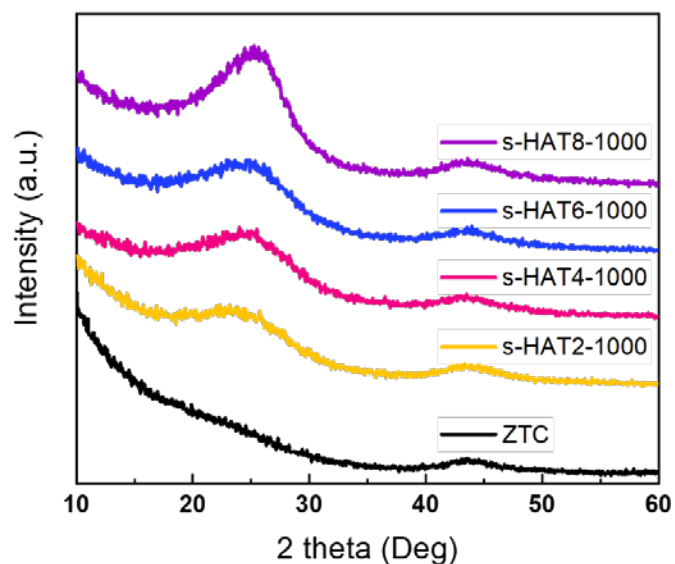
Figure S14. XRD patterns of s-HATX-1000 composites with different loading of HAT.
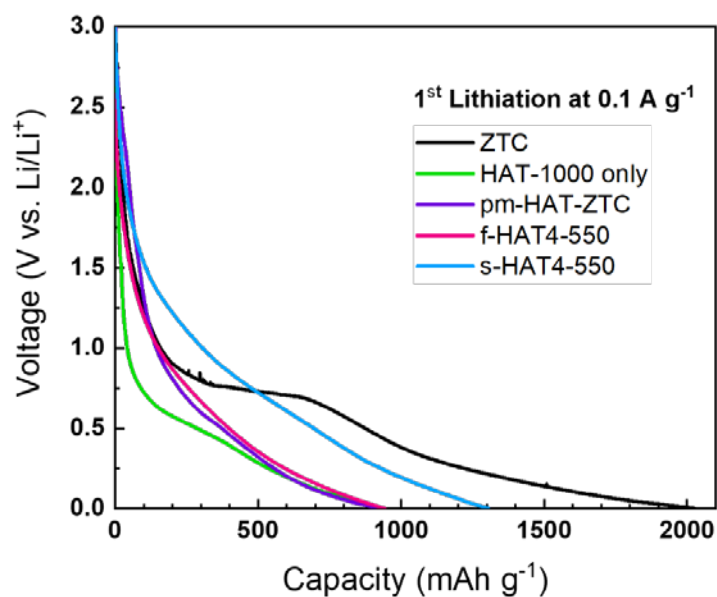
Figure S15. Capacity of the first lithiation cycle depending on different HAT/ZTC composites. This capacity of the first lithiation contains both reversible and irreversible capacity, thus the irreversible capacity loss indicated in Figure 27(b) is calculated by the difference between this capacity and the reversible capacity of the second cycle.
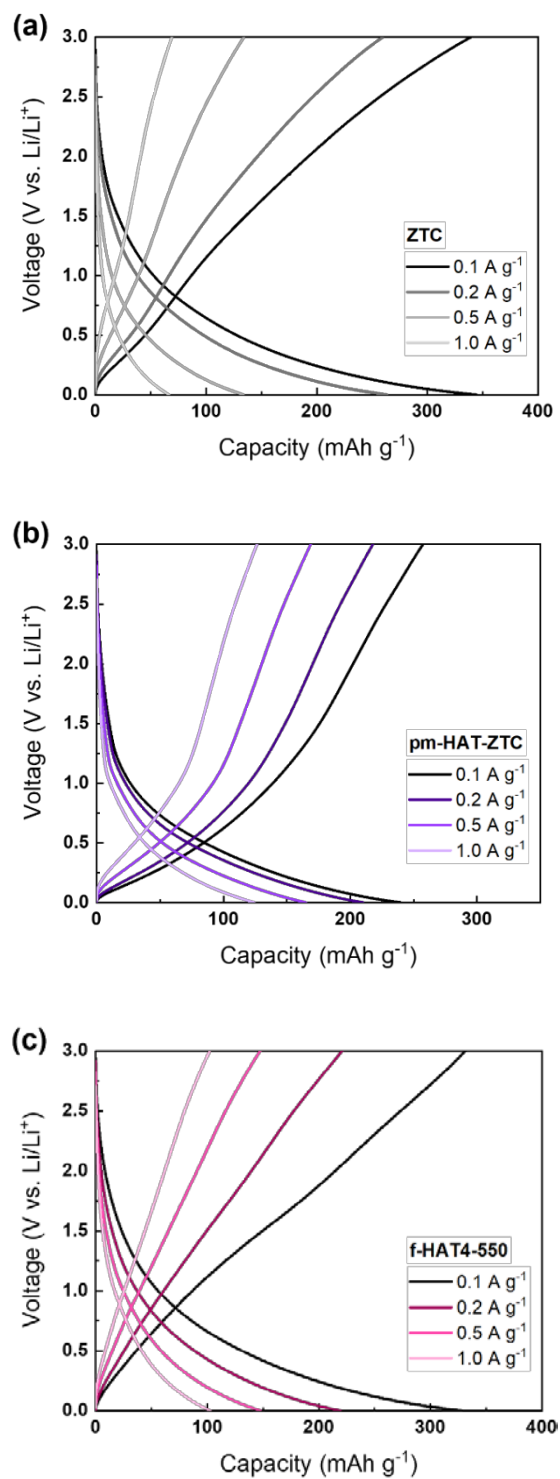
Figure S16. Charge/discharge curves of (a) ZTC, (b) pm-HAT-ZTC, and (c) f-HAT4-550 at 0.1, 0.2, 0.5, and 1.0 A g^{-1}, respectively.
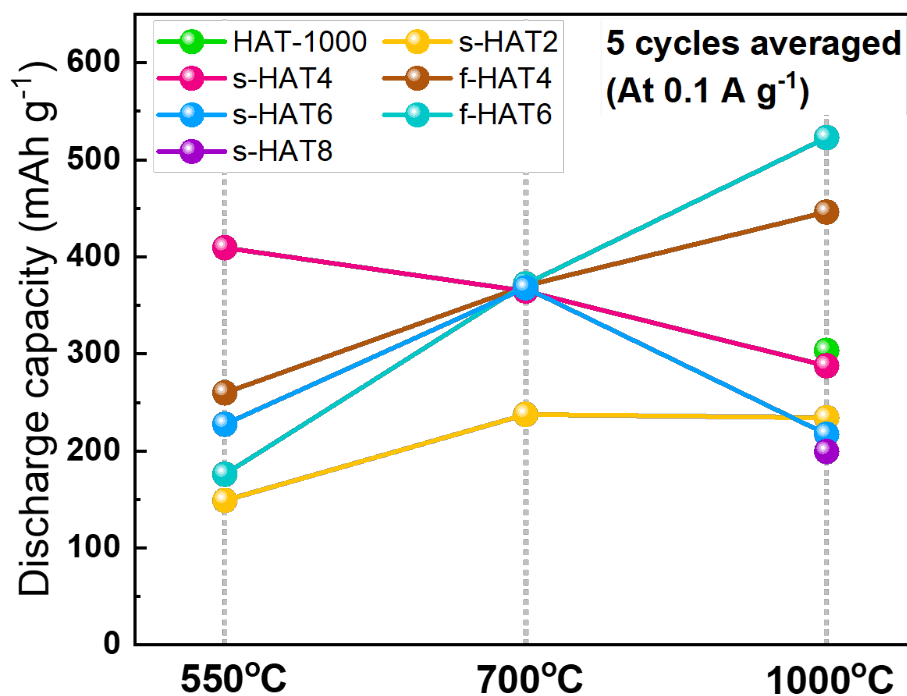
Figure S17. Comparison of discharge capacity (5 cycles averaged data at 0.1 A g^{-1}) of f/s-HATX-Y composites with different condensation temperatures.
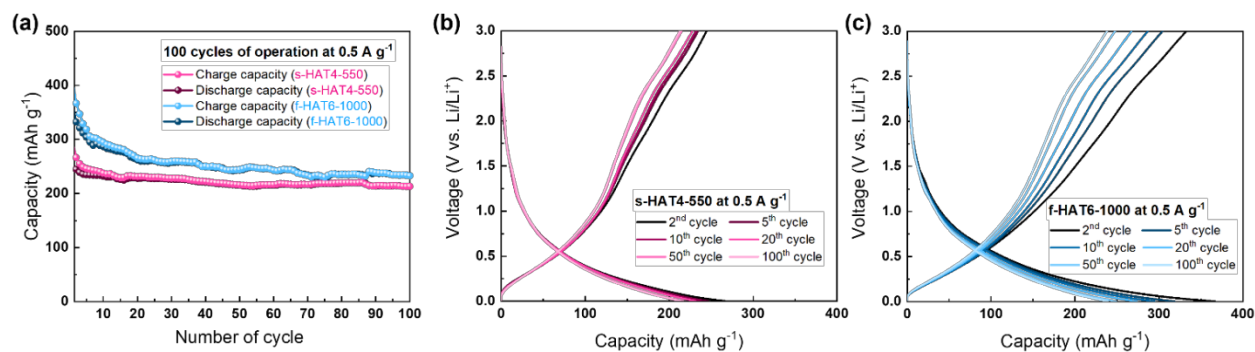
Figure S18. (a) 100 cycles of long-term stability test of s-HAT4-550 and f-HAT6-1000 at 0.5 A g^{-1} of rate, and charge/discharge curves of (b) s-HAT4-550 and (c) f-HAT6-1000 composites at 2nd, 5th, 10th, 20th, 50th, 100th cycle, respectively.
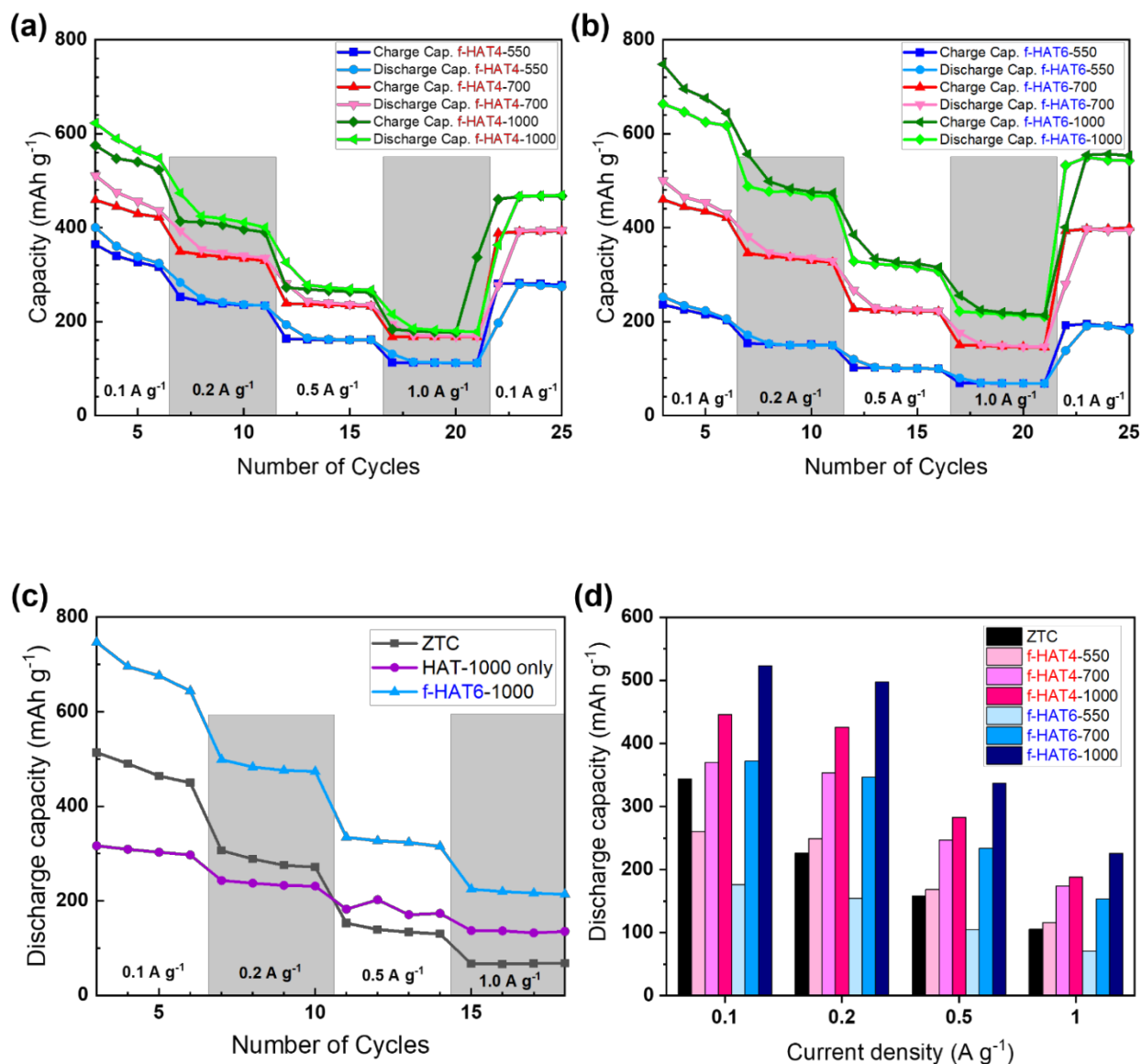
Figure S19. Charge/discharge capacity comparison of f-HAT composite electrodes depending on HAT ratio ((a) HAT4 and (b) HAT6) and the temperature. Among f-HAT composite materials, f-HAT6-1000 shows the best performance ((c), (d)) compared to other composites, ZTC, and HAT-1000 only electrode (523, 498, 337, 226 mAh g^{-1} of discharge capacity at 0.1, 0.2, 0.5, 1.0 A g^{-1} of current rate, respectively).

Point	C (wt%)	N (wt%)	O (wt%)
1	69.9	26.7	3.3
2	66.7	29.9	3.2
3	72.3	12.5	12.1
4	80.5	13.9	5.4
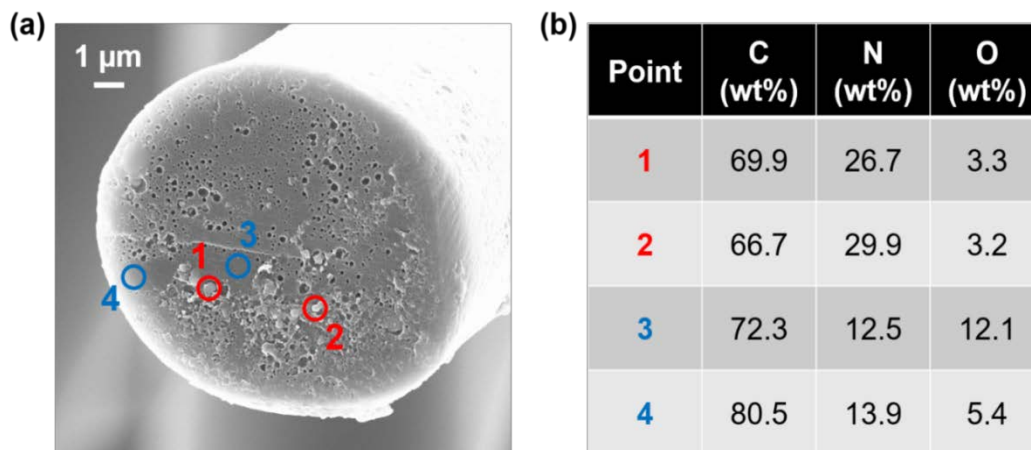
Figure S20. (a) SEM image and (b) point EDX results from the cross-section of C1-M2.
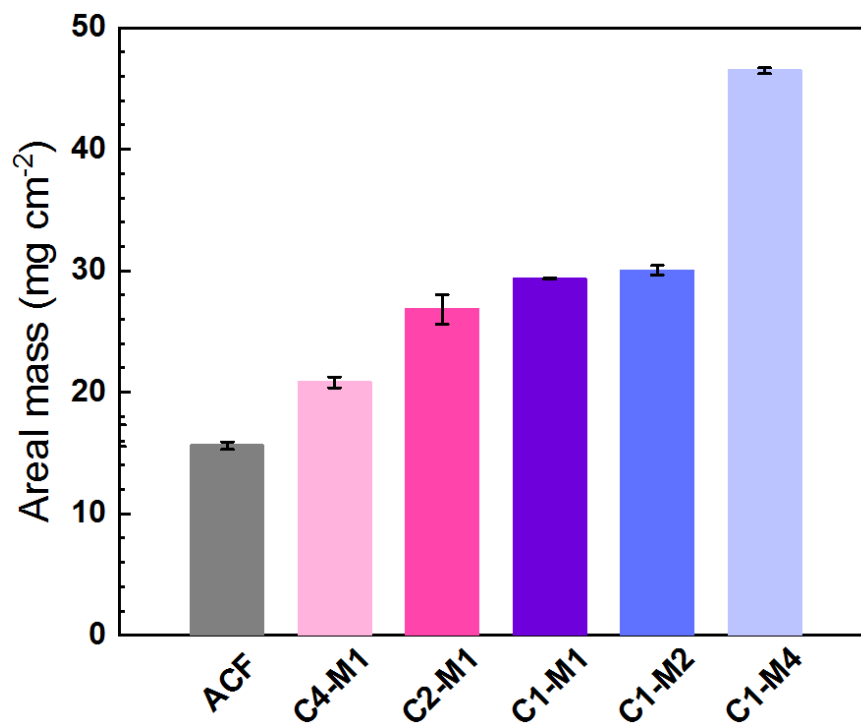
Figure S21. Areal mass (mg cm^{-2}) of ACF, and Cx-My composites depending on loading amount of melamine.

Figure S22. Optical images of Cx-My electrodes. Overloading can be clearly seen in case of the C1-M4, showing bright yellow color on the surface.
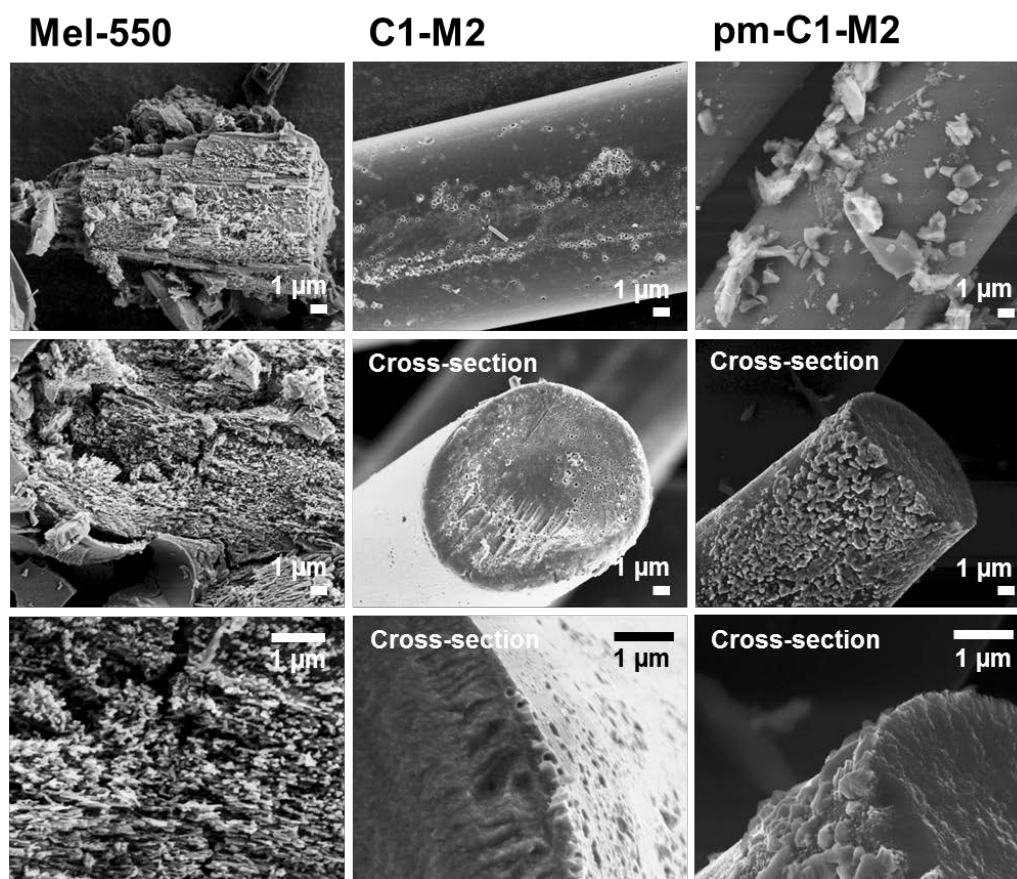
Figure S23. SEM images of 550°C heat-treated melamine (Mel-550), C1-M2, and a physical mixture of melamine and activated carbon fibers (pm-C1-M2).
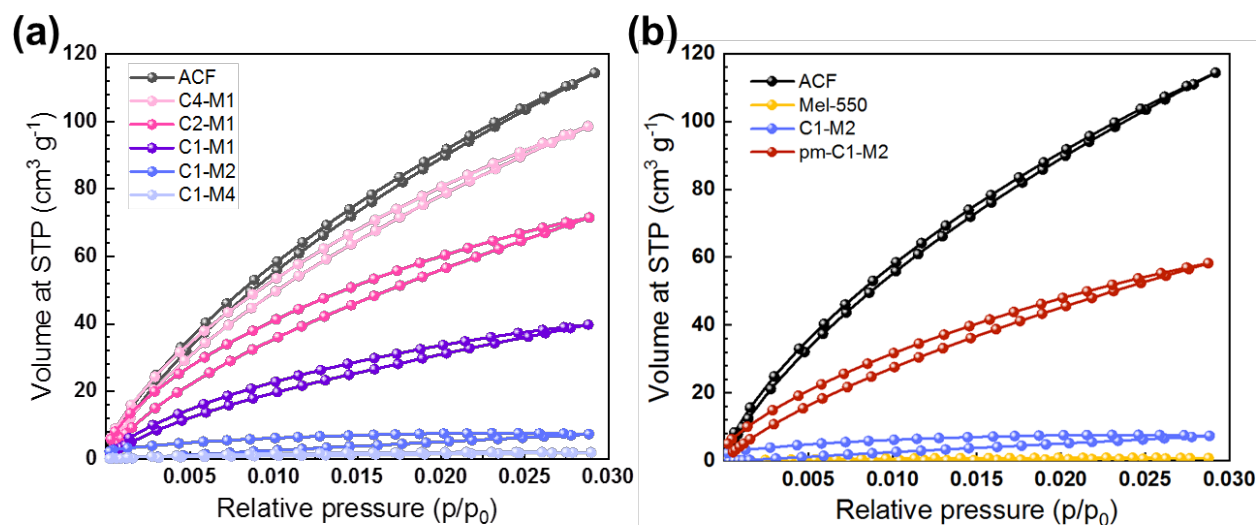
Figure S24. CO_2 physisorption isotherms (273 K) of (a) Cx-My mixtures prepared with different amounts of melamine and (b) of C1-M2 in comparison with different reference materials.
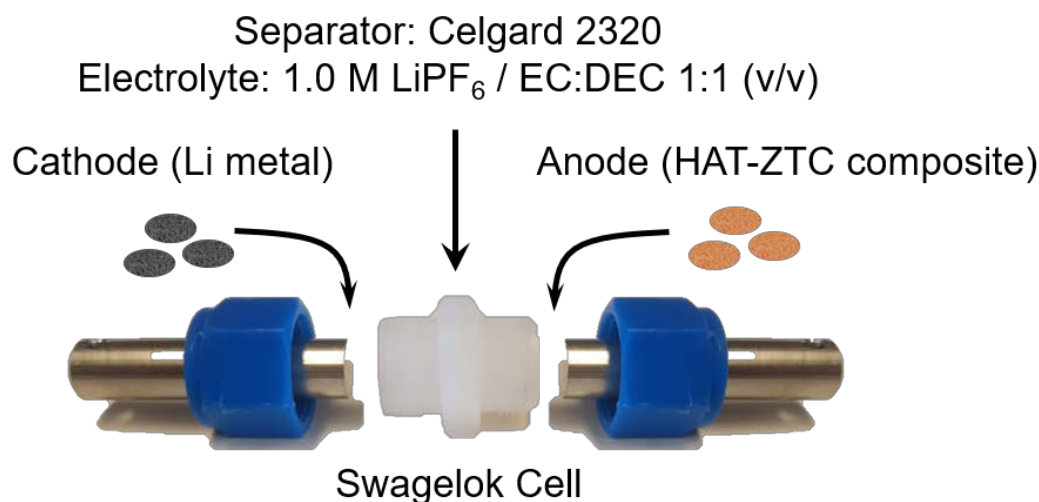
Figure S25. Swagelok cell design for Li-ion capacitor cell test. At the cathode side, disk-shaped Li metal is located, while HAT/ZTC composite loaded on Cu foil is located at the anode side. For the separator and electrolyte, Celgard 2320 porous membrane and 100 μL of 1.0 M $LiPF_6$ in EC/DEC (v:v = 1:1) are utilized, respectively.
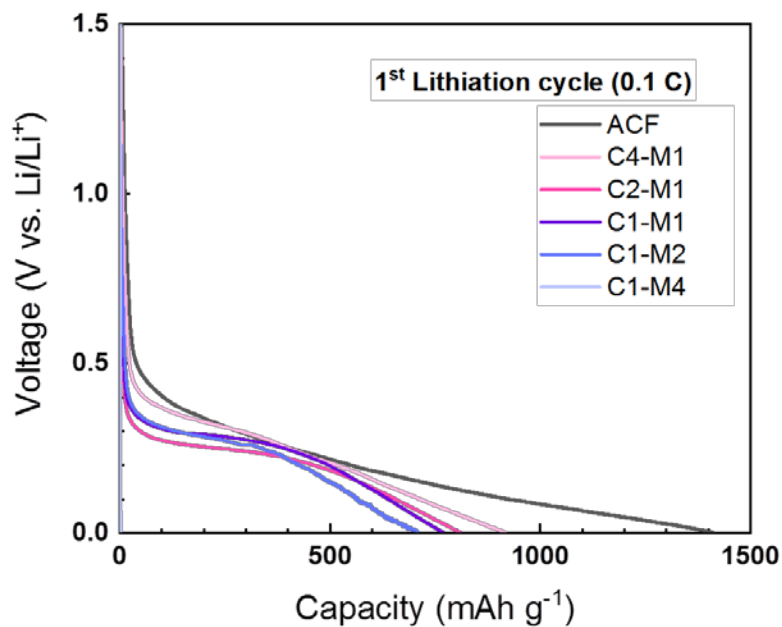
Figure S26. Galvanostatic voltage profiles of first lithiation cycles of ACF and Cx-My electrodes.
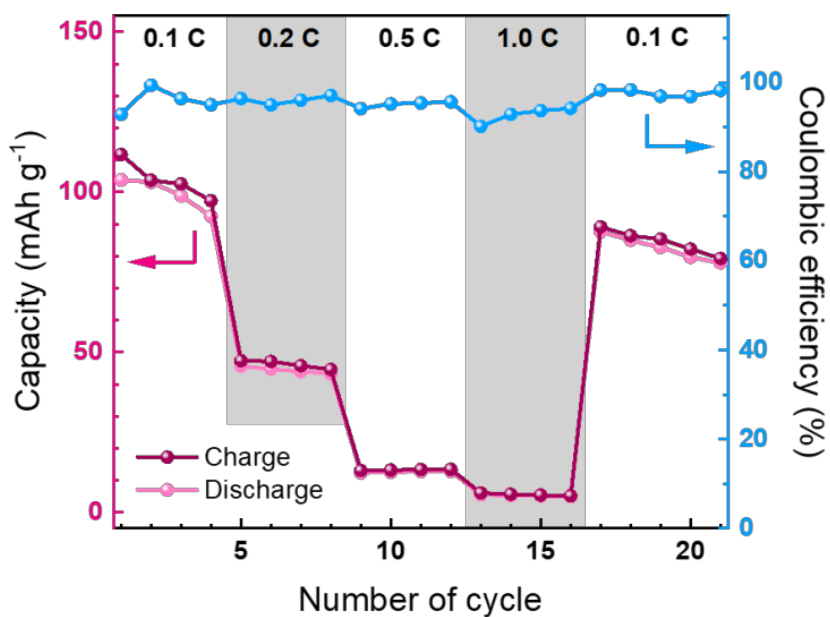
Figure S27. Rate capability test of C1-M2 from 0.1 to 1.0 C.
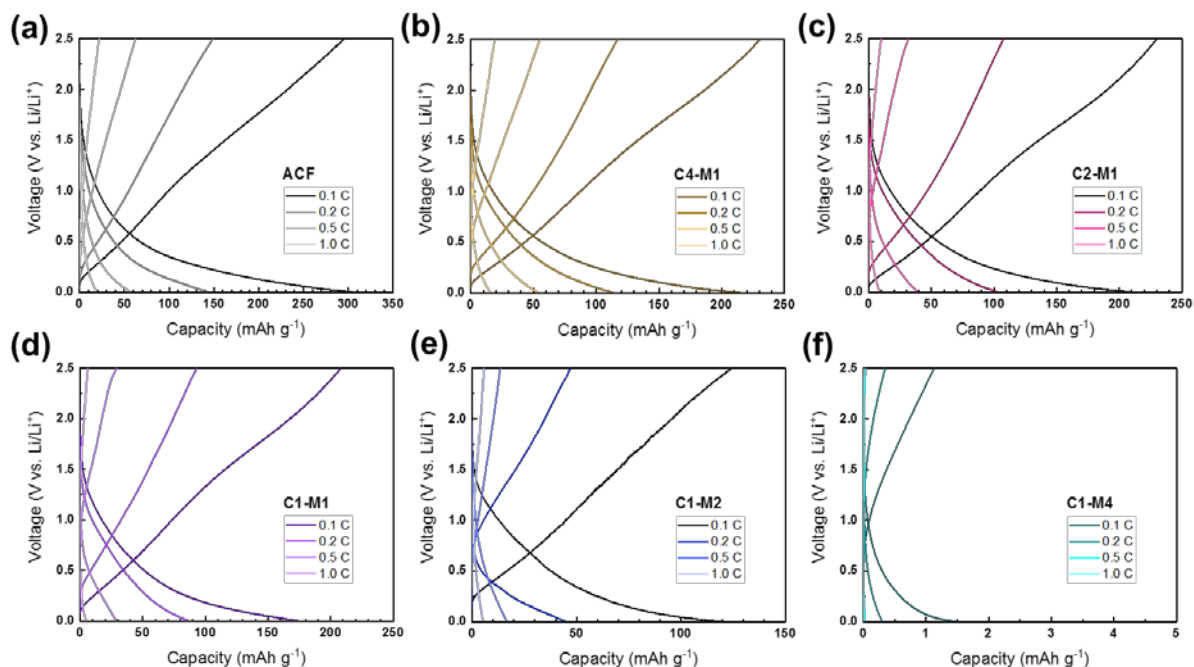
Figure S28. Galvanostatic charge-discharge profiles of (a) ACF, (b) C4-M1, (c) C2-M1, (d) C1-M1, (e) C1-M2, and (f) C1-M4 at 0.1, 0.2, 0.5, 1.0 C, respectively.
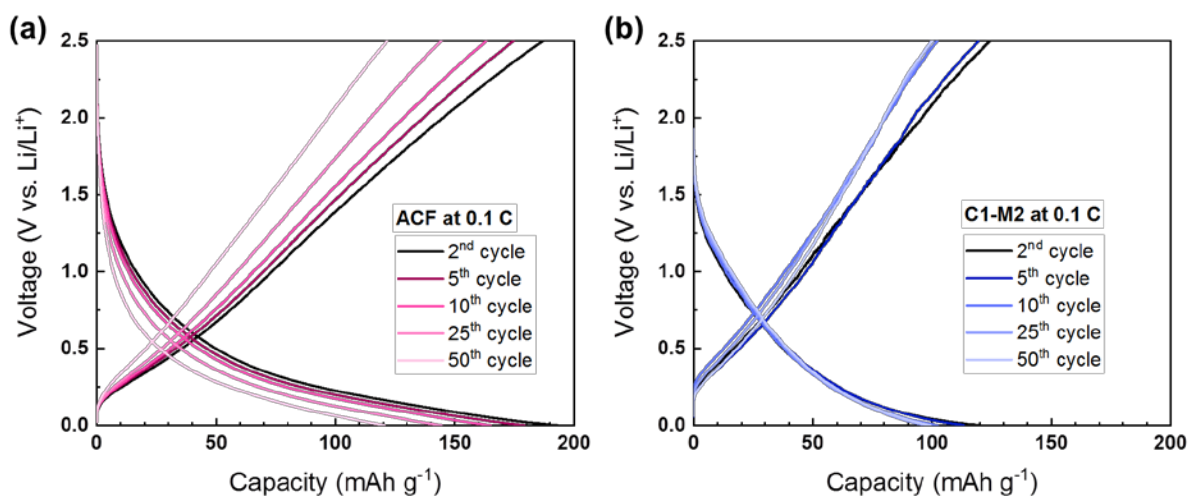
Figure S29. Charge-discharge profiles at 2nd, 5th, 10th, 25th, 50th cycle of (a) ACF and (b) C1-M2 during 50 cycles of continuous cell operation at 0.1 C.

6.5 References

1   F. Sun, M. L. Roderick and G. D. Farquhar, *Proc. Natl. Acad. Sci.*, 2018, **115**, 2305–2310.

2   M. D. Flannigan, B. D. Amiro, K. A. Logan, B. J. Stocks and B. M. Wotton, *Mitig. Adapt. Strateg. Glob. Chang.*, 2006, **11**, 847–859.

3   A. Woodward, K. R. Smith, D. Campbell-Lendrum, D. D. Chadee, Y. Honda, Q. Liu, J. Olwoch, B. Revich, R. Sauerborn, Z. Chafe, U. Confalonieri and A. Haines, *Lancet*, 2014, **383**, 1185–1189.

4   S. R. Loarie, P. B. Duffy, H. Hamilton, G. P. Asner, C. B. Field and D. D. Ackerly, *Nature*, 2009, **462**, 1052–1055.

5   R. K. Kaufmann, H. Kauppi, M. L. Mann and J. H. Stock, *Proc. Natl. Acad. Sci.*, 2011, **108**, 11790–11793.

6   A. Michaelowa, I. Shishlov and D. Brescia, *Wiley Interdiscip. Rev. Clim. Chang.*, 2019, **10**, 1–24.

7   J. Morgan and E. Northrop, *Wiley Interdiscip. Rev. Clim. Chang.*, 2017, **8**, 1–7.

8   N. J. L. Lenssen, G. A. Schmidt, J. E. Hansen, A. Persin, R. Ruedy and D. Zyss, *JGR Atmos.*, 2019, 6307–6327.

9   G. P. Peters, C. Le Quéré, R. M. Andrew, J. G. Canadell, P. Friedlingstein, T. Ilyina, R. B. Jackson, F. Joos, J. I. Korsbakken, G. A. McKinley, S. Sitch and P. Tans, *Nat. Clim. Chang.*, 2017, **7**, 848–850.

10   V. Daioglou, J. C. Doelman, E. Stehfest, C. Müller, B. Wicke, A. Faaij and D. P. Van Vuuren, *Nat. Clim. Chang.*, 2017, **7**, 920–924.

11   C. Mora, D. Spirandelli, E. C. Franklin, J. Lynham, M. B. Kantar, W. Miles, C. Z. Smith, K. Freel, J. Moy, L. V. Louis, E. W. Barba, K. Bettinger, A. G. Frazier, J. F. Colburn IX, N. Hanasaki, E. Hawkins, Y. Hirabayashi, W. Knorr, C. M. Little, K. Emanuel, J. Sheffield, J. A. Patz and C. L. Hunter, *Nat. Clim. Chang.*, 2018, **8**, 1062–1071.

12   Z. M. Chen, S. Ohshita, M. Lenzen, T. Wiedmann, M. Jiborn, B. Chen, L. Lester, D. Guan, J. Meng, S. Xu, G. Chen, X. Zheng, J. J. Xue, A. Alsaedi, T. Hayat and Z. Liu, *Nat. Commun.*, 2018, **9**, 3581.

13   H. Ziar, F. F. Sönmez, O. Isabella and M. Zeman, *Appl. Energy*, 2019, **255**, 113867.

14   D. M. Griffith, J. M. Cotton, R. L. Powell, N. D. Sheldon and C. J. Still, *J. Biogeogr.*, 2017, **44**, 2564–2574.

15   R. A. Betts, C. D. Jones, J. R. Knight, R. F. Keeling and J. J. Kennedy, *Nat. Clim. Chang.*, 2016, **6**, 806–810.

16   R. W. R. Parker, J. L. Blanchard, C. Gardner, B. S. Green, K. Hartmann, P. H. Tyedmers and R. A. Watson, *Nat. Clim. Chang.*, 2018, **8**, 333–337.

17   S. Lorek and J. H. Spangenberg, *J. Clean. Prod.*, 2014, **63**, 33–44.

18   Y. Wang, J. Du, J. M. Kuckelkorn, A. Kirschbaum, X. Gu and D. Li, *Renew. Sustain. Energy Rev.*, 2019, **113**, 109256.

19   J. Nasr, M. Stallmann, C. Rieprich and Umweltbundesamt Hauptsitz, *Germany's 2021 emissions from power stations almost back to pre-pandemic levels*, 2022.

20   F. Dong, Y. Wang, B. Su, Y. Hua and Y. Zhang, *Resour. Conserv. Recycl.*, 2019, **141**, 61–75.

21   European Environment Agency, *CO_2 emissions per capita by country (split by energy and non-energy related emissions)*, 2009.

22   I. A. G. Wilson and I. Staffell, *Nat. Energy*, 2018, **3**, 365–372.

23   T. Jin and J. Kim, *Renew. Sustain. Energy Rev.*, 2018, **91**, 464–471.

24   D. Keles and H. Ü. Yilmaz, *Energy Policy*, 2020, **141**, 111472.

25   Q. Chen, M. Lv, Y. Gu, X. Yang, Z. Tang, Y. Sun and M. Jiang, *Joule*, 2018, **2**, 607–620.

26   K. Matsumoto, M. Doumpos and K. Andriosopoulos, *Renew. Sustain. Energy Rev.*, 2018, **82**, 1737–1748.

27   F. Gökgöz and M. T. Güvercin, *Renew. Sustain. Energy Rev.*, 2018, **96**, 226–239.

28   B. Gillessen, H. Heinrichs, J. F. Hake and H. J. Allelein, *Energy Procedia*, 2019, **158**, 3339–3345.

29   H. U. Heinrichs and P. Markewitz, *Appl. Energy*, 2017, **192**, 234–246.

30   U.N. Department of Economic and Social Affairs, *World Population Prospects: The 2017 Revision*, 2018.

31   E. Taibi, F. Energy, R. Miranda and International Renewable Energy Agency, *Hydrogen from renewable power: Technology outlook for the energy transition*, 2018.

32   U.S. Energy Information Administration (EIA), *Germany announces proposal to phase out coal by 2038, further changing its generation mix*, 2019.

33   J. F. Mercure, H. Pollitt, J. E. Viñuales, N. R. Edwards, P. B. Holden, U. Chewpreecha, P. Salas, I. Sognnaes, A. Lam and F. Knobloch, *Nat. Clim. Chang.*, 2018, **8**, 588–593.

34   R. Arango-Miranda, R. Hausler, R. Romero-Lopez, M. Glaus and S. P. Ibarra-Zavaleta, *Energies*, 2018, **11**, 1–16.

35   U.S. Energy Information Administration (EIA), *International Energy Outlook 2016*, 2016.

36   A. Aslani and K. F. V. Wong, *Renew. Energy*, 2014, **63**, 153–161.

37   D. S. Ryberg, M. Robinius and D. Stolten, *Energies*, 2018, **11**, 1–19.

38   C. Perpiña Castillo, F. Batista e Silva and C. Lavalle, *Energy Policy*, 2016, **88**, 86–99.

39   M. A. Basit, S. Dilshad, R. Badar and S. M. Sami ur Rehman, *Int. J. Energy Res.*, 2020, **44**, 4132–4162.

40   X. Shi, Y. Qian and S. Yang, *ACS Sustain. Chem. Eng.*, 2020, **8**, 7097–7110.

41   B. Dunn, H. Kamath and J. M. Tarascon, *Science*, 2011, **334**, 928–935.

42   S. Speidel and T. Bräunl, *Renew. Sustain. Energy Rev.*, 2016, **60**, 1213–1224.

43   P. Slowik, N. Pavlekno and N. Lutsey, *Assessment of next-generation electric vehicle technologies*, 2016.

44   C. C. Chen and J. Maier, *Nat. Energy*, 2018, **3**, 102–108.

45   A. I. Boothroyd, *Science*, 2006, **314**, 1690–1691.

46   H. Oberhummer, A. Csótó and H. Schlattl, *Science*, 2000, **289**, 88–90.

47   W. Kiciński, M. Szala and M. Bystrzejewski, *Carbon*, 2014, **68**, 1–32.

48   M. Inagaki, M. Toyoda, Y. Soneda and T. Morishita, *Carbon*, 2018, **132**, 104–140.

49   M. M. Titirici, R. J. White, N. Brun, V. L. Budarin, D. S. Su, F. Del Monte, J. H. Clark and M. J. MacLachlan, *Chem. Soc. Rev.*, 2015, **44**, 250–290.

50   J. Lee, J. Kim and T. Hyeon, *Adv. Mater.*, 2006, **18**, 2073–2094.

51   N. George, A. B. Nair, N. Varghese and R. Joseph, *Utilization of carbon allotropes with special reference to carbon nanotubes and graphene for the high performance of natural rubber*, 2nd Ed., 2021.

52   A. Hirsch, *Nat. Mater.*, 2010, **9**, 868–871.

53   D. D. L. Chung, *J. Mater. Sci.*, 2002, **37**, 1475–1489.

54   F. Diederich and C. Thilgen, *Science*, 1996, **271**, 317–323.

55   F. Diederich and M. Gómez-López, *Chem. Soc. Rev.*, 1999, **28**, 263–277.

56   Y. Fang, C. Bi, D. Wang and J. Huang, *ACS Energy Lett.*, 2017, **2**, 782–794.

57   Y. Li, Y. Zhao, Q. Chen, Y. Yang, Y. Liu, Z. Hong, Z. Liu, Y. T. Hsieh, L. Meng, Y. Li and Y. Yang, *J. Am. Chem. Soc.*, 2015, **137**, 15540–15547.

58   D. M. Sun, C. Liu, W. C. Ren and H. M. Cheng, *Small*, 2013, **9**, 1188–1205.

59   Z. Yang, J. Tian, Z. Yin, C. Cui, W. Qian and F. Wei, *Carbon*, 2019, **141**, 467–480.

60   K. S. Novoselov, V. I. Fal'Ko, L. Colombo, P. R. Gellert, M. G. Schwab and K. Kim, *Nature*, 2012, **490**, 192–200.

61   G. AK, *Science*, 2009, **324**, 1530–1534.

62   C. N. R. Rao, A. K. Sood, K. S. Subrahmanyam and A. Govindaraj, *Angew. Chemie Int. Ed.*, 2009, **48**, 7752–7777.

63   Y. Yang, K. Chiang and N. Burke, *Catal. Today*, 2011, **178**, 197–205.

64   S. Iijima, *Nature*, 1991, **354**, 56–58.

65   X. Zhao, M. Ohkohchi, M. Wang, S. Iijima, T. Ichihashi and Y. Ando, *Carbon*, 1997, **35**, 775–781.

66   K. T. Lee, J. C. Lytle, N. S. Ergang, S. M. Oh and A. Stein, *Adv. Funct. Mater.*, 2005, **15**, 547–556.

67   J. Liu, N. P. Wickramaratne, S. Z. Qiao and M. Jaroniec, *Nat. Mater.*, 2015, **14**, 763–774.

68   H. Suda and K. Haraya, *Chem. Commun.*, 1997, **3**, 93–94.

69   T. Morishita, Y. Soneda, T. Tsumura and M. Inagaki, *Carbon*, 2006, **44**, 2360–2367.

70   R. Francisco, *Carbon*, 1998, **36**, 159–175.

71   M. Oschatz, L. Borchardt, M. Thommes, K. A. Cychosz, I. Senkovska, N. Klein, R. Frind, M. Leistner, V. Presser, Y. Gogotsi and S. Kaskel, *Angew. Chemie Int. Ed.*, 2012, **51**, 7577–7580.

72   D. W. Wang, F. Li, M. Liu, G. Q. Lu and H. M. Cheng, *Angew. Chemie Int. Ed.*, 2008, **47**, 373–376.

73   R. E. Morris and P. S. Wheatley, *Angew. Chemie Int. Ed.*, 2008, **47**, 4966–4981.

74   Y. Zhai, Y. Dou, D. Zhao, P. F. Fulvio, R. T. Mayes and S. Dai, *Adv. Mater.*, 2011, **23**, 4828–4850.

75   R. Yan, T. Heil, V. Presser, R. Walczak, M. Antonietti and M. Oschatz, *Adv. Sustain. Syst.*, 2018, **2**, 1–12.

76   F. Yao, D. T. Pham and Y. H. Lee, *ChemSusChem*, 2015, **8**, 2284–2311.

77   A. Ghosh and Y. H. Lee, *ChemSusChem*, 2012, **5**, 480–499.

78   L. Dai, D. W. Chang, J. B. Baek and W. Lu, *Small*, 2012, **8**, 1130–1166.

79   M. Thommes, K. Kaneko, A. V. Neimark, J. P. Olivier, F. Rodriguez-Reinoso, J. Rouquerol and K. S. W. Sing, *Pure Appl. Chem.*, 2015, **87**, 1051–1069.

80   A. Stein, Z. Wang and M. A. Fierke, *Adv. Mater.*, 2009, **21**, 265–293.

81   M. Sevilla and R. Mokaya, *Energy Environ. Sci.*, 2014, **7**, 1250–1280.

82   C. Merlet, C. Péan, B. Rotenberg, P. A. Madden, B. Daffos, P. L. Taberna, P. Simon and M. Salanne, *Nat. Commun.*, 2013, **4**, 2–7.

83   V. Presser, J. McDonough, S. H. Yeon and Y. Gogotsi, *Energy Environ. Sci.*, 2011, **4**, 3059–3066.

84   M. Oschatz, H. C. Hoffmann, J. Pallmann, J. Schaber, L. Borchardt, W. Nickel, I. Senkovska, S. Rico-Francés, J. Silvestre-Albero, S. Kaskel and E. Brunner, *Chem. Mater.*, 2014, **26**, 3280–3288.

85   L. Borchardt, M. Oschatz, S. Paasch, S. Kaskel and E. Brunner, *Phys. Chem. Chem. Phys.*, 2013, **15**, 15177–15184.

86   Z. Hu, M. P. Srinivasan and Y. Ni, *Adv. Mater.*, 2000, **12**, 62–65.

87   A. Ahmadpour and D. D. Do, *Carbon*, 1996, **34**, 471–479.

88   B. Rand and H. Marsh, *Carbon*, 1971, **9**, 79–85.

89   M. Oschatz, L. Borchardt, I. Senkovska, N. Klein, M. Leistner and S. Kaskel, *Carbon*, 2013, **56**, 139–145.

90   D. Salinas-Torres, D. Lozano-Castelló, M. M. Titirici, L. Zhao, L. Yu, E. Morallón and D. Cazorla-Amoros, *J. Mater. Chem. A*, 2015, **3**, 15558–15567.

91   S. Osswald, C. Portet, Y. Gogotsi, G. Laudisio, J. P. Singer, J. E. Fischer, V. V. Sokolov, J. A. Kukushkina and A. E. Kravchik, *J. Solid State Chem.*, 2009, **182**, 1733–1741.

92   F. Rodríguez-Reinoso and M. Molina-Sabio, *Carbon*, 1992, **30**, 1111–1118.

93   J. Wang and S. Kaskel, *J. Mater. Chem.*, 2012, **22**, 23710–23725.

94   L. Borchardt, M. Oschatz and S. Kaskel, *Mater. Horizons*, 2014, **1**, 157–168.

95   Y. Li, C. Li, H. Qi, K. Yu and C. Liang, *Chem. Phys.*, 2018, **506**, 10–16.

96   B. Li, F. Dai, Q. Xiao, L. Yang, J. Shen, C. Zhang and M. Cai, *Adv. Energy Mater.*, 2016, **6**, 1600802.

97   J. H. Knox, B. Kaur and G. R. Millward, *J. Chromatogr. A*, 1986, **352**, 3–25.

98   X. Y. Yang, L. H. Chen, Y. Li, J. C. Rooke, C. Sanchez and B. L. Su, *Chem. Soc. Rev.*, 2017, **46**, 481–558.

99   Y. Xia, Z. Yang and R. Mokaya, *Nanoscale*, 2010, **2**, 639–659.

100   M. E. Davis, *Nature*, 2002, **417**, 813–821.

101   Y. J. Yuan, H. P. Hentze, W. M. Arnold, B. K. Marlow and M. Antonietti, *Nano Lett.*, 2002, **2**, 1359–1361.

102   M. Oschatz and M. Antonietti, *Energy Environ. Sci.*, 2018, **11**, 57–70.

103   S. Polarz and M. Antonietti, *Chem. Commun.*, 2002, **22**, 2593–2604.

104   F. Schüth, *Angew. Chemie Int. Ed.*, 2003, **42**, 3604–3622.

105   X. S. Zhao, F. Su, Q. Yan, W. Guo, X. Y. Bao, L. Lv and Z. Zhou, *J. Mater. Chem.*, 2006, **16**, 637–648.

106   M. R. Benzigar, S. N. Talapaneni, S. Joseph, K. Ramadass, G. Singh, J. Scaranto, U. Ravon, K. Al-Bahily and A. Vinu, *Chem. Soc. Rev.*, 2018, **47**, 2680–2721.

107   C. Zhao, L. Liu, H. Zhao, A. Krall, Z. Wen, J. Chen, P. Hurley, J. Jiang and Y. Li, *Nanoscale*, 2014, **6**, 882–888.

108   N. Díez, M. Sevilla and A. B. Fuertes, *Carbon*, 2021, **178**, 451–476.

109   F. Zhang, Y. Meng, D. Gu, Y. Yan, C. Yu, B. Tu and D. Zhao, *J. Am. Chem. Soc.*, 2005, **127**, 13508–13509.

110   Y. Wan and D. Zhao, *Chem. Rev.*, 2007, **107**, 2821–2860.

111   W. Libbrecht, A. Verberckmoes, J. W. Thybaut, P. Van Der Voort and J. De Clercq, *Carbon*, 2017, **116**, 528–546.

112   Y. Meng, D. Gu, F. Zhang, Y. Shi, H. Yang, Z. Li, C. Yu, B. Tu and D. Zhao, *Angew. Chemie Int. Ed.*, 2005, **44**, 7053–7059.

113   L. Chuenchom, R. Kraehnert and B. M. Smarsly, *Soft Matter*, 2012, **8**, 10801–10812.

114   C. T. Kresge, M. E. Leonowicz, W. J. Roth, J. C. Vartuli and J. S. Beck, *Nature*, 1992, **359**, 710–712.

115   A. Zeleňáková, P. Hrubovčák, O. Kapusta, N. Kučerka, A. Kuklin, O. Ivankov and V. Zeleňák, *Sci. Rep.*, 2019, **9**, 1–9.

116   A. H. Lu and F. Schüth, *Adv. Mater.*, 2006, **18**, 1793–1805.

117   H. Yang and D. Zhao, *J. Mater. Chem.*, 2005, **15**, 1217–1231.

118   S. Jun, Sang Hoon Joo, R. Ryoo, M. Kruk, M. Jaroniec, Z. Liu, T. Ohsuna and O. Terasaki, *J. Am. Chem. Soc.*, 2000, **122**, 10712–10713.

119   R. Ryoo, S. H. Joo and S. Jun, *J. Phys. Chem. B*, 1999, **103**, 7743–7746.

120   M. Choi, W. Heo, F. Kleitz and R. Ryoo, *Chem. Commun.*, 2003, **3**, 1340–1341.

121   D. Saikia, T. H. Wang, C. J. Chou, J. Fang, L. D. Tsai and H. M. Kao, *RSC Adv.*, 2015, **5**, 42922–42930.

122   D. Zhao, Q. Huo, J. Feng, B. F. Chmelka and G. D. Stucky, *J. Am. Chem. Soc.*, 1998, **120**, 6024–6036.

123   P. Strubel, S. Thieme, T. Biemelt, A. Helmer, M. Oschatz, J. Brückner, H. Althues and S. Kaskel, *Adv. Funct. Mater.*, 2015, **25**, 287–297.

124   P. Strubel, H. Althues and S. Kaskel, *Carbon*, 2016, **107**, 705–710.

125   N. Fechler, T. P. Fellinger and M. Antonietti, *Adv. Mater.*, 2013, **25**, 75–79.

126   Q. Wei, X. Tong, G. Zhang, J. Qiao, Q. Gong and S. Sun, *Catalysts*, 2015, **5**, 1574–1602.

127   X. Liu, C. Giordano and M. Antonietti, *Small*, 2014, **10**, 193–200.

128   Y. S. Bae and R. Q. Snurr, *Angew. Chemie Int. Ed.*, 2011, **50**, 11586–11596.

129   X. Lu, D. Jin, S. Wei, Z. Wang, C. An and W. Guo, *J. Mater. Chem. A*, 2015, **3**, 12118–12132.

130   J. B. Howard and D. C. Rees, *Chem. Rev.*, 1996, **96**, 2965–2982.

131   J. M. Lavoie, *Front. Chem.*, 2014, **2**, 1–17.

132   N. Karousis, N. Tagmatarchis and D. Tasis, *Chem. Rev.*, 2010, **110**, 5366–5397.

133   M. Antonietti and M. Oschatz, *Adv. Mater.*, 2018, **30**, 1706836.

134   M. Antonietti, N. Lopez-Salas and A. Primo, *Adv. Mater.*, 2019, **31**, 1–15.

135   M. Perovic, Q. Qin and M. Oschatz, *Adv. Funct. Mater.*, 2020, **30**, 1908371.

136   J. P. Paraknowitsch and A. Thomas, *Energy Environ. Sci.*, 2013, **6**, 2839–2855.

137   Y. P. Wu, E. Rahm and R. Holze, *Electrochim. Acta*, 2002, **47**, 3491–3507.

138   L. Chen, X. Zhang, H. Liang, M. Kong, Q. Guan, P. Chen and C. E. T. Al, *ACS Nano*, 2012, **6**, 7092–7102.

139   X. Xu, Y. Li, Y. Gong, P. Zhang, H. Li and Y. Wang, *J. Am. Chem. Soc.*, 2012, **134**, 16987–16990.

140   K. Gong, F. Du, Z. Xia, M. Durstock and L. Dai, *Science*, 2009, **323**, 760–764.

141   J. Wu, Z. Pan, Y. Zhang, B. Wang and H. Peng, *J. Mater. Chem. A*, 2018, **6**, 12932–12944.

142   Y. Deng, Y. Xie, K. Zou and X. Ji, *J. Mater. Chem. A*, 2015, **4**, 1144–1173.

143   W. Shen and W. Fan, *J. Mater. Chem. A*, 2013, **1**, 999–1013.

144   J. Xu, J. Mahmood, Y. Dou, S. Dou, F. Li, L. Dai and J. B. Baek, *Adv. Mater.*, 2017, **29**, 1–8.

145   W. J. Ong, L. L. Tan, Y. H. Ng, S. T. Yong and S. P. Chai, *Chem. Rev.*, 2016, **116**, 7159–7329.

146   R. J. White, M. Antonietti and M. M. Titirici, *J. Mater. Chem.*, 2009, **19**, 8645–8650.

147   R. Pietrzak, H. Wachowska and P. Nowicki, *Energy and Fuels*, 2006, **20**, 1275–1280.

148   C. M. Yang, C. Weidenthaler, B. Spliethoff, M. Mayanna and F. Schüth, *Chem. Mater.*, 2005, **17**, 355–358.

149   I. Y. Jeon, H. J. Noh and J. B. Baek, *Chem. - An Asian J.*, 2020, **15**, 2282–2293.

150   L. Chen, R. Yan, M. Oschatz, L. Jiang, M. Antonietti and K. Xiao, *Angew. Chemie Int. Ed.*, 2020, **59**, 9067–9073.

151   W. Ju, A. Bagger, G. P. Hao, A. S. Varela, I. Sinev, V. Bon, B. Roldan Cuenya, S. Kaskel, J. Rossmeisl and P. Strasser, *Nat. Commun.*, 2017, **8**, 1–9.

152   Z. Chen, S. Mitchell, E. Vorobyeva, R. K. Leary, R. Hauert, T. Furnival, Q. M. Ramasse, J. M. Thomas, P. A. Midgley, D. Dontsova, M. Antonietti, S. Pogodin, N. López and J. Pérez-Ramírez, *Adv. Funct. Mater.*, 2017, **27**, 1–12.

153   R. Walczak, A. Savateev, J. Heske, N. V. Tarakina, S. Sahoo, J. D. Epping, T. D. Kühne, B. Kurpil, M. Antonietti and M. Oschatz, *Sustain. Energy Fuels*, 2019, **3**, 2819–2827.

154   M. Oschatz and R. Walczak, *Carbon*, 2018, **4**, 56.

155   W. Chen, M. Wan, Q. Liu, X. Xiong, F. Yu and Y. Huang, *Small Methods*, 2019, **3**, 1–18.

156   J. Wu, S. Ma, J. Sun, J. I. Gold, C. Tiwary, B. Kim, L. Zhu, N. Chopra, I. N. Odeh, R. Vajtai, A. Z. Yu, R. Luo, J. Lou, G. Ding, P. J. A. Kenis and P. M. Ajayan, *Nat. Commun.*, 2016, **7**, 1–6.

157   X. H. Li and M. Antonietti, *Chem. Soc. Rev.*, 2013, **42**, 6593–6604.

158   V. Etacheri, R. Marom, R. Elazari, G. Salitra and D. Aurbach, *Energy Environ. Sci.*, 2011, **4**, 3243–3262.

159   A. Manthiram, S. H. Chung and C. Zu, *Adv. Mater.*, 2015, **27**, 1980–2006.

160   D. Geng, N. Ding, T. S. A. Hor, S. W. Chien, Z. Liu, D. Wuu, X. Sun and Y. Zong, *Adv. Energy Mater.*, 2016, **6**, 1–14.

161   C. Delmas, *Adv. Energy Mater.*, 2018, **8**, 1–9.

162   H. Su, A. A. Barragan, L. Geng, D. Long, L. Ling, K. N. Bozhilov, L. Mangolini and J. Guo, *Angew. Chemie*, 2017, **129**, 10920–10925.

163   T. Ohzuku and R. J. Brodd, *J. Power Sources*, 2007, **174**, 449–456.

164   W. Li, B. Song and A. Manthiram, *Chem. Soc. Rev.*, 2017, **46**, 3006–3059.

165   D. Aurbach, I. Weissman, A. Zaban, E. Mengeritsky and P. Dan, *J. Electrochem. Soc.*, 1996, **143**, 2110–2116.

166   G. Salitra, A. Soffer, L. Eliad, Y. Cohen and D. Aurbach, *J. Electrochem. Soc.*, 2000, **147**, 2486.

167   J. B. Goodenough, *Nat. Electron.*, 2018, **1**, 204.

168   M. S. Whittingham, *Chem. Rev.*, 2004, **104**, 4271–4301.

169   H. Pan, Y. S. Hu and L. Chen, *Energy Environ. Sci.*, 2013, **6**, 2338–2360.

170   J. Collins, G. Gourdin, M. Foster and D. Qu, *Carbon*, 2015, **92**, 193–244.

171   F. Kong, R. Kostecki, G. Nadeau, X. Song, K. Zaghib, K. Kinoshita and F. McLarnon, *J. Power Sources*, 2001, **97–98**, 58–66.

172   P. Verma, P. Maire and P. Novák, *Electrochim. Acta*, 2010, **55**, 6332–6341.

173   D. Guyomard and J. M. Tarascon, *J. Electrochem. Soc.*, 1992, **139**, 937–948.

174   J. M. Tarascon, W. R. McKinnon, F. Coowar, T. N. Bowmer, G. Amatucci and D. Guyomard, *J. Electrochem. Soc.*, 1994, **141**, 1421–1431.

175   A. Wang, S. Kadam, H. Li, S. Shi and Y. Qi, *npj Comput. Mater.*, 2018, **4**, 15.

176   J. O'Heir, *Mech. Eng.*, 2017, **139**, 10–11.

177   M. J.-M. Tarascon, Armand, *Nature*, 2001, **414**, 359–367.

178   K. Zaghib, A. Mauger, H. Groult, J. B. Goodenough and C. M. Julien, *Materials*, 2013, **6**, 1028–1049.

179   Y. Wang, C. Yuan, K. Li, D. Li and A. Ju, *ACS Appl. Energy Mater.*, 2022, **5**, 11462–11471.

180   P. Gómez-Romero, J. Fraile and B. Ballesteros, *RSC Adv.*, 2013, **3**, 2351–2354.

181   D. P. Dubal, O. Ayyad, V. Ruiz and P. Gómez-Romero, *Chem. Soc. Rev.*, 2015, **44**, 1777–1790.

182   S. H. Ha and Y. J. Lee, *Chem. - A Eur. J.*, 2015, **21**, 2132–2138.

183   X. Zhou, F. Wang, Y. Zhu and Z. Liu, *J. Mater. Chem.*, 2011, **21**, 3353–3358.

184   Y. Wang, Z. S. Feng, J. J. Chen and C. Zhang, *Mater. Lett.*, 2012, **71**, 54–56.

185   Y. Ding, Y. Jiang, F. Xu, J. Yin, H. Ren, Q. Zhuo, Z. Long and P. Zhang, *Electrochem. commun.*, 2010, **12**, 10–13.

186   R. A. Houstoun, *Elements of Physics*, Longmans, New York, 1919.

187   J. Ho, T. R. Jow and S. Boggs, *IEEE Electr. Insul. Mag.*, 2010, **26**, 20–25.

188   H. I. Becker, *Low voltage electrolytic capacitor*, US2800616A, 1954.

189   F. Béguin, V. Presser, A. Balducci and E. Frackowiak, *Adv. Mater.*, 2014, **26**, 2219–2251.

190   W. Gu and G. Yushin, *Wiley Interdiscip. Rev. Energy Environ.*, 2014, **3**, 424–473.

191   R. Dubey and V. Guruviah, *Ionics*, 2019, **25**, 1419–1445.

192   W. Raza, F. Ali, N. Raza, Y. Luo, K. H. Kim, J. Yang, S. Kumar, A. Mehmood and E. E. Kwon, *Nano Energy*, 2018, **52**, 441–473.

193   W. Schmickler, *Chem. Rev.*, 1996, **96**, 3177–3200.

194   L. Zhang and X. S. Zhao, *Chem. Soc. Rev.*, 2009, **38**, 2520–2531.

195   R. Burt, G. Birkett and X. S. Zhao, *Phys. Chem. Chem. Phys.*, 2014, **16**, 6519–6538.

196   Y. Wang, L. Zhang, H. Hou, W. Xu, G. Duan, S. He, K. Liu and S. Jiang, *J. Mater. Sci.*, 2021, **56**, 173–200.

197   Y. Kado, Y. Soneda, H. Hatori and M. Kodama, *J. Solid State Electrochem.*, 2019, **23**, 1061–1081.

198   M. Salanne, B. Rotenberg, K. Naoi, K. Kaneko, P. L. Taberna, C. P. Grey, B. Dunn and P. Simon, *Nat. Energy*, 2016, **1**, 1–10.

199   C. R, Kotz, M, *Electrochim. Acta*, 2000, **45**, 2483–2498.

200   T. Brousse, D. Bélanger, K. Chiba, M. Egashira, F. Favier, J. Long, J. R. Miller, M. Morita, K. Naoi, P. Simon and W. Sugimoto, *Springer Handbooks*, 2017, 495–561.

201   Y. Korenblit, A. Kajdos, W. C. West, M. C. Smart, E. J. Brandon, A. Kvit, J. Jagiello and G. Yushin, *Adv. Funct. Mater.*, 2012, **22**, 1655–1662.

202   H. Zhang, G. Cao, Y. Yang and Z. Gu, *Carbon*, 2008, **46**, 30–34.

203   Z. Yu, L. Tetard, L. Zhai and J. Thomas, *Energy Environ. Sci.*, 2015, **8**, 702–730.

204   A. Eftekhari, *Energy Storage Mater.*, 2017, **9**, 47–69.

205   M. Antonietti, X. Chen, R. Yan and M. Oschatz, *Energy Environ. Sci.*, 2018, **11**, 3069–3074.

206   F. Wang, X. Wang, Z. Chang, X. Wu, X. Liu, L. Fu, Y. Zhu, Y. Wu and W. Huang, *Adv. Mater.*, 2015, **27**, 6962–6968.

207   S. Zheng, J. Ma, Z. S. Wu, F. Zhou, Y. B. He, F. Kang, H. M. Cheng and X. Bao, *Energy Environ. Sci.*, 2018, **11**, 2001–2009.

208   F. Wang, Z. Liu, X. Yuan, J. Mo, C. Li, L. Fu, Y. Zhu, X. Wu and Y. Wu, *J. Mater. Chem. A*, 2017, **5**, 14922–14929.

209   H. Yong, H. Park and C. Jung, *J. Power Sources*, 2020, **447**, 227390.

210   M. Ishikawa, T. Sugimoto, M. Kikuta, E. Ishiko and M. Kono, *J. Power Sources*, 2006, **162**, 658–662.

211   P. L. T. J. Chmiola, G. Yushin, Y. Gogotsi, C. Portet, P. Simon, *Science*, 2006, **313**, 902.

212   J. Chmiola, C. Largeot, P. L. Taberna, P. Simon and Y. Gogotsi, *Angew. Chemie Int. Ed.*, 2008, **47**, 3392–3395.

213   N. Jäckel, P. Simon, Y. Gogotsi and V. Presser, *ACS Energy Lett.*, 2016, **1**, 1262–1265.

214   E. Raymundo-Piñero, K. Kierzek, J. Machnikowski and F. Béguin, *Carbon*, 2006, **44**, 2498–2507.

215   H. J. Liu, J. Wang, C. X. Wang and Y. Y. Xia, *Adv. Energy Mater.*, 2011, **1**, 1101–1108.

216   M. Rose, Y. Korenblit, E. Kockrick, L. Borchardt, M. Oschatz, S. Kaskel and G. Yushin, *Small*, 2011, **7**, 1108–1117.

217   M. Oschatz, E. Kockrick, M. Rose, L. Borchardt, N. Klein, I. Senkovska, T. Freudenberg, Y. Korenblit, G. Yushin and S. Kaskel, *Carbon*, 2010, **48**, 3987–3992.

218   M. Oschatz, L. Borchardt, K. Pinkert, S. Thieme, M. R. Lohe, C. Hoffmann, M. Benusch, F. M. Wisser, C. Ziegler, L. Giebeler, M. H. Rümmeli, J. Eckert, A. Eychmüller and S. Kaskel, *Adv. Energy Mater.*, 2014, **4**, 1–9.

219   Z. Xu, J. Chen, X. Zhang, Q. Song, J. Wu, L. Ding, C. Zhang, H. Zhu and H. Cui, *Microporous Mesoporous Mater.*, 2019, **276**, 280–291.

220   B. Men, P. Guo, Y. Sun, Y. Tang, Y. Chen, J. Pan and P. Wan, *J. Mater. Sci.*, 2019, **54**, 2446–2457.

221   M. Majumder, R. B. Choudhary and A. K. Thakur, *Carbon*, 2019, **142**, 650–661.

222   Y. Huang, J. Liang and Y. Chen, *Small*, 2012, **8**, 1805–1834.

223   C. Guan, X. Li, Z. Wang, X. Cao, C. Soci, H. Zhang and H. J. Fan, *Adv. Mater.*, 2012, **24**, 4186–4190.

224   H. W. Wang, Z. A. Hu, Y. Q. Chang, Y. L. Chen, H. Y. Wu, Z. Y. Zhang and Y. Y. Yang, *J. Mater. Chem.*, 2011, **21**, 10504–10511.

225   D. Chao, C. Zhu, P. Yang, X. Xia, J. Liu, J. Wang, X. Fan, S. V. Savilov, J. Lin, H. J. Fan and Z. X. Shen, *Nat. Commun.*, 2016, **7**, 1–8.

226   Y. Wang, Y. Song and Y. Xia, *Chem. Soc. Rev.*, 2016, **45**, 5925–5950.

227   S. Li, J. Chen, M. Cui, G. Cai, J. Wang, P. Cui, X. Gong and P. S. Lee, *Small*, 2017, **13**, 1–9.

228   G. G. Amatucci, F. Badway, A. Du Pasquier and T. Zheng, *J. Electrochem. Soc.*, 2001, **148**, A930.

229   A. Jagadale, X. Zhou, R. Xiong, D. P. Dubal, J. Xu and S. Yang, *Energy Storage Mater.*, 2019, **19**, 314–329.

230   V. Aravindan, J. Gnanaraj, Y. S. Lee and S. Madhavi, *Chem. Rev.*, 2014, **114**, 11619–11635.

231   H. S. Choi, T. Kim, J. H. Im and C. R. Park, *Nanotechnology*, 2011, **22**, 405402.

232   J. R. Miller and A. F. Burke, *Electrochem. Soc. Interface*, 2008, **17**, 53–57.

233   H. Wang, C. Zhu, D. Chao, Q. Yan and H. J. Fan, *Adv. Mater.*, 2017, **29**, 1–18.

234   Y. Wang and Y. Xia, *J. Electrochem. Soc.*, 2006, **153**, A450.

235   H. Jiang, J. Ma and C. Li, *Chem. Commun.*, 2012, **48**, 4465–4467.

236   H. Wang, C. Guan, X. Wang and H. J. Fan, *Small*, 2015, **11**, 1470–1477.

237   V. Surendran, A. Lal and M. M. Shaijumon, *ACS Appl. Mater. Interfaces*, 2021, **13**, 52610–52619.

238   Y. Ma, H. Chang, M. Zhang and Y. Chen, *Adv. Mater.*, 2015, **27**, 5296–5308.

239   M. R. Lukatskaya, B. Dunn and Y. Gogotsi, *Nat. Commun.*, 2016, **7**, 1–13.

240   V. Augustyn, P. Simon and B. Dunn, *Energy Environ. Sci.*, 2014, **7**, 1597–1614.

241   H. Kim, M. Y. Cho, M. H. Kim, K. Y. Park, H. Gwon, Y. Lee, K. C. Roh and K. Kang, *Adv. Energy Mater.*, 2013, **3**, 1500–1506.

242   R. Yi, S. Chen, J. Song, M. L. Gordin, A. Manivannan and D. Wang, *Adv. Funct. Mater.*, 2014, **24**, 7433–7439.

243   F. Chen, R. Li, M. Hou, L. Liu, R. Wang and Z. Deng, *Electrochim. Acta*, 2005, **51**, 61–65.

244   V. Aravindan, W. Chuiling, M. V. Reddy, G. V. S. Rao, B. V. R. Chowdari and S. Madhavi, *Phys. Chem. Chem. Phys.*, 2012, **14**, 5808–5814.

245   Q. Wang, Z. Wen and J. Li, *Adv. Funct. Mater.*, 2006, **16**, 2141–2146.

246   I. K. Ilic and M. Oschatz, *Small*, 2021, **17**, 2007508.

247   J. Pampel and T. P. Fellinger, *Adv. Energy Mater.*, 2016, **6**, 1–8.

248   M. Graglia, J. Pampel, T. Hantke, T. P. Fellinger and D. Esposito, *ACS Nano*, 2016, **10**, 4364–4371.

249   I. K. Ilic, A. Tsouka, M. Perovic, J. Hwang, T. Heil, F. F. Loeffler, M. Oschatz, M. Antonietti and C. Liedel, *Adv. Sustain. Syst.*, 2021, **5**, 2000206.

250   X. Ji, K. T. Lee and L. F. Nazar, *Nat. Mater.*, 2009, **8**, 500–506.

251   S. Muench, A. Wild, C. Friebe, B. Häupler, T. Janoschka and U. S. Schubert, *Chem. Rev.*, 2016, **116**, 9438–9484.

252   S. Xu, G. Wang, B. P. Biswal, M. Addicoat, S. Paasch, W. Sheng, X. Zhuang, E. Brunner, T. Heine, R. Berger and X. Feng, *Angew. Chemie*, 2018, **58**, 849–853.

253   R. Yan, K. Leus, J. P. Hofmann, M. Antonietti and M. Oschatz, *Nano Energy*, 2020, **67**, 104240.

254   X. Zhuang, F. Zhang, D. Wu and X. Feng, *Adv. Mater.*, 2014, **26**, 3081–3086.

255   Y. Su, Y. Liu, P. Liu, D. Wu, X. Zhuang, F. Zhang and X. Feng, *Angew. Chemie*, 2015, **127**, 1832–1836.

256   A. Laemont, S. Abednatanzi, P. G. Derakshandeh, F. Verbruggen, E. Fiset, Q. Qin, K. Van Daele, M. Meledina, J. Schmidt, M. Oschatz, P. Van Der Voort, K. Rabaey, M. Antonietti, T. Breugelmans and K. Leus, *Green Chem.*, 2020, **22**, 3095–3103.

257   R. Futamura, T. Iiyama, Y. Takasaki, Y. Gogotsi, M. J. Biggs, M. Salanne, J. Ségalini, P. Simon and K. Kaneko, *Nat. Mater.*, 2017, **16**, 1225–1232.

258   T. Xu, L. Zhou, Y. He, S. An, C. Peng, J. Hu and H. Liu, *Ind. Eng. Chem. Res.*, 2019, **58**, 19642–19648.

259   Q. Meng, Y. Lu, F. Ding, Q. Zhang, L. Chen and Y. S. Hu, *ACS Energy Lett.*, 2019, **4**, 2608–2612.

260   A. Silvestre-Albero, M. Gonalves, T. Itoh, K. Kaneko, M. Endo, M. Thommes, F. Rodríguez-Reinoso and J. Silvestre-Albero, *Carbon*, 2012, **50**, 66–72.

261   J. T. Lee, Y. Zhao, S. Thieme, H. Kim, M. Oschatz, L. Borchardt, A. Magasinski, W. Il Cho, S. Kaskel and G. Yushin, *Adv. Mater.*, 2013, **25**, 4573–4579.

262   P. Giusto, D. Cruz, T. Heil, H. Arazoe, P. Lova, T. Aida, D. Comoretto, M. Patrini and M. Antonietti, *Adv. Mater.*, 2020, **32**, 1908140.

263   M. Sabo, A. Henschel, H. Fröde, E. Klemm and S. Kaskel, *J. Mater. Chem.*, 2007, **17**, 3827–3832.

264   J. Tang, R. R. Salunkhe, J. Liu, N. L. Torad, M. Imura, S. Furukawa and Y. Yamauchi, *J. Am. Chem. Soc.*, 2015, **137**, 1572–1580.

265   R. Yan, E. Josef, H. Huang, K. Leus, M. Niederberger, J. P. Hofmann, R. Walczak, M. Antonietti and M. Oschatz, *Adv. Funct. Mater.*, 2019, **29**, 1902858.

266   R. T. Woodward, F. Markoulidis, F. De Luca, D. B. Anthony, D. Malko, T. O. McDonald, M. S. P. Shaffer and A. Bismarck, *J. Mater. Chem. A*, 2018, **6**, 1840–1849.

267   J. Lin, Z. Peng, Y. Liu, F. Ruiz-Zepeda, R. Ye, E. L. G. Samuel, M. J. Yacaman, B. I. Yakobson and J. M. Tour, *Nat. Commun.*, 2014, **5**, 1–8.

268 S. Zhang, A. Hao, N. Nguyen, A. Oluwalowo, Z. Liu, Y. Dessureault, J. G. Park and R. Liang, *Carbon*, 2019, **144**, 628–638.

269 P. Simon and Y. Gogotsi, *Nat. Mater.*, 2020, **19**, 1151–1163.

270 Z. Wang, F. Li, N. S. Ergang and A. Stein, *Chem. Mater.*, 2006, **18**, 5543–5553.

271 J. O. Besenhard and M. Winter, *ChemPhysChem*, 2002, **3**, 155–159.

272 A. Vu, Y. Qian and A. Stein, *Adv. Energy Mater.*, 2012, **2**, 1056–1085.

273 L. Croguennec and M. R. Palacin, *J. Am. Chem. Soc.*, 2015, **137**, 3140–3156.

274 F. Wang, X. Wu, C. Li, Y. Zhu, L. Fu, Y. Wu and X. Liu, *Energy Environ. Sci.*, 2016, **9**, 3570–3611.

275 L. Zhou, K. Zhang, Z. Hu, Z. Tao, L. Mai, Y. M. Kang, S. L. Chou and J. Chen, *Adv. Energy Mater.*, 2018, **8**, 1–23.

276 N. S. Choi, Z. Chen, S. A. Freunberger, X. Ji, Y. K. Sun, K. Amine, G. Yushin, L. F. Nazar, J. Cho and P. G. Bruce, *Angew. Chemie Int. Ed.*, 2012, **51**, 9994–10024.

277 J. B. Goodenough and Y. Kim, *Chem. Mater.*, 2010, **22**, 587–603.

278 Y. Liu, Y. Zhu and Y. Cui, *Nat. Energy*, 2019, **4**, 540–550.

279 L. Borchardt, M. Oschatz and S. Kaskel, *Chem. - A Eur. J.*, 2016, **22**, 7324–7351.

280 M. Oschatz, P. Pré, S. Dörfler, W. Nickel, P. Beaunier, J. N. Rouzaud, C. Fischer, E. Brunner and S. Kaskel, *Carbon*, 2016, **105**, 314–322.

281 R. Walczak, B. Kurpil, A. Savateev, T. Heil, J. Schmidt, Q. Qin, M. Antonietti and M. Oschatz, *Angew. Chemie Int. Ed.*, 2018, **57**, 10765–10770.

282 Y. Li, Y. Lu, P. Adelhelm, M. M. Titirici and Y. S. Hu, *Chem. Soc. Rev.*, 2019, **48**, 4655–4687.

283 P. K. Nayak, L. Yang, W. Brehm and P. Adelhelm, *Angew. Chemie Int. Ed.*, 2018, **57**, 102–120.

284 J. Mahmood, E. K. Lee, M. Jung, D. Shin, I. Y. Jeon, S. M. Jung, H. J. Choi, J. M. Seo, S. Y. Bae, S. D. Sohn, N. Park, J. H. Oh, H. J. Shin and J. B. Baek, *Nat. Commun.*, 2015, **6**, 4–10.

285 Z. Tian, N. López-Salas, C. Liu, T. Liu and M. Antonietti, *Adv. Sci.*, 2020, **7**, 2001767.

286 N. Fechler, N. P. Zussblatt, R. Rothe, R. Schlögl, M. G. Willinger, B. F. Chmelka and M. Antonietti, *Adv. Mater.*, 2016, **28**, 1287–1294.

287 Z. Xing, Z. Ju, Y. Zhao, J. Wan, Y. Zhu, Y. Qiang and Y. Qian, *Sci. Rep.*, 2016, **6**, 1–10.

288 D. Bhattacharjya, H. Y. Park, M. S. Kim, H. S. Choi, S. N. Inamdar and J. S. Yu, *Langmuir*, 2014, **30**, 318–324.

289 S. Huang, Z. Li, B. Wang, J. Zhang, Z. Peng, R. Qi, J. Wang and Y. Zhao, *Adv. Funct. Mater.*, 2018, **28**, 1–10.

290   A. L. M. Reddy, A. Srivastava, S. R. Gowda, H. Gullapalli, M. Dubey and P. M. Ajayan, *ACS Nano*, 2010, **4**, 6337–6342.

291   U. Subramanya, C. Chua, V. G. He Leong, R. Robinson, G. A. Cruz Cabiltes, P. Singh, B. Yip, A. Bokare, F. Erogbogbo and D. Oh, *RSC Adv.*, 2019, **10**, 674–681.

292   Y. Zheng, Y. Yao, J. Ou, M. Li, D. Luo, H. Dou, Z. Li, K. Amine, A. Yu and Z. Chen, *Chem. Soc. Rev.*, 2020, **49**, 8790–8839.

293   E. Josef, R. Yan, R. Guterman and M. Oschatz, *ACS Appl. Energy Mater.*, 2019, **2**, 5724–5733.

294   S. Ullah, M. Hasan, H. Q. Ta, L. Zhao, Q. Shi, L. Fu, J. Choi, R. Yang, Z. Liu and M. H. Rümmeli, *Adv. Funct. Mater.*, 2019, **29**, 1904457.

295   Y. Wang, H. Xuan, G. Lin, F. Wang, Z. Chen and X. Dong, *J. Power Sources*, 2016, **319**, 262–270.

296   D. Hulicova-Jurcakova, M. Seredych, G. Q. Lu and T. J. Bandosz, *Adv. Funct. Mater.*, 2009, **19**, 438–447.

297   R. Zhang, X. Jing, Y. Chu, L. Wang, W. Kang, D. Wei, H. Li and S. Xiong, *J. Mater. Chem. A*, 2018, **6**, 17730–17739.

298   G. Zhang, L. Lin, G. Li, Y. Zhang, A. Savateev, S. Zafeiratos, X. Wang and M. Antonietti, *Angew. Chemie Int. Ed.*, 2018, **57**, 9372–9376.

299   S. Youk, J. P. Hofmann, B. Badamdorj, A. Völkel, M. Antonietti and M. Oschatz, *J. Mater. Chem. A*, 2020, **8**, 21680–21689.

300   V. Bon, I. Senkovska, J. D. Evans, M. Wöllner, M. Hölzel and S. Kaskel, *J. Mater. Chem. A*, 2019, **7**, 12681–12690.

301   G. P. Hao, G. Mondin, Z. Zheng, T. Biemelt, S. Klosz, R. Schubel, A. Eychmüller and S. Kaskel, *Angew. Chemie Int. Ed.*, 2015, **54**, 1941–1945.

302   S. Maaz, M. Rose and R. Palkovits, *Microporous Mesoporous Mater.*, 2016, **220**, 183–187.

303   D. Saurel, J. Segalini, M. Jauregui, A. Pendashteh, B. Daffos, P. Simon and M. Casas-Cabanas, *Energy Storage Mater.*, 2019, **21**, 162–173.

304   Y. Morikawa, S. ichi Nishimura, R. ichi Hashimoto, M. Ohnuma and A. Yamada, *Adv. Energy Mater.*, 2020, **10**, 1903176.

305   V. Aravindan, Y. S. Lee and S. Madhavi, *Adv. Energy Mater.*, 2017, **7**, 1602607.

306   G. M. Veith, L. Baggetto, L. A. Adamczyk, B. Guo, S. S. Brown, X. G. Sun, A. A. Albert, J. R. Humble, C. E. Barnes, M. J. Bojdys, S. Dai and N. J. Dudney, *Chem. Mater.*, 2013, **25**, 503–508.

307   Y. Matsukawa, F. Linsenmann, M. A. Plass, G. Hasegawa, K. Hayashi, T. P. Fellinger and W. J. Ong, *Beilstein J. Nanotechnol.*, 2020, **11**, 1217–1229.

308   K. Schutjajew, J. Pampel, W. Zhang, M. Antonietti and M. Oschatz, *Small*, 2021, 2006767.

309   C. Ma, C. Deng, X. Liao, Y. He, Z. Ma and H. Xiong, *ACS Appl. Mater. Interfaces*, 2018, **10**, 36969–36975.

310   P. Mcmullan, *Adv. Imaging Electron Phys.*, 2004, **133**, 59–91.

311   R. Bottom, *Princ. Appl. Therm. Anal.*, 2008, **1**, 87–118.

312   M. Thommes and K. A. Cychosz, *Adsorption*, 2014, **20**, 233–250.

313   F. Ambroz, T. J. Macdonald, V. Martis and I. P. Parkin, *Small Methods*, 2018, **2**, 1–17.

314   S. Brunauer, P. H. Emmett and E. Teller, *J. Am. Chem. Soc.*, 1938, **60**, 309–319.

315   A. V. Neimark, Y. Lin, P. I. Ravikovitch and M. Thommes, *Carbon*, 2009, **47**, 1617–1628.

316   K. A. Cychosz, R. Guillet-Nicolas, J. García-Martínez and M. Thommes, *Chem. Soc. Rev.*, 2017, **46**, 389–414.

317   S. Furmaniak, A. P. Terzyk, P. A. Gauden, P. J. F. Harris and P. Kowalczyk, *J. Phys. Condens. Matter*, 2010, **22**, 085003.

318   K. S. W. Sing and R. T. Williams, *Part. Part. Syst. Charact.*, 2004, **21**, 71–79.

319   M. E. Hankus, D. N. Stratis-cullum, P. M. Pellegrino and Army Research Laboratory, *Enabling Technologies for Point and Remote Sensing of Chemical and Biological Agents Using Surface Enhanced Raman Scattering (SERS) Techniques*, 2009.

320   R. Trusovas, G. Račiukaitis, G. Niaura, J. Barkauskas, G. Valušis and R. Pauliukaite, *Adv. Opt. Mater.*, 2016, **4**, 37–65.

321   Q. H. Yang, P. X. Hou, M. Unno, S. Yamauchi, R. Saito and T. Kyotani, *Nano Lett.*, 2005, **5**, 2465–2469.

322   B. Kurpil, A. Savateev, V. Papaefthimiou, S. Zafeiratos, T. Heil, S. Özenler, D. Dontsova and M. Antonietti, *Appl. Catal. B Environ.*, 2017, **217**, 622–628.

6.6 List of publications

6.6.1 Journal publications

[1] **J. Hwang**, S. Youk, K. Schutjajew, W. Zhang and M. Oschatz, "Bridging the Gap between Electrochemistry and Gas Physisorption to Understand the Interplay between Heteroatoms and Nanoporosity in All-Carbon Mixtures for Efficient Lithium Storage"

Manuscript in preparation

[2] **J. Hwang**, W. Zhang, S. Youk, K. Schutjajew and M. Oschatz, "Understanding Structure-Property Relationships under Experimental Conditions for the Optimization of Lithium-Ion Capacitor Anodes based on All-Carbon-Composite Materials", *Energy Technol.* 2021, 9(3), 2001054.

DOI: 10.1002/ente.202001054

[3] W. Zhang, S. Zhan, Q. Qin, T. Heil, X. Liu, **J. Hwang**, T. H. Ferber, J. P. Hofmann, M. Oschatz, "Electrochemical Generation of Catalytically Active Edge Sites in C_2N-type Carbon Materials for Artificial Nitrogen Fixation" *Small* 2022, 18(42), 2204116.

DOI: 10.1002/smll.202204116

6.6.2 Conference contribution

WILEY Weinheim Symposium on Energy Technology 2021, Germany

"Understanding Structure-Property Relationships under Experimental Conditions for the Optimization of Lithium-Ion Capacitor Anodes based on All-Carbon-Composite Materials"

Jinyeon Hwang (Oral presentation: Speaker) and Martin Oschatz

6.7 Declaration

Die vorliegende Dissertation entstand in dem Zeitraum zwischen März 2018 und März 2021 am Max-Planck-Institut für Kolloid- und Grenzflächenforschung und an der Universität Potsdam unter der Betreuung von Prof. Dr. Martin Oscahtz.

Hiermit erkläre ich, dass die vorliegende Arbeit selbstständig angefertigt wurde und keine anderen als die angegebenen Hilfsmittel und Quelle verwendet wurden.

Die Arbeit wurde bisher weder im Inland noch im Ausland in gleicher oder ähnlicher Form einer anderen Prüfungsbehörde vorgelegt.

Es habe bisher keine früheren erfolglosen Promotionsverfahren stattgefunden.

The present work was carried out during the period of March, 2018 to March, 2021 at the Max Planck Institute of Colloids and Interfaces and at University of Potsdam under supervision of Prof. Dr. Martin Oschatz.

I declare that I have written this work on my own and used no other than the named aids and references.

This thesis was not submitted to another examination board in this or other countries.

There were no unsuccessful examination processes.

Jinyeon Hwang

Potsdam, 21.01.2023